Towards development of automatic path planning system in image-guided neurosurgery

---

by

Rui Hui

October 2014

School of Science and Technology
Middlesex University London

A dissertation submitted to Middlesex University London in partial fulfilment of the requirements for the degree of Doctor of Philosophy

Abstract

With the advent of advanced computer technology, many computer-aided systems have evolved to assist in medical related work including treatment, diagnosis, and even surgery. In modern neurosurgery, Magnetic Resonance Image guided stereotactic surgery exactly complies with this trend. It is a minimally invasive operation being much safer than the traditional open-skull surgery, and offers higher precision and more effective operating procedures compared to conventional craniotomy. However, such operations still face significant challenges of planning the optimal neurosurgical path in order to reach the ideal position without damage to important internal structures. This research aims to address this major challenge.

The work begins with an investigation of the problem of distortion induced by MR images. It then goes on to build a template of the Circle of Wills brain vessels, realized from a collection of Magnetic Resonance Angiography images, which is needed to maintain operating standards when, as in many cases, Magnetic Resonance Angiography images are not available for patients. Demographic data of brain tumours are also studied to obtain further understanding of diseased human brains through the development of an effect classifier.

The developed system allows the internal brain structure to be ‘seen’ clearly before the surgery, giving surgeons a clear picture and thereby makes a significant contribution to the eventual development of a fully automatic path planning system.

Acknowledgements

I would like to thank the director of my research, Prof. Xiaohong Wang Gao, for her guidance in this project and constructive criticism on the thesis. I am also grateful for her encouragement throughout the project.

I would also like to express my deepest appreciation to Prof. Richard Comley and Prof. Zengmin Tian, for their unconditional support and expertise on the project.

I would like to pay my special tribute to Prof. Anthony White, whose guidance and encouragement helped me in many ways during the project before he left university after taking retirement.

Many thanks go to the staff and research students of Middlesex University London for the discussions, support and help with the program. Special thanks go to Dr. Yu Qian, Mr. Eser Gemikonakli and Mr. Payam S. Rahmdel, who helped me with the program.

I offer my gratitude and sincere thanks to my parents for their encouragement, love and support. All my love goes to my wife, Dr. Dan Li, for her enduring encouragement and discussion during my writing.

This work is financially supported by the School of Science and Technology, Middlesex University London, whose support is gratefully acknowledged.

Abbreviations

2 D: Two Dimensional

3 D: Three Dimensional

ACA: Anterior Cerebral Artery

BA: Basilar Artery

BW: Binary images

COW: Circle of Wills

CSF: Cerebrospinal Fluid

CT : Computer Tomography

DI: Different Index

Exp: Exponential

fMRI: functional Magnetic Resonance Angiography

GTR: Grossly Total Removal

ICA: Internal Carotid Artery

MCA: Middle Cerebral Artery

MIP: Maximum Intensity Projection

mm: millimetre

MRA: Magnetic Resonance Angiography

MRI: Magnetic Resonance Image

^{32}P: ^{32}Phosphate

PCA: Posterior Cerebral Artery

PCoA: Posterior Communicating Artery

PET: Positron Emission Tomography

RT: Radiation Therapy

SCA: Superior Cerebellar Artery

SI: Similarity Index

SPM: Statistical Parametric Mapping

SVD: Singular Value Decomposition

T: Tesla

T1W: T1 Weighted

T2W: T2 Weighted

T-COW: Template of COW

VA: Vertebral Artery

VI: Volume Index

Contents

1. INTRODUCTION 1

2. LITERATURE REVIEW 4

2.1 THE DEVELOPMENT STATUS OF BRAIN STEREOTACTIC OPERATION AND FRAMELESS STEREOTACTIC NEUROSURGICAL ROBOT 5

2.1.1 The development of brain stereotactic operative technique 5

2.1.1.1 The stage of brain function orientation in animal studies 5

2.1.1.2 The stage of x-ray ventriculography orientation in clinical applications of extrapyramidal system disease 6

2.1.1.3 The stage of the nervous system anatomic imaging guided three-dimensional orientation in treatments of diverse brain diseases 7

2.2 THE PROGRESS OF CRANIOPHARYNGIOMAS TREATMENT 8

2.2.1 Brief introduction to craniopharyngiomas 8

2.2.2 The clinical manifestations of craniopharyngiomas 9

2.2.3 The imaging features of craniopharyngiomas 10

2.2.4 The treatment options of craniopharyngiomas 13

2.2.4.1 The surgical excision with or without adjuvant conventional external beam irradiation 13

2.2.4.2 The intracystic irradiation 15

2.2.4.3 Stereotactic radiosurgery 16

2.2.5 Therapeutic strategy 17

2.3 THE PROGRESS IN THE CORRECTION OF MR IMAGES DISTORTION 19

2.3.1 Progress in the correction of MR images distortion before or during the process of MR scan 19

2.3.2 Progress in the correction of MR images distortion after the process of MR scan 22

2.3.3 Progress in the correction of MR images distortion using spatial references 25

2.4 OVERVIEW OF CEREBRAL VASCULAR SYSTEM 25

2.4.1 Carotid system 26

2.4.1.1 Circle of Willis 27

2.4.1.2 Anterior Cerebral Artery 30

2.4.1.3 Middle Cerebral Artery 32

2.4.2 Vertebral system 32

2.4.3 Posterior cerebral artery 34

2.4.4 Summary of the arterial blood supply to the brain 35

2.5 PROGRESS IN BUILDING A VASCULAR TEMPLATE 37

2.5.1 Progress on the calculation of mean dataset 38

2.5.2 Progress on the vascular skeletonisation 39

2.6 PROGRESS IN SURGICAL PATH PLANNING IMAGE GUIDED NEUROSURGERY 39

2.6.1 Progress in medical images visualizing and surgical path planning 41

2.6.2 Progress in automatic surgical path planning 42

3 METHODOLOGY 45

3.1 METHODS OUTLINE 45

3.2 CLINICAL DATA ACQUISITION 46

3.2.1 MR data collection 46

3.2.2 Surgical path collection 47

3.3 Detection of MR images distortion 50
3.4 Tumours location analysis 50
3.5 Targets and angles of existing surgical path lines analysis 51
3.6 Coordinate data alignment 51
3.7 Building a cerebrovascular template 54
3.7.1 Data collection 54
3.7.2 Spatial normalisation 54
3.7.3 Extraction of Circle of Willis (COW) artery 55
3.7.4 Calculation of mean COW using spherical Fisher-Rao metric 61
3.7.5 Skeletonization of the mean COW 66
3.7.6 Re-construction of mean COW 67
3.7.7 Designing a surgical path by finding the minimal distance 68

4 DETECTION OF MR IMAGES DISTORTION 70

4.1 Methods 70
4.1.1 Linear transformation with non-isotropic scale factors 70
4.1.2 Linear transformation with a constant scale factor 72
4.2 Results 72
4.3 Summary 75

5 IMAGES DATA ANALYSIS AND CLASSIFICATION 76

5.1 Tumours location analysis 76
5.2 Targets and angles of existing surgical path lines analysis 77
5.3 Coordinate data alignment 77
5.4 Data Classification 79
5.5 Summary 81

6 RESULTS OF BUILDING CEREBRAL VASCULAR TEMPLATE 82

6.1 Experimental results 82
6.2 The analysis of variation of the mean COW 89
6.3 A clinical application 91
6.4 Summary 93

7. CONCLUSION AND FUTURE WORKS 96

7.1 Conclusion 96
7.2 Future works 96
7.2.1 Initial programming 98
7.2.2 Programming based on cost functions 99
7.2.3 Establishment of an expert system 100
7.2.4 Convert and implant the programme 100
7.2.5 Evaluation 100

REFERENCE 102

APPENDIX 110

Captions

List of Figures

Figure1.1 A flowchart of automatic surgical path planning system process for stereotactic operations 3
Figure 2.2.1Axial unenhanced (A) and contrast-enhanced (B) brain demonstrate a craniopharyngioma locating suprasellar region with different contents 11
Figure 2.2.2 Axial brain CT demonstrates a craniopharyngioma locating suprasellar region with cyst capsule and coarse calcification, and dilatation of the temporal horns of the lateral ventricles..... 12
Figure 2.2.3 Therapeutic strategy of craniopharyngioma 18
Figure 2.3 Schematic diagram of decomposing distortion factor into rotation, translation and scaling factor 23
Figure. 2.4.1 Carotid and vertebral arteries deriving the aortic arch and secondary vessels 26
Figure. 2.4.2 Ventral view (sketch and MRA) of vertebral–basilar system and its relationship to the brainstem and carotid circulation 29
Figure.2.4.3 Midsagittal view of the cerebral hemisphere shows the general distribution of the main branches of the anterior and posterior cerebral arteries 31
Figure 2.4.4 Lateral view illustrates the distribution of the middle cerebral artery 31
Figure 2.4.5 Lateral view of the vertebral–basilar system shows its relationship to the internal carotid artery 33
Figure 2.5 Interface of frame stereotactic operation for Craniopharyngioma 40
Figure 3.1 A flowchart of clinical data processing in this study..... 45
Figure 3.2 The flow chart of the establishment of a mean architecture of COW 46
Figure 3.3 A photo of Signa horizon 1.5T, GE Medical System 47
Figure 3.4 Left: Appearance of CAS-R-2 robot system; Right: Performing a frameless stereotactic operation with the CAS-R-2 robot system 49
Figure 3.5 Snapshot picture of the operative interface for frameless stereotactic operation..... 49
Figure 3.6 The sketch of the new 3D coordinate system 53
Figure 3.7 The Circle of Willis artery 56
Figure 3.8 An example displaying the Gaussian distribution of the intensity profile of arteries 58
Figure 3.9 The procedure of calculating the mean of images 1 and 2..... 66
Figure 3.10 Schematic illustration of reconstruction of a vessel cross-section with diameter of d 68
Figure 4.1 A head frame with contrast agent filled in the N shape tubes 73
Figure 4.2 CT and MR slices at the same head position (same z direction) 74
Figure 5.1 The interface of 3D Slicer (Module Models)..... 76
Figure 5.2 Two examples of surgical paths that are indicated by red lines in the frameless stereotactic operative interface 80
Figure 5.3 The locations of tumour centres of 100 in the XY plane 80
Figure 5.4 The angles of the 100 path lines projected onto XY and YZ planes..... 81
Figure 6.1 The measurement of arteries in COW for the twenty-two datasets (x-axis) investigated in this study 83
Figure 6.2. The extraction of COW from 22 datasets using a Hessian matrix 85
Figure 6.3 3D view of mean COWs 86
Figure 6.4 Reconstruction of the Circle of Willis (COW)..... 87
Figure 6.5 The reconstructed COW template with two ACAs 88

Figure 6.6 The plots of VI, SI and DI between control data (left) and test data (right) and the mean 90
Figure 6.7 Visual comparison between six test datasets and the COW template with two shown in each graph 91
Figure 6.8 An example of surgical planning for tumour removal 92
Figure 7.1 A flowchart of automatic surgical path planning process in this study 97
Figure 7.2 Three snapshot pictures captured at three time points during the process of minimal distance calculation on Matlab platform 98

List of Tables

Table 3.1. Constants applied in the process of COW enhancement 61
Table 4.1 The largest transformative errors worked out from two algorithms 74
Table 6.1 Image sizes during each processing stage 82
Table 6.2 The mean diameters measured from the twenty-two datasets. 84
Table 7.1 Importance values of different introcranial structures 99

1. Introduction

In the late 20th century, computer technology had been applied to the field of neurosurgery by some forward-looking scientists. The development of surgical robotic technology, computerised navigational systems and the establishment of community networks have made it possible to perform computer-assisted neurosurgery by the end of the 20th century[1,2]. The accurate, expeditious and reliable stereotactic operation, which is a branch of computer-assisted neurosurgery, has saved many lives all over the world so far and has become more and more popular both with doctors and patients[3].

Nowadays, image-guided stereotactic neurosurgical operation is widely employed by functional neurosurgery, pathological biopsy as well as cysti-liquid aspiration [4,5,6]. With a remarkable curative effect, stereotactic operation has been used mainly to treat craniopharyngioma. Craniopharyngiomas are congenital epithelial tumours arising along the path of the craniopharyngeal duct[7]. They may be diagnosed during childhood or adult life and are often associated with an enigmatic and unpredictable growth pattern. Despite their benign histological appearance, their often infiltrative tendency into critical parasellar structures and their aggressive behaviour, even after apparently successful therapy, may result in significant morbidity and mortality posing a considerable medical and social problem [8]. However, doctors rest their hope to cure this disease on stereotactic neurosurgical operation because it is effective, reliable and multi-operable [9,10].

As one of the most important elements in computer-assisted stereotactic neurosurgery, image guidance has been widely integrated into the practice of cranial surgery and some specific spinal surgeries [11]. Above all, image data which is used in stereotactic operations must be clear, accurate and distortionless irrespective of which domains, such as, Magnetic Resonance Image (MRI), Computer Tomography (CT) or fused images. Images can be utilised to guide a surgeon in two ways in the practical stereotactic operation [12], which can be demonstrated in two steps as follows:

1. Registration of a patient's medical images (CT or MR images etc.) onto the physical space of the same patient's anatomy. Various images data, brain atlases or vessels' distribution for instance, can be added in during the process, so that all of the information may be used simultaneously [13]. To realise the registration of the images data onto the physical space of the patient's anatomy, a physical device is used to link them with each other. These physical devices, relative to the patient's head, must be immovable and can be displayed on both CT and MR images, such as a head frame with a contrast agent inside or adhesive fiducial markers fixed to the patient's skin.

2. Provision of image information to the surgeon in an intuitionistic, interactive and useful way. Having accomplished registration, an image-guide system can display image data in different planes and reconstruct them into pseudo three-dimensional data in a manner more relevant to the surgeon. The image data display allows surgeons the ability to perform many tasks that include reformatting of images, multiple user-selected two or three-dimensional display formats, virtual reality and augmented reality interface and treatment planning. This can be converted to enable the robot to perform a neurosurgical operation [14].

The accurate stereotactic operation relies on clear and distortionless medical images, while the safety and effective operation depends on professional knowledge and clinical experience. Surgical path planning is at the very core of computer-assisted neurosurgery. Normally, a neurosurgeon designs an effective and safe path to the lesion depending on his/her clinical experience. However, for a junior doctor who is not so competent in planning a perfect path, there is no reliable module that can provide valuable planning automatically. Although a few existent systems have the training interface in path planning for junior doctors, it is still a long way from a practical implementation.

This study investigates how the process of image guided stereotactic operation may be automated. From the beginning, MR images were analysed by a distortion correction module to ensure the precision of the medical images. Then, MR images were detected by a classification module to pick up an image series with tumours. After that, a standard vessel template was implanted in the image series to build a 3D brain model with

tumours and vessels. Finally, based on the 3D brain model, a neurosurgical path planning module can generate a practical surgical path that is able to guide a neurosurgical stereotactic operation. The flow chart of this process is shown below (Figure. 1.1). The aim of this work is to develop this system, which can promote medical doctors performing stereotactic operations as easily as possible, and can provide training for basic neurosurgical education. To achieve this goal, different kinds of medical images such as MRI, CT, Magnetic Resonance Angiography (MRA) and stereotactic operation path planning interface snapshots are analyzed by diverse means in this study, and new approaches and modules are developed, which in turn ensure the reliability and security of automatic surgical path planning system.

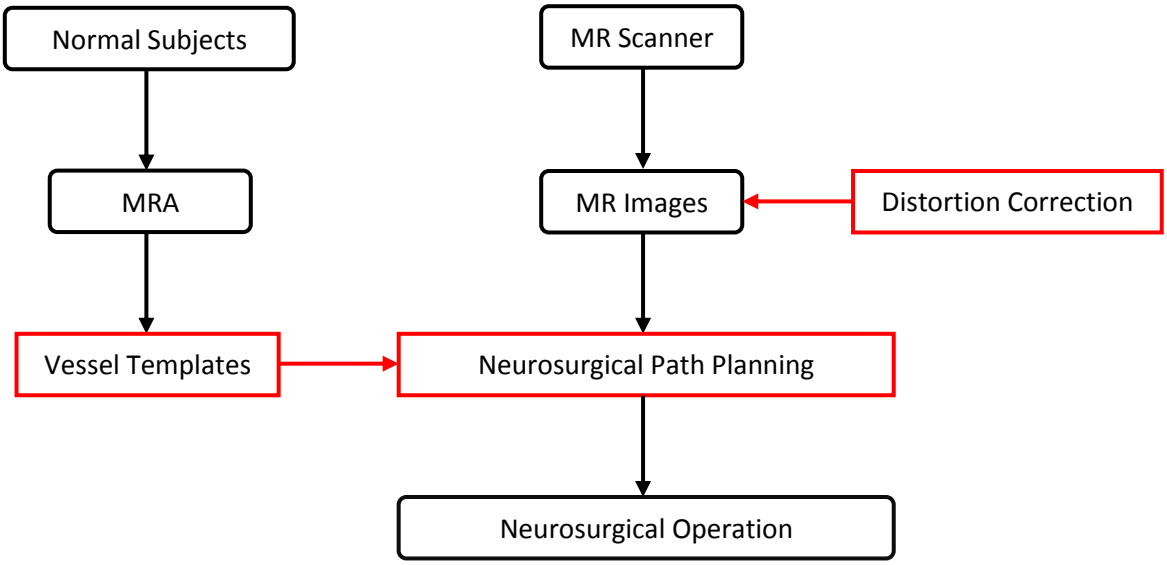

Figure1.1 A flowchart of automatic surgical path planning system process for stereotactic operations

2. Literature Review

The brain is the most complex organ in the human body. Through the centuries, many serious health hazards associated with various brain diseases have been identified. Neurosurgery is the medical specialty concerned with the prevention, diagnosis, treatment, and rehabilitation of disorders which affect the nervous system, especially the brain, in a surgical manner. However, in the past, intracranial operations were dangerous to the patient and only used to treat a small proportion of brain diseases.

With rapid development of medical imaging techniques, CT and MR have been employed as the primary means to diagnose brain disease and to guide intracranial operations. A traditional intracranial operation is performed as follow: find the bodily superficial projection of the lesion, design the scalp insection, remove a part of the bone from the skull to expose the brain and then, remove the lesion. The bone flap is temporarily removed, then replaced and stitched with the rest of the tissue after the lesion has been taken out. Therefore, a traditional intracranial operation is called a craniotomy. Thus, craniotomy brings more surgical injuries, and the outcome of the operation is more determined by the neurosurgeon's surgical skills and experience.

Alternatively, some other 'craniotomy' procedures may utilize the guidance of computers and imaging to reach the precise location within the brain that is to be treated. This intracranial operation cuts a small in section and drills a small hole in the skull instead of making a bone flap, which is known as a key-hole technique. This technique requires the use of a frame placed onto the skull or a frameless system using superficially placed marks on the scalp. Scans made of the brain, in conjunction with these computers and localizing frames, provide a three-dimensional image, for example, of a tumour within the brain. It is useful in making the distinction between tumour tissue and healthy tissue and reaching the precise location of the abnormal tissue. When either of these imaging procedures is used along with the 'craniotomy' procedure, it is called a stereotactic operation.

2.1 The development status of brain stereotactic operation and frameless stereotactic neurosurgical robot

2.1.1 The development of brain stereotactic operative technique

It has a history of more than 100 years, since the stereotactic operative technique was invented. There are three stages in the development: 1) the stage of the brain function orientation in animal studies, 2) the stage of the X-ray ventriculography orientation in clinical applications of extrapyramidal system disease, 3) the stage of the nervous system anatomic imaging guided three-dimensional orientation in treatments of diverse brain diseases. The details are as follow:

2.1.1.1 The stage of brain function orientation in animal studies

As early as 1889, Prof. Zernov, an anatomist at the Muscovite University, developed the first stereotactic apparatus in the world. The apparatus, called an encephalometer, was designed using the principle of spherical polar coordinates to calculate the coordinate data of the target, and made use of experimental study of brain function orientation. Several years later, Rossolimo improved the encephalometer to the brain topograph, and made more attempts at experimental studies. These were the rudiments of modern stereotactic apparatus.

In 1908, two British scientists, Sir Victor Horsley, a physician and neurosurgeon, and Robert H. Clarke, a physiologist, working at University College London Hospital, invented the Horsley–Clarke apparatus based on the Cartesian (three-orthogonal axis) system [15]. It was huge and complex (with 151 components), and was used initially for animal experimentation. It made a great contribution to further basic and clinical research on the central nervous system. Improved designs of their original device came into use in the 1930s for animal experimentation and are still in wide use today in all animal neuroscience laboratories. However, using the Horsley–Clarke apparatus for human

brains was difficult because of the inability to visualize intracranial anatomic detail via radiography.

2.1.1.2 The stage of x-ray ventriculography orientation in clinical applications of extrapyramidal system disease

With the use of X-rays, some of intracranial structures became visible. Brain radiography (particularly ventriculography) permitted the visualization of intracranial anatomic reference points or landmarks. The first stereotactic devices for humans used the pineal gland and the foramen of Monro as landmarks. Later, other anatomic reference points such as the anterior and posterior commissures were used as intracranial landmarks. These landmarks were used with a brain atlas to estimate the location of intracranial anatomic structures that were not visible in radiographs.

Two American neurosurgeons, Ernest A. Spiegel and Henry T. Wycis, in 1947, developed the first stereotactic apparatus that were used for brain surgery in humans [16]. Spiegel and Wycis used the Cartesian coordinate system (also called the translational system) for their device. In addition, they compiled the first atlas of brain stereotactic operation in the world, and first applied the stereotactic technique to treat central nervous system disease.

Leksell's apparatus used the polar coordinate system (also called spherical) that was far easier to use and calibrate in the operating room. The stereotactic localization system was also used by Leksell in his next invention, a device for radiosurgery of the brain. This system is also used by the Gamma Knife device, and by other neurosurgeons, using other radiation therapy [17]. Leksell significantly affected the development of the stereotactic technique and to date, derivatives of Leksell’s apparatus still have a wide application in modern neurosurgery.

2.1.1.3 The stage of the nervous system anatomic imaging guided three-dimensional orientation in treatments of diverse brain diseases

The invention of computerised tomography in the 1970s, and magnetic resonance imaging of the brain in the 1980s, has resulted in a seismic shift in the development of nerve system localization diagnosis. In 1978, Russell A. Brown, an American physician and computer scientist, developed a device known as the N-localizer that guides stereotactic surgery using tomographic images that are obtained via medical imaging technologies from CT [18,19]. The N-localizer significantly improves surgical precision because MRI and CT permit accurate visualization of intracranial anatomic detail. The N-localizer creates extra-cranial fiducial marks or landmarks in each tomographic image. These fiducial marks specify the spatial orientation of that image with respect to the stereotactic instrument. Usually, the N-localizer is fixed with a detachable head frame to perform the stereotactic operation, namely the frame stereotactic operation which is widely used today.

The development of surgical robotic technology, computerized navigational systems and the establishment of community networks with high-speed data transfer have made robot-assisted frameless stereotactic operation possible. Comparing with the frame stereotactic technique, the frameless technique is more comfortable for the patient because it no longer requires a frame to be attached to the patient's head. In addition, sticky fiducial marks on the patient's scalp can be used to register the anatomic structure to corresponding medical images. Moreover, fiducial-based registration is more accurate than the use of anatomical landmarks [20].

Although the brain stereotactic operation technique has developed late in mainland China, some of the hospitals have been making great progress in this field. A series of technical innovations have resulted in greater accuracy of surgical localization, minimal invasion and optimized surgery outcomes. Surgical robotics also plays significant roles in facilitating the development of surgical instruments and sharing medical expertise between large and small, urban and rural hospitals [21]. In neurosurgery, telementoring

systems have made it possible for an expert surgeon in a major health care centre to provide real-time guidance for another surgeon in a remote location [22]. Based on such progress, the Navy General Hospital of the Chinese People's Liberation Army and the Yan'an University Affiliated Hospital jointly performed successfully telemanipulation frameless stereotactic operations using the CAS-BH5 robot system. This preliminary data indicates that telemanipulation in frameless stereotactic surgeries is feasible, reliable and safe [23].

The stereotactic technique has continued to evolve, and at present employs an elaborate mixture of image-guided surgery that uses computed tomography, magnetic resonance imaging and stereotactic localization, will facilitate collaboration between surgeons, enhance training, allow for sharing of resources, and have wide applications in the field of neurosurgery in the future.

2.2 The progress of craniopharyngiomas treatment

2.2.1 Brief introduction to craniopharyngiomas

Craniopharyngiomas are epithelial tumours arising along the path of the craniopharyngeal duct. Craniopharyngiomas may arise anywhere along the craniopharyngeal canal, but most of them are located in the sellar/parasellar region.

In 1857, Zenker was the first to indentify masses of cells resembling squamous epithelium along the pars distalis and pars tuberalis of the pituitary [24]. Since then, many doctors reported and described successively the occupying lesions at the sellar region which were different from the common brain tumour such as the glioma and meningioma [25, 26]. Because the histology was not developed enough to detect all histopathologic changes of the tissue, craniopharyngiomas were not described completely until 1932. Susman, in 1932, detected the squamous epithelial cells in the pituitary glands of childhood populations, indicating the formation of the complete concept [27]. In the same year, Cushing introduced the name 'craniopharyngioma' as a new neurological

terminology [28]. However, the first attempt for surgical removal of the tumour by Dr. A. E. Halstead in St. Luke's Hospital, while it was not diagnosed as craniopharyngioma, was reported in 1910 by Lewis [29].

2.2.2 The clinical manifestations of craniopharyngiomas

The intracranial occupying lesions cause various clinical manifestations depending on the location, the size, and the growth potential of the lesions. Likewise, the potential proximity to and the subsequent pressure effects of craniopharyngiomas on vital structures of the brain (visual pathways, brain parenchyma, ventricular system, major blood vessels, and hypothalamo-pituitary system) predispose the patients to multiple clinical manifestations [30, 31]. The duration of the symptoms until diagnosis ranges between 1 week and 372 months [32]. Headaches, nausea/vomiting, visual disturbances, growth failure (inchildren), and hypogonadism (in adults) are the most frequently reported. Other less common or rare features include motor disorders, such as hemi- or monoparesis, seizures, psychiatric symptoms, such as emotional lability, hallucinations, paranoic delusions, autonomic disturbances, precocious puberty, the syndrome of inappropriate secretion of antidiuretic hormone, chemical meningitis due to spontaneous cyst rupture, hearing loss, anosmia, photophobia, emaciation, Weber's syndrome (ipsilateral III cranial nerve palsy with contra-lateral hemiplegia due to midbrain infarction), and Wallenberg's syndrome (signs due to occlusion of the posterior inferior cerebellar artery) [30, 33, 34, 35]. On the other hand, the hypothalamo-pituitary function at presentation may be severely compromised; interestingly, in a series of 122 patients, 85% had one to three hormone deficits [36].

It has been implied that the presenting clinical manifestations may be distinct in the various age groups, with most commonly reported symptoms of raised intracranial pressure in young children, sexual immaturity in adolescents, visual field defects and features of hypopituitarism in young and middle-aged adults [37], and mental changes in elderly subjects [38]. In a large series of patients, comparing the presenting manifestations between childhood and adult populations, apart from headaches,

nausea/vomiting, papilloedema, and cranial nerve palsies, which were more frequent in children (probably associated with the high rates of hydrocephalus in this age group), no further differences in the clinical picture, the symptoms duration, and the rates of ndocrine deficits were found [32].

2.2.3 The imaging features of craniopharyngiomas

In modern neurosurgery, computed tomography (CT), magnetic resonance imaging (MRI), and occasionally, cerebral angiography are useful tools for the neuroradiological characterization of the craniopharyngiomas. Although plain skull x-ray films have been superseded by newer imaging techniques, they may still be used to show an abnormal sella and tumour calcification [39].

CT produces a volume of data that can be manipulated in order to demonstrate various bodily structures based on their ability to block an x-ray beam. Pre- and post-contrast enhanced images in the axial plane followed by post-contrast coronal images have been advocated [40]. The CT appearance of craniopharyngiomas depends on the proportion of the solid and the cystic components; they are usually of mixed attenuation, the cyst fluid has low density, and the contrast medium enhances any solid portion, as well as the cyst capsule [40] (Figure 2.2.1).

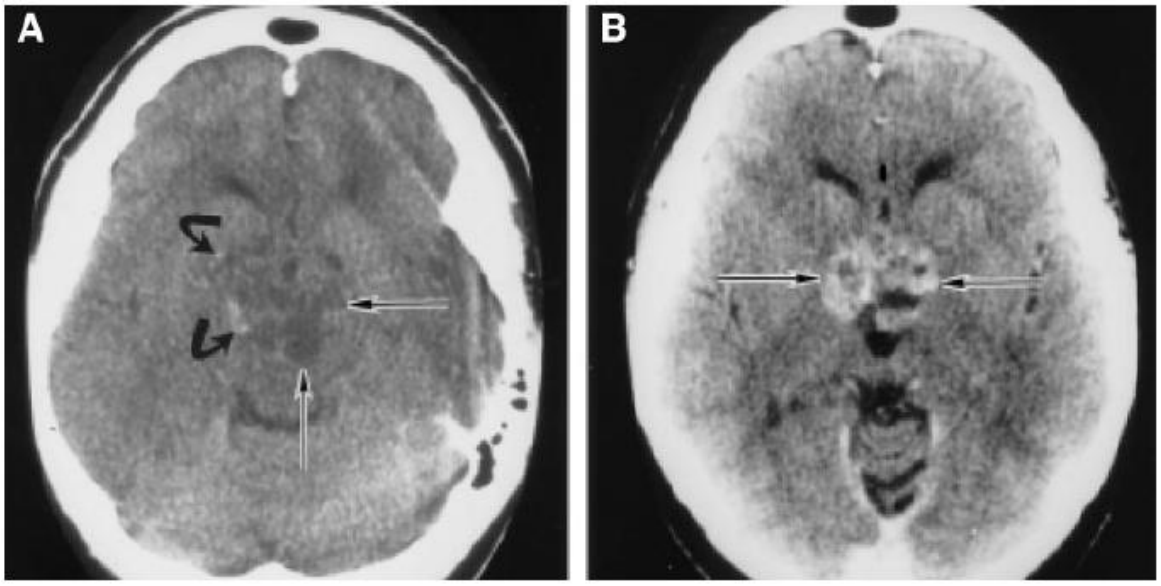

Figure 2.2.1Axial unenhanced (A) and contrast-enhanced (B) brain demonstrate a craniopharyngioma locating suprasellar region with different contents

MRI makes use of the property of nuclear magnetic resonance to image nuclei of atoms inside the body. MRI, particularly after contrast enhancement, is valuable for the topographic and structural analysis of these tumours [41, 42]. The appearance of the craniopharyngioma depends on the proportion of the solid and cystic components, the content of the cyst(s) (cholesterol, keratin, hemorrhage), and the amount of calcification present. The signal of a solid tumour is iso- or hypointense relative to the brain on precontrast T1W sequences showing enhancement after gadolinium, whereas it is usually of mixed hypo- or hyperintensity on T2W sequences [43]. Calcification is difficult to detect on MRI studies, but if a large area is present, it maybe seen as a low signal on T1W and T2W sequences. The cystic component is usually hypointense on T1W and hyperintense on T2W sequences [43]. Protein, cholesterol, and methemoglobin may cause a high signal on T1W images [41], whereas very concentrated protein, calcification, and various blood products may be associated with a low T2W signal [44]. Post contrast T1-weighted images demonstrate the thin peripheral contrast-enhancing rim of the cyst [43]. Interestingly, edema in the adjacent brain parenchyma are presenting a reaction to the craniopharyngioma itself or a focal disturbance in the cerebrospinal fluid (CSF) flow

spreading along the visual pathways may be present, providing a useful MRI finding for distinguishing craniopharyngiomas from other common parasellar tumours [45, 46]. (Figure. 2.2.2)

Figure 2.2.2 Axial brain CT demonstrates a craniopharyngioma locating suprasellar region with cyst capsule and coarse calcification, and dilatation of the temporal horns of the lateral ventricles

It is reported that the proportions of the craniopharyngiomas components were different. Their consistency is purely or predominantly cystic in 46–64% of the cases, purely or predominantly solid in 18–39%, and mixed in 8–36% [47, 48]. Notably, apart from rare cases with a significant cystic component, most of the intraventricular craniopharyngiomas have been reported as solid [49]. These determine the specific treatments to different craniopharyngiomas as described below.

Apart from the inherent imaging features of craniopharyngiomas, CT or MRI also

show the pressure effects on surrounding structures, such as pituitary, hypothalamus and commissural optica. Hydrocephalus has been reported in 20–38% of the cases, it is probably more frequent in childhood populations (41–54% in children and 12–30% in adults for reasons not yet clarified [50, 47, 36]).

2.2.4 The treatment options of craniopharyngiomas

Craniopharyngiomas are an example of a benign tumour but with a malignant growth tendency. Since growth mode is unpredictable, craniopharyngiomas bring great surgical challenge, even with the advent of modern neurosurgical techniques. Their often large size, sharp and irregular margins, and their adherence to vital neurovascular structures do not allow a clear line of cleavage, and thus, make complete resection difficult and potentially hazardous to critical brain areas. Nevertheless, craniopharyngiomas have a high recurrence rate.

2.2.4.1 The surgical excision with or without adjuvant conventional external beam irradiation

Surgical excision is the primary therapy for craniopharyngiomas. The surgical approach should provide wide exposure of all parts of the tumour and minimize the damage to vital structures. Its choice depends on the location, the consistency, the degree of calcification, the shape and size of the tumour, as well as on the surgeon's preference and experience. Resection is usually attempted by craniotomy through a large number of approaches used alone or in combination for difficult tumours [51, 52, 53]. The less traumatic transsphenoidal route is best reserved for smaller intrasellar-infradiaphragmatic tumours [51, 54]. For massive lesions, a two-stage removal may be necessary: transsphenoidal debulking followed by craniotomy several weeks later. This policy may allow the tumour to descend caudally, facilitating its further resection during the second surgery [55, 56]. In cases of hydrocephalus, resection can be achieved more easily after decompression of the ventricles and stabilization of the clinical status of the patient.

Similarly, when large cystic components are present, fluid aspiration provides relief of the obstructive manifestations and facilitates the consecutive removal of the solid tumour portion; the latter should not be delayed for more than a few weeks, due to the significant risk of a cyst refilling [47].

Surgery combined or not with adjuvant external beam irradiation is currently one of the most widely used first therapeutic approaches for craniopharyngiomas. However, there tumours were considered radioresistant until 1937 when Carpenter first described the beneficial effects of radiotherapy after aspiration of cyst contents [57]. As to the recurrence rate, radiotherapy following radicality of resection show that gross total removal is associated with recurrence rates of 0–62% at 10-yr follow-up [47, 55, 52]. These are significantly lower than the ones following partial or subtotal removal (25–100% at 10-yr follow-up) [47, 55, 52]. Although not widely accepted, it has been proposed that the tumour control correlates with the irradiation dose [58, 59]. Thus, it seems likely that surgical resection combined with adjuvant external beam irradiation is the first option to treat primary craniopharyngiomas.

The management of recurrent tumours remains difficult, because scarring/adhesions from previous operations or radiation decrease the possibility of successful excision. Actually, the success rate of total removal drops dramatically (0–25%), when compared with primary surgery, and there is increased perioperative morbidity and mortality (10.5–24%), suggesting that for many recurrent lesions palliative surgery is the most realistic target [47, 52]. There was also no significant difference in the tumour control among patients offered adjuvant radiotherapy after primary surgery and those receiving irradiation for recurrence. Although the two treatment groups may not be comparable in terms of tumour aggressiveness, some of neurosurgeons proposed that radiotherapy may be equally effective at the time of recurrence [60]. Therefore, a consensus has been reached by many doctors that therapy, such as radiotherapy, are more likely to be employed to treat recurrent craniopharyngiomas instead of intracranial resection.

2.2.4.2 The intracystic irradiation

As a very important application of the brain stereotactic technique, intracystic irradiation, was first applied to treat craniopharyngiomas by Leksell in 1952 [61]. It involves stereotactically guided instillation of β-emitting isotopes into cystic craniopharyngiomas delivering higher radiation doses to the cyst lining than the ones offered by conventional external beam radiotherapy. The beneficial effect is achieved through destruction of the secretory epithelial lining causing elimination of the fluid production and cyst shrinkage [62]. Subsequent studies assessed the efficacy of various β-and γ-emitting isotopes (mainly ^{32}phosphate, ^{90}yttrium, ^{186}rhenium, and ^{198}gold); because none of them has the ideal physical and biological profile (i.e. pure β-emitter with short half-life and with tissue penetrance limited to cover only the cyst wall), there is no consensus on which therapeutic agent is the most suitable [63, 64, 65, 66].

It is worthwhile to note that the neurosurgery department of the Navy General Hospital in China performed a large number of intracystic irradiation operations employing the stereotactic technique, which achieved a good outcome [67, 68]. Sun reported that a treated group with 26 senior patients received stereotactic cystic fluid aspiration and ^{32}P intracavitary irradiation. Among them, 10 patients were treated with gamma knife surgery in solid part of the tumors. The volume of stereotactic cystic fluid aspiration varied from 1.5 to 27ml (average 11.3ml). Visual acuity and fields improved in 11 patients at different degrees postoperative instantly. No severe complications occurred in these patients. 26 patients were followed up from 12 months to 22 years (mean, 46months). The actuarial tumor control rates were 83.3%. 10 patients received combined therapy and gamma knife surgery, of which 9 were followed up. The control rates for the solid part of tumors was 88.9%. He drew a conclusion that stereotactic ^{32}P intracavitary irradiation is a simple, safe and effective method for craniopharyngiomas. For the patients who cannot endure a craniotomy or have postoperative residual and recurrent craniopharyngiomas, stereotactic cystic fluid aspiration and intracavitary brachytherapy can be used for the cystic part and gamma knife surgery for the solid part of the tumors [68].

In summary, intracavitary irradiation seems to offer a good prospect for the reduction or stabilization of cystic craniopharyngiomas. This effect, combined with its reported low surgical morbidity and mortality, renders this management option attractive for predominantly cystic tumors and particularly the monocystic ones. In the mean time, the risk of isotope leakage into the surrounding structures may be eliminated by adopting appropriate technical measures, such as accurate volume determination of the cyst and cyst puncture with a very small needle [69].

2.2.4.3 Stereotactic radiosurgery

Stereotactic radiosurgery delivers a single fraction of high dose ionizing radiation on precisely mapped targets, keeping the exposure of adjacent structures to a minimum and possibly reducing the late radiation-induced adverse sequelae. Tumour volume and close attachment to critical structures are limiting factors for its application, with 10 and 15 Gy being the maximum tolerated doses for the optic apparatus and other cranial nerves, respectively [70]. Its role in the treatment of craniopharyngiomas has been assessed in a small number of reports, which cover relatively short follow-up periods.

Yu, a neurosurgeon of the Navy General Hospital, offered combined treatment with stereotactic instillation of ^{32}P (for cystic parts) and gamma knife surgery (for solid parts) in 46 patients [mean age, 39 years (range, 3–60);28 had previously undergone total or SR with or without external beam radiotherapy, and 14 had previously received stereotactic intracavitary irradiation]. The marginal dose of gamma knife therapy was between 8 and 18 Gy, and the inner surface of the cyst wall received a cumulative dose of 250 Gy. Three subjects received another radioisotope injection due to cyst recurrence. The assessment of the imaging outcome of 38 patients after a mean follow-up of 16 months showed that the tumor control rate (disappearance, decrease, or no change) was 90% in solid and 85.7% in mixed tumors (92.1% for their solid segment) [67].

In a word, stereotactic radiosurgery achieves tumor control in a substantial number of patients with small volume lesions. It may be particularly useful for well-defined residual

tissue after surgery or for the treatment of small solid recurrent tumors, especially after failure of conventional radiotherapy.

2.2.5 Therapeutic strategy

A clear consensus on the best therapeutic approach of primary or recurrent craniopharyngiomas has not been established as yet. Based on the reports in this chapter, a therapeutic strategy is proposed and is shown in Figure.2.2.3.

As long as pressure effects appear, therapeutic intervention is suggested for all patients with imaging consistent with a craniopharyngioma. Clinical and radiological factors at presentation may guide the initial approach. When compressive signs or symptoms are evident, surgical excision is considered necessary, which in cases of predominantly cystic lesions may be facilitated by previous fluid aspiration. Resection is reasonable, provided it is performed by skilled neurosurgical hands and hazardous manipulations to critical brain areas are avoided. In view of the poor local control rates associated with radiographically confirmed residual tumours and the high morbidity and mortality after reoperation(s), in cases of non-total removal and conservative surgery, postoperative irradiation is recommended. Although this policy is debated for young children, the radiation toxicity to the developing brain needs to be balanced with the risks of a recurrent mass and subsequent possible multiple surgical procedures. In small tumors not causing pressure effects (visual, neurological, hypothalamic), radiotherapy (preceded by biopsy for confirmation of the diagnosis) offers an attractive option for avoiding the risks of surgery. In predominantly cystic craniopharyngiomas, previous aspiration of the fluid may decrease the adverse sequelae of possible cyst enlargement during irradiation.

The therapeutic decisions for recurrent disease depend on the nature of the previous interventions and the severity of the clinical picture. In recurrent lesions not previously irradiated, radiotherapy seems beneficial. Given the high morbidity and mortality accompanying repeated surgery, this option is suggested only in cases of acute pressure effects.

The plans for control of further local failure are individualized and include the alternatives of gamma knife radiosurgery, cyst controlling procedures, surgical debulking (for significant solid life-threatening component), and systemic chemotherapy.

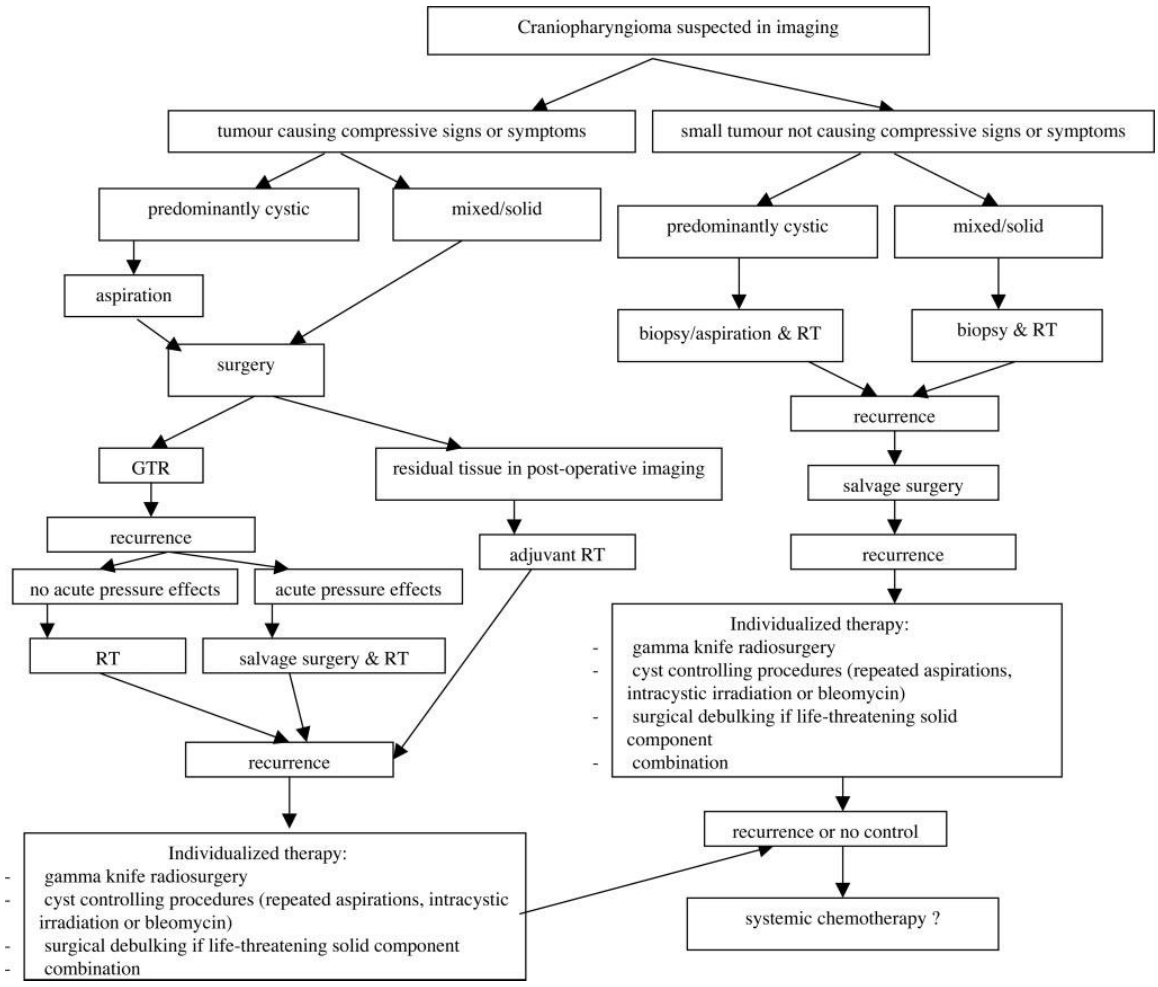

Figure 2.2.3 Therapeutic strategy of craniopharyngioma

No matter whether it is a primary or recurrence, stereotactic operation is the best technique for aspiration and biopsy of craniopharyngiomas. In addition, stereotactic operation is particularly suited to predominantly cystic craniopharyngiomas since it is minimally-invasive, effective and repeatable. Using the frame or frameless stereotactic technique, a large number of craniopharyngiomas patients received operations and

yielded desirable outcomes in the Navy General Hospital [68, 67, 9]. It is reasonable to say that craniopharyngiomas are the major form of the sellar/parasellar tumour, and the feature data of craniopharyngiomas are representative. Moreover, the same types of tumour make it simpler for analysis, comparison and induction. Therefore, image data of craniopharyngiomas were collected as research objects to analyze the relationship among the lesions, brain blood vessels and the neurosurgical path in this study.

2.3 The progress in the correction of MR images distortion

MR scanners use strong magnetic fields to form images of the human body. Most medical applications rely on detecting a radio frequency signal emitted by excited hydrogen atoms in the body (present in any tissue containing water molecules) using energy from an oscillating magnetic field applied at the appropriate resonant frequency. The orientation of the image is controlled by varying the main magnetic field using gradient coils. As these coils are rapidly switched on and off they create the characteristic repetitive noises of an MRI scanner. The contrast between different tissues is determined by the rate at which excited atoms return to the equilibrium state. As a common examination, MRI is often used for diagnosis as well as treatment, especially in the neurosurgical area. MR image guided neurosurgery is one of the favoured applications for the usage of MRI in the clinic, and has become very popular because it provides accurate, informative and high-resolution medical images. An accurate MRI requires a magnetic field that is both strong and uniform, however, the condition of a magnetic field has not always been satisfied.

2.3.1 Progress in the correction of MR images distortion before or during the process of MR scan

An unclear MR image can be caused by MRI distortions, due to undesired components such as non-linearity of the gradients and static magnetic field inhomogeneity [71,72]. Using a Fourier transform image formation method, Kawanaka

et.al sought a relationship between these undesired components and the image distortion. They also proposed a way of estimating the undesired components of fields from the image conventionally reconstructed from an appropriately designed reference object. The proposed method can be utilized not only for the measurement of static and gradient fields but also for the correction of image distortion[71]. The study focused on the distortion caused by the magnetic field, and tried to correct it before images had been generated. In other words, to correct MR image distortions during the process of an MR scan.

On the other hand, a patient's body, with different proportions of tissues (fat and muscle, etc.), will perturb the magnetic field. Motions of the patient, implantable devices, such as dentures, will also induce field inhomogeneity. Many approaches have been developed including choosing maximum read-out and slice selection gradients [72] and the registration of fiducial markers [73]. In 1992, Bakker et. al reported an approach to analyze the machine-dependent and object-induced geometric distortion in a 1.5T MR scanner. System related imperfections were measured by systematic variation of the strength, direction, and polarity of the read-out gradient in imaging experiments on a grid of cylindrical sample tubes. Field related errors were shown to be inversely proportional to gradient strength, whereas gradient related errors turned out to be virtually independent of gradient strength. These experiments revealed a negligible influence of the object on the gradient error distribution, and lead to the conclusion that correction for the nonlinearity of the gradients only requires the application of system dependent correction factors. In the study, correction of system related geometric distortions in MR images can readily be performed by looking up the distortion value and replacing by real sample parameters. However, this correction had to be done manually at that time.

In another way, the static magnetic inhomogeneity were analyzed by varying the direction of the read-out gradient in Moerland's study in 1995 [73]. For the purposes of accuracy assessment, external and internal landmarks were inducted in their study. Tubes attached to the cast and in the localization frame served as external landmarks. In the midsagittal plane the brain-sinussphenoidolis interface, the pituitary gland-sinus

sphenoidalis-interface, the sphenoid-bone and the corpora of the cervical vertebra served as internal landmarks. Landmark displacements as observed in the reversed read-out gradient experiments were analyzed with respect to the contributions of machine-related static magnetic field inhomogeneity and susceptibility and chemical shift artifacts. The result showed that machine-related, chemical shift and susceptibility-induced static magnetic field inhomogeneity were of the same order, resulting in spatial distortions between -2mm and +2mm with only negative values for the chemical shift effect. After correction for the machine imperfections and susceptibility artifacts, the geometric accuracy of the landmark in the localization was better than 1.3 mm. Thus, Moerland and his colleagues developed an approach to intensively analyze the factors causing field inhomogeneity and corrected the distortion separately.

In 1995, Maciunas et. al also reported a universal method for geometric correction of MRI [74]. In their study, patients with a so-called Kelly-Groerss modified Todd-Wells stereotactic frame and implantation of four skull-mounted fiducial markers underwent imaging with MR scans. As the reference, CT images were acquired simultaneously. After obtaining each MR image, an additional MR image was acquired with identical imaging parameters, except that the read-out gradient was reversed. The MR images were corrected for scale distortion by using the stercotactic frame as an object of known shape and size to estimate a scale factor for the three directions. A new image, without inhomogeneity distortion, was then generated from the pair of distorted images acquired with reversed readout gradient. The Euclidean error of the distance between the target centroids in MR was calculated as the target registration error. As a result, the Euclidean error in target registration between CT and MR was significantly reduced.

In the same year as Maciunas's study was published, Balac and Caloz reported their study concerning MRI distortion caused by magnetic susceptibility artifacts [75]. Since some of the artificial implants, a paramagnetic material for instance, have magnetic properties, they might disturb the magnetic field in the MR scanner. In their study, a mathematical model was employed to numerically compute the disturbances induced by the implant. Since the method is linked to an artifact reconstruction model to get

simulated images, it has to be well suited for general three dimensional geometries and to provide very accurate results in a fine grid around the implants.

At present, each MR scanner used in almost all the modern polyclinic hospitals has its own module to reduce the machine-related distortion to a minimum level automatically, and head motions can be detected by some modules [76], but it still cannot eliminate the distortion entirely. For example, the motions of the patient during the MR scan, metal implants in the body and the flexible background magnetic field might lead to inevasible MR image distortions which could rarely be eliminated by the integrated modules. Therefore, another method that will possibly wipe out MRI distortions by analyzing the existing MR images is required.

2.3.2 Progress in the correction of MR images distortion after the process of MR scan

All the methods, as described above, for detection and correction of MRI distortions were performed by measuring the gradient of the magnetic field or using spatial markers. These approaches need standard samples or similar devices beforehand, and then analyze the relationship between the original objects and output MR images. These have to be done before or during the process of an MR scan, which in turn develop the accuracy of subsequent MR images. To analyze the existing MR images, other references need to be introduced.

A number of approaches have been tried to analyze MRI distortions with reference to CT images that are considered as distortion-free. One of the most popular algorithms applied in registering two sets of image data was presented by Arun et.al, based on the singular value decomposition (SVD) of a matrix, for finding the least-squares solution of distortion factors [77]. The SVD, in linear algebra is a factorization of a real or complex matrix, with many useful applications in signal processing and statistics. It is also very popular in data processing and information analyzing [78]. In their study, two 3D point sets (p_i); i=1, 2, 3…, N (here, p'_I are considered as 3×1column matrices) were given

$$p'_i = Rp_i + T + N_i \quad (2.1)$$

where R is a 3×3 rotation matrix, T is a translation vector (3×1 column matrix), and N_i is a noise vector (Formula 2.1.). The SVD of the 3×3 matrix was used to find the least-squares solution for minimizing R and T. This algorithm has been used in the registration of two sets of fiducial markers originating from CT and MR images, and inspired a number of scientists to expand it. Subsequently, a series of algorithms and applications were developed based on Arun's study. However, as an important parameter, a scaling factor had not been determined in Arun's procedure (Figure 2.3).

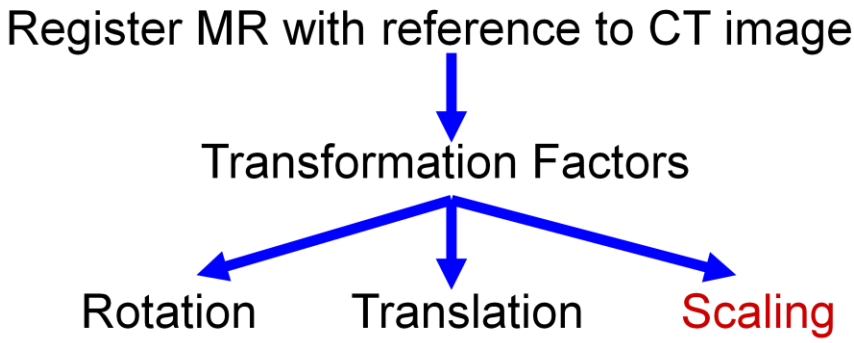

Figure 2.3 Schematic diagram of decomposing distortion factor into rotation, translation and scaling factor

Based around a singular value decomposition similar to Arun et.al, Challis expanded their algorithm to allow for the determination of a constant scaling factor [79]. The procedure, which requires the coordinates of three or more noncollinear points, is based around the singular value decomposition, and provides a least-squares estimate of the rigid body transformation parameters. In his study, the procedure was used to determine the attitude of a rigid body, and for osteometric scaling.

In order to estimate the medical imaging distortion from two m-D point set patterns, the classic least square algorithm using SVD was often used, but the algorithm was not perfect. Ramos et. al improved the least square algorithm and proposed a formulation by the use of total least squares, where both data sets are treated as noise [80]. Here, the

noise vector was emphasized as an important parameter because 2 sets of image data could be corrupted by noise. The new algorithm takes advantage of the noise structure in the data. That is, they assumed there was noise present in both data patterns, as well as a noise-free column for the translation vector. Also, the proposed algorithm computed all the parameters at once, without averaging the data. In their study, they treated the image registration problem from a mixed least square-total least square point of view, and gained positive results.

These algorithms consider the noise as coming from one image only, when in fact both images are corrupted by noise. In addition, these algorithms may suffer from round-off accumulation errors due to an SVD of a matrix product between two noises corrupted matrices.

CT is considered as distortionless because the X-ray, which is used by CT scanners to generate images, penetrates the tissues of human's body in a straight line with little diffraction. Thus, CT images are often referenced by MR images to correct MRI distortions. In Alexander's study, an image fusion technique based on a chamfer matching algorithm was used to eliminate MR image distortion. The fusion process relies on the automatic segmentation of the surfaces of the bony anatomy in both CT and MR volumes. The bone surfaces from CT are aligned to the bone surfaces in MR using the chamfer matching method. As the result, the post fusion images between the CT and MR anatomy as visualized by the soft tissue components inside the skull are quite overlapping [81].

Similarly, Cohen et al demonstrated that a method of co-registered CT and MR images by matching cranial landmarks in the two scans, and software which was based on least-squares fitting was used to make comparisons among all the landmarks. They testified that their method has increased MR image accuracy [82]. Eggers et. al scanned two human cadaver heads using MRI, while CT scans of the same heads were used as a benchmark. Using a stereotactic frame, corresponding images of MRI and CT were superimposed and the concordance of the images of the mandibular nerve in MRI with

those of the mandibular canal in CT was assessed. Eventually, they drew the conclusion that MRI of the mandibular nerve is sufficiently accurate [83].

The algorithms mentioned above are widely employed in medical registration, which are applied generally to register MR images with reference to CT images or to coregister them with each other.

2.3.3 Progress in the correction of MR images distortion using spatial references

In recent years, a number of methods have employed special phantoms for mapping geometric distortions in MR images. The phantom described in Wang's et al paper was designed based on the concept that a point in space can be defined using three orthogonal planes. The phantom contained over ten thousand control points to ensure the accuracy of the mapping system [84]. It was also reported in another paper that a large 3D phantom with spherical balls was used to characterize geometric distortion [85]. Although it is an effective way to correct MR distortion in accordance with a hypostatic phantom, it is still hard to realize without powerful engineering technical support.

In this research, we seek to develop a new way to detect and eliminate MR distortion, ensuring MR data in this study are accurate and reliable. The method will be described below.

2.4 Overview of cerebral vascular system

As a great oxygen expenditure organ of the human body, more than 20% of the oxygen we breathe is consumed by brain. It must receive a sufficient blood supply otherwise cerebral ischemia symptoms such as megrim, apopsychia and limb weakness may occur [86]. There are four ascending arteries that supply to the cerebral circulation; two carotidarteries and two vertebral arteries. Some variation is occasionally found in these vessels. The left common carotidartery derives directly from the aortic arch, while

the right common carotid emanates from the brachiocephalic artery coming from the aortic arch. The brachiocephalic artery derives to the right vertebral artery. The 3rd major artery to branch off the aortic arch is the left subclavian artery. The left vertebral artery branches off the left subclavian shortly after it branches out from the aortic arch. (Figure. 2.4.1)

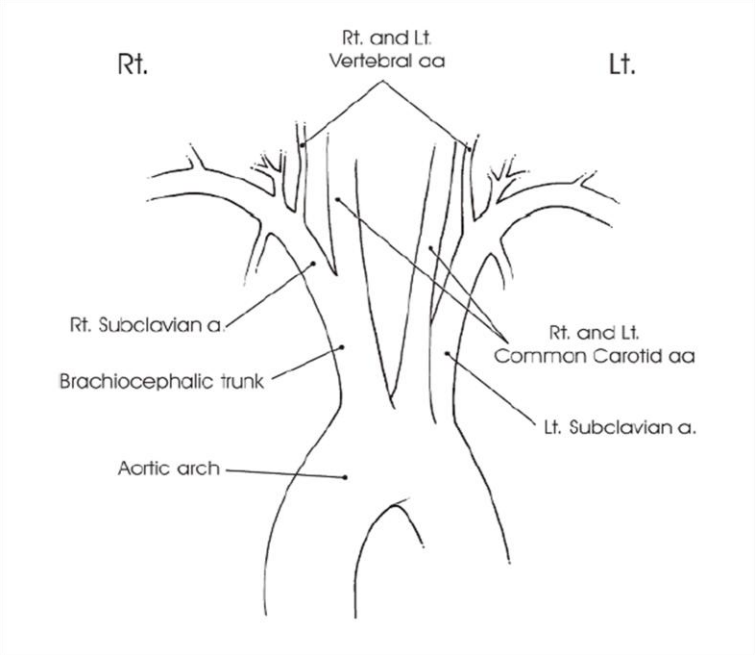

Figure. 2.4.1 Carotid and vertebral arteries deriving the aortic arch and secondary vessels

2.4.1 Carotid system

The common carotid arteries also proceed in a rostral direction in a more anteriorposition in the neck. At nearly the level of the fourth cervical vertebra, the common carotids bifurcate, forming the internal and external carotidarteries. The latter go on to supply the extracranial tissues of the face and most parts of the dura. The internal carotid arteries go ahead into the cranial cavity where they eventually give rise to the right and left anterior (ACA) and middle cerebral (MCA) arteries, the four remaining cerebral vessels.

Just prior to entering the circle of Willis (see below) where the internal carotid and vertebral systems confluence via connecting vessels or communicalis arteriae, the internal carotids give rise to two major vessels, the ophthalmic artery and the anterior choroidal artery. Besides to supplying structures around the eye and the anteriorportion of the dura, one branch of the ophthalmic artery enters the eye goes along with the optic nerve and supplies the retina. The anterior choroidal artery will be described in greater detail later. As its name shows, it is important in supplying the choroidplexus (lateral ventricles), but also supplies parts of the visual and motor systems structures and the temporal poles.

2.4.1.1 Circle of Willis

The internal carotid communicates vertebral vascular systems at the base of the brain, anterior to the brainstem and beneath the optic chiasm (Figure. 2.4.2). This communication or anastomosis is known as the circle of Willis, a 17th century anatomist (Thomas Willis, 1621–1675). The circle of Willis provides a potential blood flow for collateral blood supply following the possible block of one of the major cranial arteries feeding into it. However, this potential collateral system has big variability by different individuals and can be influenced by several factors. This “circle” is formed by the presence of “communicating” arteries that link the right and left internal carotids by the vertebral circulation. Just rostral to the third cranial nerves, slightly posterior to the mammillary bodies, the basilar artery bifurcates, turning into the right and left posterior cerebral arteries (PCA). Close to the bifurcation, each posterior artery sends an anterior branch that connects to the internal carotidsipsi laterally. These connecting vessels are the posterior communicating arteries.

As to the bilateral internal carotids, they divide into the middle and anterior cerebral arteries. The middle cerebral artery (MCA), which is the primary extension of the internal carotid, goes dorsal-laterally up through the lateral fissure between the temporal and frontal lobes. The anterior cerebral artery (ACA) initially remains more medial as it proceeds anteriorly toward the frontal lobe, goes through the fissurae interhemisphaerica.

Just anterior to the optic chiasm, the anterior communicating artery connects the two anterior cerebral arteries, in turn completing the circle.

However, the above description of the circle of Willis represents the more typical pattern, some individual variations may be noted. Although the presence of a completed "circle" in the majority of individuals, since there is little "communication" between the right and left internal carotids via these communicating arteries, they may not be much blood flowing around the circle. This relative lack of flow around the circle of Willis seems primarily to be the fact that: 1)the interconnecting arteries themselves are often relatively small, 2)there is relatively equal hemodynamic pressure from one arterial system to the other arteries, thus not encouraging flow between the systems. Nevertheless, if at a certain time one of the major arteries, one of the internal carotids for instance, becomes gradually stenosed, a pressure gradient makes the shunting of blood from one side to the other artery. As a result of this shunting of blood flows through the posterior and/or anterior communicating arteries, the interconnecting arteries gradually enlarge, creating a larger flow, thus facilitating more shunting of blood. So, it is possible to find that a fairly complete thrombotic occlusion of one internal carotid arteries with little if any clinical manifestations of compromise of cerebral blood flow [86]. But, if such an occlusion were to occur more acutely, as a result of an embolus for instance [87], the interconnecting vessels would not have time to adapt and a major stroke is likely to ensue.

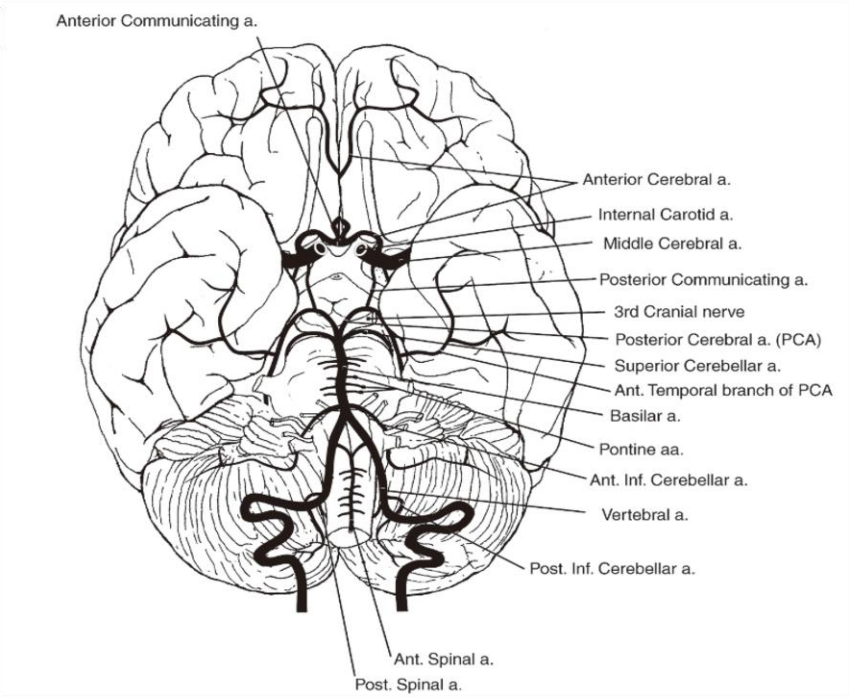

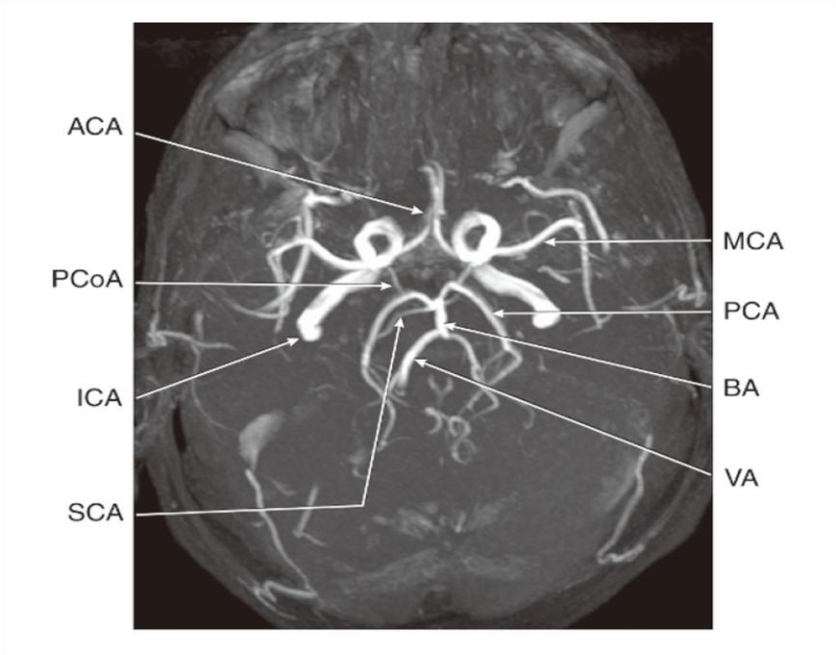

Figure. 2.4.2 Ventral view (sketch and MRA) of vertebral–basilar system and its relationship to the brainstem and carotid circulation

The "circle of Willis" is creating anastomoses between the posterior and carotid circulations. Figure below: MRA showing same vessels from axial perspectives.

2.4.1.2 Anterior Cerebral Artery

As described above, the ACA originates at the bifurcation of the internal carotid into the middle and anterior cerebral arteries. The ACA, normally smaller than the MCA, proceeds frontally along the base of the frontal lobe. Shortly after their site of origin, the anterior communicating artery links the two ACAs. Aneurysms have a tendency to develop at sites where proximal branching of the arteries occurs [88], and the ACA is a common site for such aneurysms. After to the anterior communicating artery, the main branch of the ACA proceeds anterior-dorsally through the fissure interhemispheric. It then curves around the corpus callosum genu and crawls the corpus callosum posteriorly along its dorsal surface in the callosal sulcus, which seats between the corpus callosum and the cingulate gyrus (Figure. 2.4.3). This part of the ACA is known as the pericallosalartery. Normally, a second more dorsally positioned branching of the ACA follows the cingulate sulcus, namely the calloso marginal artery. The anterior cerebral artery also sends off secondary arteries that supply such as the orbital, front lobe polar and the medial frontal and parietal cortices, including most if not all of the cingulate gyrus. Branches of this artery also supply the genu and more or less the anterior two thirds of the corpus callosum body, as well as parts of the anteroventral striatum and the anterior limb of the internal capsule. As shown in (Figure. 2.4.4), the distal branches of this anterior system also tend to overlap slightly onto the dorsal–lateral surface of the frontal and parietal lobes.

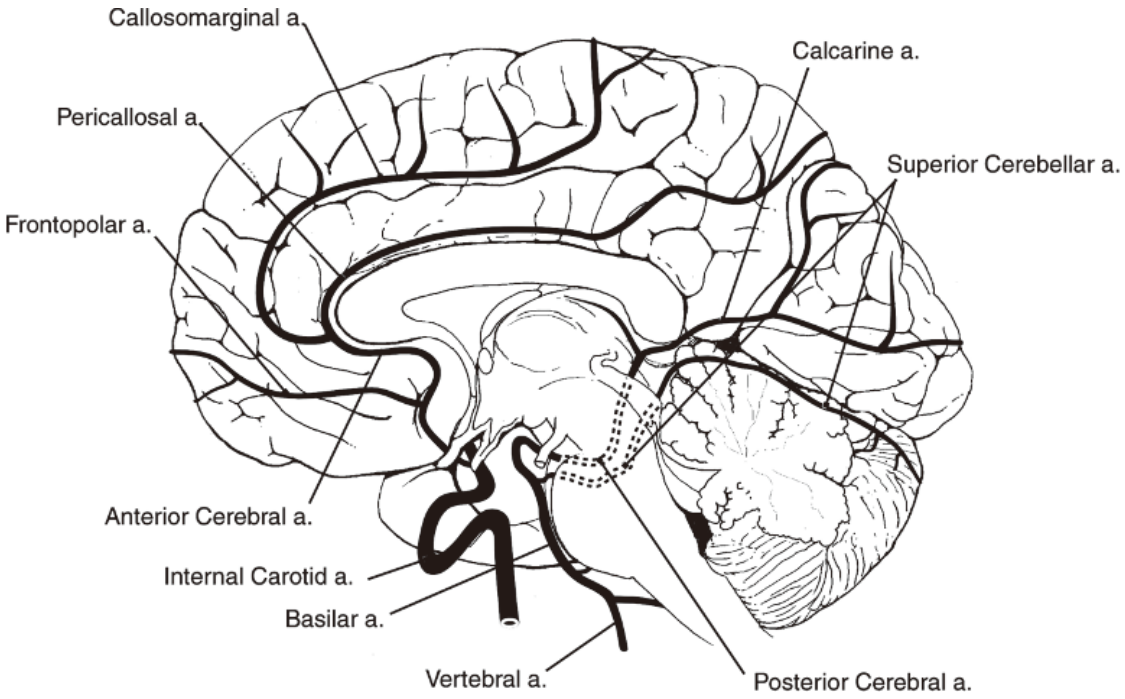

Figure.2.4.3 Midsagittal view of the cerebral hemisphere shows the general distribution of the main branches of the anterior and posterior cerebral arteries

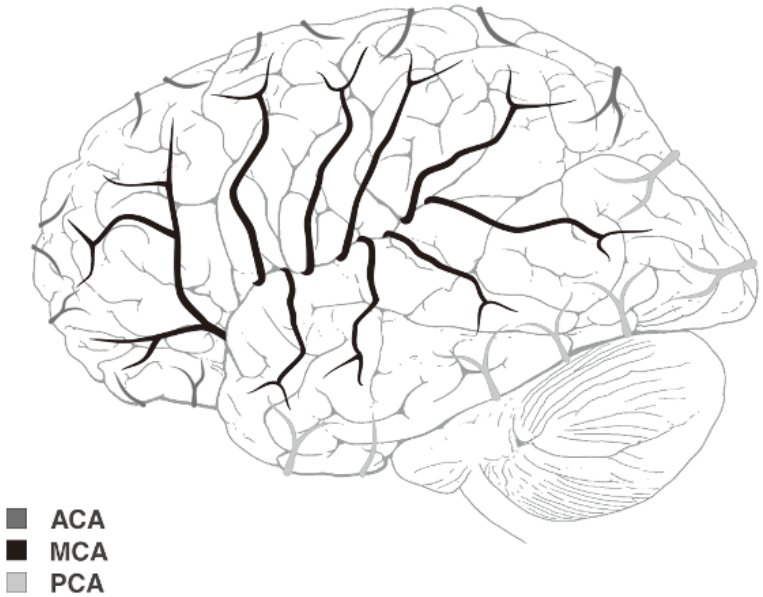

Figure 2.4.4 Lateral view illustrates the distribution of the middle cerebral artery

The main trunk of the MCA comes off the internal carotid and reaches the surface of the hemispheres by passing through the lateral fissure. As illustrated in Figure.2.4.4, the

anterior and posteriorcirculations are most prominent on the medial surface of the cerebral hemispheres, but also extend slightly onto the lateral surface of the hemispheres where they anastomose with the terminal branches of the MCA.

2.4.1.3 Middle Cerebral Artery

The larger middle cerebral artery is most likely the direct continuation of the internal carotid artery. This, combined with its larger inradium, and forming greater hemodynamic flow, increases the probability that emboli emanating from the heart or carotid vessels will affect the distribution of the MCA [89] rather than going up through the ACA. After dividing from the terminal end of the internal carotid, the MCA goes dorsolaterally into the lower aspect of the lateral fissure. Within the frontal–parietal operculum in the region of the insularcortex, the MCA separates into various cortical branches (varying from one individual to another) that come off from the superior surface of the lateral fissure. These MCA branches including the orbitofrontal, prefrontal, central, postcentral, anterior and posterior parietal, angular, and the posterior, middle, anterior and polar temporal arteries supply almost the whole lateral convexities of the frontal, parietal, and temporal lobes. This adds up to most of the lateral surface of the brain. The MCA also provides blood flow to the cortex of the insula and the claustrum. Penetrating arteries such as medial and lateral lenticulostriate arteries, coming off the MCA, supply other internal subcortical structures. The terminals of both the anterior and posterior cerebral arteries, which mainly supply the medial cortical surfaces, extend slightly onto the dorsolateral and ventrolateral surface of all lobes where they overlap with the terminals of the MCA. This region of overlap is indicated to as the watershed or border zone areas, and as we shall see may become important in certain hypotensive states [89] or in some cases infarction of the internal carotid artery and hypertension.

2.4.2 Vertebral system

The vertebral arteries proceed in their rostral course along the ventral surface of the

cervical spine and become encased in its bony processes, namely the transverse foramen. After entering the foramen magnum, the vertebral arteries lie adjacent to the ventral surface of the medulla in the brainstem, namely the basilar sulcus. Then, these two vertebral arteries join to form the singular basilar artery at the level of the pontine–medullary junction (Figure. 2.4.2and 2.4.5). Finally, the basilar artery itself will bifurcate just above the pons, at the level of the midbrain, emit the two posterior cerebral arteries (PCA). As shown in Figure. 2.4.2 and 2.4.3, there are several prominent cortical branches of the PCA such as the parietooccipital artery, the calcarine artery (which supplies Brodmann's area 17, the primary visual cortex), the anterior and posterior temporal branches of the PCA (supplying the ventral and medial surfaces of the temporal lobes, including parts of the hippocampus).

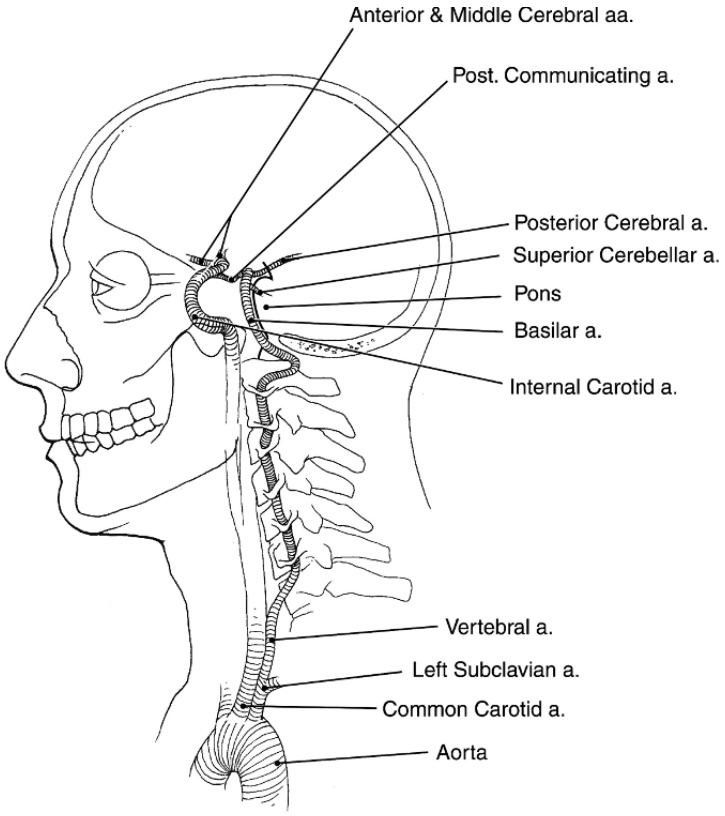

Figure 2.4.5 Lateral view of the vertebral–basilar system shows its relationship to the internal carotid artery

The Figure also shows the distal part of the vertebral artery passing through the transverse processes of the cervical vertebrae before entering the foramen magnum and forming the basilar artery.

In addition to the posterior cerebral arteries, the vertebral and basilar arteries emit multiple branches throughout their course along the brainstem. These branches, as shown in Figure 2.4.2, represent the main source of blood supply both to the brainstem and the cerebellum, as well as to the cervical part of the spinal cord. There are three main branches of the vertebral arteries: 1) the anterior spinal artery, 2) the posterior spinal arteries, and 3) the posterior inferior cerebellar arteries. After the vertebral arteries join to form the basilar artery, the latter emit two other major vessels supplying the cerebellum and brainstem: the anterior inferior cerebellar and the superior cerebellar arteries. The anterior inferior cerebellar artery supplies the anterior and inferior parts of the cerebellum and the caudal pons. The superior cerebellar artery supplies the superior aspect of the cerebellum, the rostral pons, and portions of the midbrain. Other smaller arteries, namely pontine branches derived from the basilar artery and supply brainstem structures, particularly the pons. The areas supplied by the posterior cerebal artery will be described below.

2.4.3 Posterior cerebral artery

As mentioned earlier, the posterior cerebral arteries are part of the vertebral system and are formed by the bifurcation of the basilar artery. After their origination at the level of the midbrain, they round posteriorly around the midbrain with the main trunks remaining on the medial surface of the occipital–temporal lobes (shown in Figure2.4.3). Branches of the PCA supply the inferior and medial part of the temporal lobe, except for the temporal pole. This includes part of the hippocampal gyrus and the parahippocampal and occipitotemporal gyri. However, part of the hippocampus is supplied by the anterior choroidalartery. As shown in Figure2.4.3, occipital branches of the PCA supply the medialportions of the occipital lobe, the lingual gyrus and cuneus, including the primaryvisual cortex, and parts of the medial superior parietal lobule. The

corpuscallosum splenium also is supplied by the PCA system. Similar to the above, the terminals of the PCA tend to overlap and anastomose with the terminal branches of the ACA and the MCA both on the margins of the lateral convexities as well as on the medial surfaces of the hemispheres.

2.4.4 Summary of the arterial blood supply to the brain

In general, the brainstem (midbrain, pons, and medulla) and cerebellum as well as the upper part of the spinal cord primarily are supplied by vessels arising from the vertebral and basilar arteries. A part of midbrain structures also are supplied by the anterior such as substantia nigra, and posterior such as tectum. The lateral convexity of the cerebral hemispheres is basically supplied by the branches of the MCA, which along with the ACA come off from the bifurcation of the internal carotid arteries. However, both the ACA and PCA overlap the distribution of the MCA on the margins of the lateral surface of the hemispheres.

The inferior and medial surfaces of the hemispheres are supplied by the ACA and PCA. The ACA supplies the orbital and medial surface of the frontal lobes, including the sensorimotor regions for the lower limbs and most of the remaining medial parietal cortices, the cingulate gyrus, and most of the anterior 2/3 of the corpus callosum. The PCA supplies the medial surface of the occipital cortex, including the visual areas, parts of the medial superior parietal lobule, most of the medial and inferior temporal lobe, and the splenium of the corpus callosum.

The basal ganglia primarily are supplied by the lenticulostriate arteries that emit from the proximal part of the MCA. However, parts of these structures also are supplied by the anterior choroidal artery and small vessels emiting off the posterior communicating artery. The thalamus mainly is supplied by the smaller vessels that come off the PCA and posterior communicating arteries, including the thalamoperforating, inferior thalamic, thalamogeniculate, and posterior choroidal arteries. The anterior choroidal arteries also may make a minor contribution to these areas. The anterior hypothalamus mainly is supplied by the small penetrating, anteromedial vessels deriving from the ACA and/or

anterior communicating artery surround the circle of Willis, while the more posterior part of the hypothalamus are supplied by the posterior penetrating arteries.

Most of the anterior and posterior limb of the internal capsule also is supplied by the lenticulostriate arteries. Small arteries that derive directly from the internal carotid may supply the genu. The anterior choroidal artery normally supplies some of the more ventral portions of the posterior limb, as well as the retrolenticular portions.

The visual system is supplied by multiple vessels. The retina of each eye is exclusively supplied by its corresponding ophthalmic artery from the internal carotid. The optic nerves, optic chiasm, and the initial segment of the optic tracts mainly are supplied by the penetrating arteries derived from the ACA and the anterior communicating artery. Small vessels from the internal carotid or middle arteries primarily supply the more anterior part of the optic tract. The more posterior parts of the tract, along with parts of the lateral geniculates, are supplied by the anterior choroidal arteries. The lateral geniculates are supplied by the posterolateral penetrating arteries of the posterior artery system. The superior optic radiations are supplied by the posterior cortical branches of the middle cerebral artery, while the inferior radiations are supplied by the posterior cerebral artery (PCA). The primary visual cortex and parts of the secondary visual cortex are supplied by the PCA as well.

The motor system also is subserved by a variety of vessels [89]. The disruption of any of these vessels can produce a weakness or paralysis. The primary motor cortex that conducts the face, hands, and trunk is supplied by the MCA, whereas the legs, especially the lower legs and feet, are represented on the medial surface of the hemispheres, and thus are supplied by the ACA. The MCA and ACA watershed territory supplies the motor cortex that mediates control of the proximal arm and proximal leg. The basal ganglia and internal capsule primarily are supplied by the lenticulostriate arteries (branches of the MCA), although some input is derived from the anterior choroidal and posterior penetrating arteries. The corticospinal tracts are supplied by various small vessels deriving both from the internal carotid and posterior cerebral artery systems at the level of the midbrain and by branches of the basilar and vertebral arteries at the level of the

pons and medulla. The cerebellum, the disruption of which can lead to difficulties with balance, coordination, and weakness, is supplied by the superior cerebellar artery, the anterior and posterior cerebellar arteries that derive from the vertebral system.

The arterial blood supply pattern described above is extremely important to clinical practice as well as the research in this study. It provides the theoretical basis for building the vascular template study which is described below.

2.5 Progress in building a vascular template

As a key principle in neurosurgical path planning, avoiding brain vessels should always be complied with. Therefore, the vessels must be visible to the neurosurgeon during the process of path planning. Although vascular angiography is the best way to show the brain vessels and the golden criterion to diagnose cerebrovascular diseases, MRA is another essential examination to the cerebrovascular system, and the latter is much easier to acquire. Building an average distribution architecture of brain vessels as a template and implanting the template in to patient's MR images, will help the neurosurgeon to design a safe surgical path.

As described before, the basic cranial arteries including the circle of Willis are the trunks of the brain arteries system, while arterial branches extending from the trunks are much smaller. In clinical practice, arterial branches are rarely a hazard for the biopsy needle or the electric pole because of the blunt tips of these operative instruments and the significant difference of diameters between the vessels and tips. Otherwise, it leads to the disastrous outcome if the artery trunk was damaged by any surgical instrument. Undoubtedly, to perform a safe stereotactic operation, cerebral vessels must be considered by the neurosurgeons using their experience or a visible vascular distribution pattern. The aim of this study is to rebuild a visible cerebral vascular distribution pattern derived from the existing MRA data, which in turn guides the stereotactic operation.

2.5.1 Progress on the calculation of mean dataset

The difficulty facing the calculation of an average shape from a group of similar shapes lie in the fact that there are no correspondences between those shape points, which is attributed to unequal numbers of shape points between sample data, the deformable nature retained by these points, and the unavailability of standard representations of those deformable/non-rigid shapes. As a result, in the field of computer vision, representation of shapes involves mathematical modelling using a type of constrained and non-negative functions, which has directly led to the requirement of proper statistical models on appropriately constrained functional spaces. Subsequently, consideration must be given to metrics, probability models and estimators underpinning those representations. As such, re-parameterisation of shapes, also known as non-rigid registrations, whereby noise is usually taken into account [90], should be invariant of representation spaces as well as being easy to implement. Towards this end, in addition to classic curves and surfaces, which are a natural choice but difficult to perform statistical analysis, a number of representations have been proposed very recently built on statistical models. In [90], researchers propose a "spherical" version of the Fisher-Rao metric for imposing Riemannian structure on a collection of related spaces: the space of probability density functions, time-warping functions, re-parametrization functions, etc. For another example, in [91], a new joint clustering and matching algorithm is proposed which proceeds in three steps involving clustering, non-rigid mapping estimation and mean shape estimation. Alternatively, in [92], a divergence approach is employed through the definition of Havrda-Charvat entropy to contend with the dissimilarity between point sets.

To define a statistical model of shapes, the underlying space is not a vector one but nonlinear (differentiable) manifolds, which has led to the employment of Riemannian geometry, within which, points can vary smoothly from one to another owing to the formula of inner product on a tangent space. Consequently, the drive to measure the distance between two probability distributions has seen a direct rise in the number of applications of the Fisher-Rao metric recently, seven decades after it was first published in 1945 [93]. More recently, it has also been opted for [94] to construct a

neuroanatomical shape atlas with a very promising result. In addition, as a probability model, square-root density function is resorted to in this paper since it appears to offer the only one invariant of re-parameterisation.

2.5.2 Progress on the vascular skeletonisation

Although modern CT or MR scanners have implanted modules to reconstruct arteries, veins and other structures into 3D versions, it only shows an individual pattern of these structures rather than a common pattern. As to the brain vessels, a common cerebral vascular distribution pattern provides more useful information to the neurosurgeons in case they cannot acquire patients' individual vascular images for some reason. The Thinning algorithm is widely use by many studies, such as medical surface reconstruction, medial line extraction and generating medial faces [95]. In She's study, a novel 3D Thinning algorithm, which takes advantages of both parallel and symmetry, is developed. This algorithm was validated by 3D image analysis, and the skeleton of 3D objects derived from it presents high quality. For instance, the skeletons are accurate, one voxel wide (the minimum unit), and the texture of 3D objects were entirely preserved. Moreover, the computation of the algorithm is efficient and fast, invariant to rotation, and rarely affected by noise and objects boundary complexity.

In this study, skeletonisation is one of important step to build a cerebral vascular template. A similar algorithm is employed by this study to extract the middle line of cerebral vascular, and the details will describe below.

2.6 Progress in surgical path planning image guided neurosurgery

Since neurosurgical stereotactic operation has unparalleled advantages in treating craniopharyngiomas and such brain diseases, as described above, stereotactic equipments and techniques are widely applied in the most of polyclinics. Basically, the image guided

stereotactic system, no matter frame or frameless, consists of three main components: a medical images acquiring subsystem, including MR or CT scanner, data transit pathway and images matching tools; a stereotactic planning system which provides a platform to display the images in 3D version and help neurosurgeons to design a virtual surgical path from the surface of the brain to the target; a stereotactic localization and placement procedure to perform the operation on the patient. The equipments and operating processes are described in detail in the next chapter. In the whole process of stereotactic operations, neurosurgeons may pay more attention to surgical path planning because it impinges directly upon the outcomes of the operation.

Modern stereotactic planning systems are computer based. Generally, a surgical path planning module in a neurosurgical operative system is composed of an integrated manipulative platform which includes hardware, such as postural localizers or robots, and software such as a surgical operating system. The module provides an interface for neurosurgeons to design a surgical path from their clinical experience. The interfaces of common platforms of frame and frameless stereotactic operative systems are shown separately in Figure2.5:

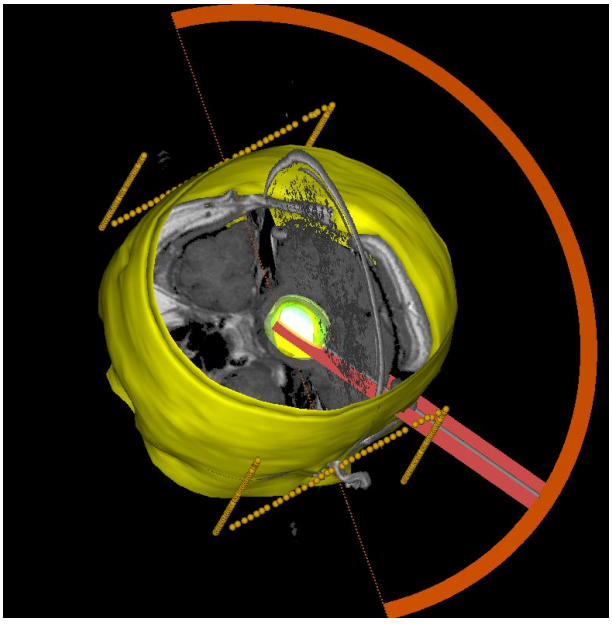

Figure 2.5 Interface of frame stereotactic operation for Craniopharyngioma

The platforms are usually maneuverable like common computer applications. After reconstruction, medical images, such as MR and CT images, are shown in 3D which are easy to observe and analyze. A series of medical images can be displayed integrally or slice by slice. Depending on this, neurosurgeons will be able to segment the lesion, select the path target and design the surgical path. At present, the main factors attributed to the definition of a path for a neurosurgeon is the location, size, and shape of a lesion. Although a patient's pathology also affects the path planning, the former three are paramount considerations. A proper surgical path must have relative minimal distance between the brain surface and the target without passing through blood vessels, nuclear, ventricles, functional areas and other important anatomic structures. In the meantime, because of the delicate nature of the brain and the complexity of brain structure, path planning is only conducted by experienced surgeons manually.

2.6.1 Progress in medical images visualizing and surgical path planning

Although the operator's clinical experience seems indispensable in surgical path planning, some of the scientists are trying to automate this process. Recently, it was reported in some papers that the analogous path could be worked out automatically not only in an industrial realm but also in medical treatment [96, 97, 98]. Elnagar et.al, employing Java, developed an autonomous robot motion planning system which could visualize each phase of the planning process graphically [97]. The path planning system involves several phases: collision detection, obstacle avoidance, free-path generation and then selecting the shortest one. A collision-free path would be figured out after four phases' computing.

On the other hand, a group of scientists in Massachusetts Institute of Technology Artificial Intelligence Laboratory developed a software package integrating several modules which provide capabilities for automatic registration, semi-automatic segmentation, 3D surface model generation, 3D visualization, and quantitative analysis of various medical scans [98]. The software had covered all the common medical imaging

methods, even including real-time intra-operative MR scans, providing a very intuitive platform to neurosurgeons. Depending on the platform, neurosurgeons could easily realize the relationships among the lesions, blood vessels, functional regions, cranial bones and other anatomic structures. In that case, to design a safe and reliable surgical path was no longer difficult.

Similarly, a novel interactive technique has been presented that facilitated path planning of surgical therapy in epilepsy for neurosurgeons [99]. The technique compounded multi-data obtained from MRI, CT, fMRI or PET together and enable them to be visualized. The modules allow surgeons to control the shape of the region of the brain that they can visually analyze and modify during exploration and surgery. The basic shapes such as simple spherical, cubical, ellipsoidal and cylindrical are provided for exploration purposes. In addition, it integrated a cropping tool with the image-guided navigation system used for epilepsy neurosurgery. These techniques simplified the procedures on deciding a safe and reliable surgical path. However, it was one step away from automatic path planning since neurosurgeons still had to set the surgical path manually in the process. Although it had not been a proper automatic path planning system, their development provided the basis for later studies in this research area.

2.6.2 Progress in automatic surgical path planning

In 1997, Vaillant et.al developed a widely accepted computer algorithm for determining optimal surgical paths for neurosurgical operation [100]. The algorithm computes a cost function associated with each point on the outer brain boundary, which is treated as a candidate entry point. The cost function is determined based on both a segmentation of the patients images into gray and white matter, and a spatially transformed atlas of the human brain registered to the patient's MR images. The importance value of various structures, such as functional areas, tracts and nerves, can be defined on the atlas and transferred onto the patient's images through the spatial transformation. The cost of a particular path associated with each critical structure, as well as the total cost of each path are computed and displayed, allowing the surgeon to

define a low cost path, to visualize an arbitrary cross-section through the patient's MR images that contains this path, and to examine all the cross-sectional images orthogonal to that path. This algorithm could be employed to design not only craniotomic operations but also stereotactic operations.

Fuji et.al described a method of automatic neurosurgical path searching, which integrated the structure of blood vessels obtained from magnetic resonance angiography and brain tissues [101]. Magnetic resonance angiography (MRA) is a group of techniques based on MRI to image blood vessels whereby a special contrast agent is administrated to patients to highlight the artery trunks, such as the Circle of Willis [102]. Their path searching consisted of four steps:

1. each region of brain tissue was classified into four degrees (importance value 0-3) indicating the importance of each different area, then working out the sum of the importance values for each possible path;

2. a module integrated structure of blood vessels picked up the optimal path candidate which keeps furthest distance from each vessel;

3. the paths which have the minimum value could be regarded as the path candidates indicating the safest paths;

4. a path smoothing module reformed the shape of the path candidate to a perfect solid line which could, consequently, guide the surgical operation. Although Fuji et.al provided a comprehensive system to help neurosurgeons design a perfect path, the classification of the importance value is not so specific and MRA is too extravagant for ordinary hospitals and average patients. Therefore, the search for optimal neurosurgical path planning is far from over.

As mentioned above in this section, location, size, and shape are the paramount consideration in surgical path planning. However, the most important feature of a tumour which mainly determines the path is the location of the tumour. Location is a determinative factor of the corresponding surgical path because it is always regarded as the target of the path by neurosurgeon. A reliable and safe path is a virtual line segment

jointing the target and the certain point on the surface of the brain, and is free from damaging blood vessels, nuclear, ventricles, functional areas and other important anatomic structures. In Fuji's study, they integrated the structure of blood vessels obtained from the MRA as a criterion to pick up the optimal path candidate [101]. The Circle of Willis should be avoided from interacting in the process of surgical path planning. To achieve this purpose, building an average distribution of brain vessels based on the existing data can overcome the difficulties caused by missing MRA data, benefitting doctors and patients, especially for the situation that an MRA scan remains inconceivable in a number of hospitals.

3 Methodology

3.1 Methods Outline

To find the optimal surgical path for image-guided neurosurgery, the existing CT or MR images as well as an existing surgical path are required. All these research samples are analyzed by diverse methods to discover the relationship among them. In this study, the clinical data are processed as follows (Figure 3.1):

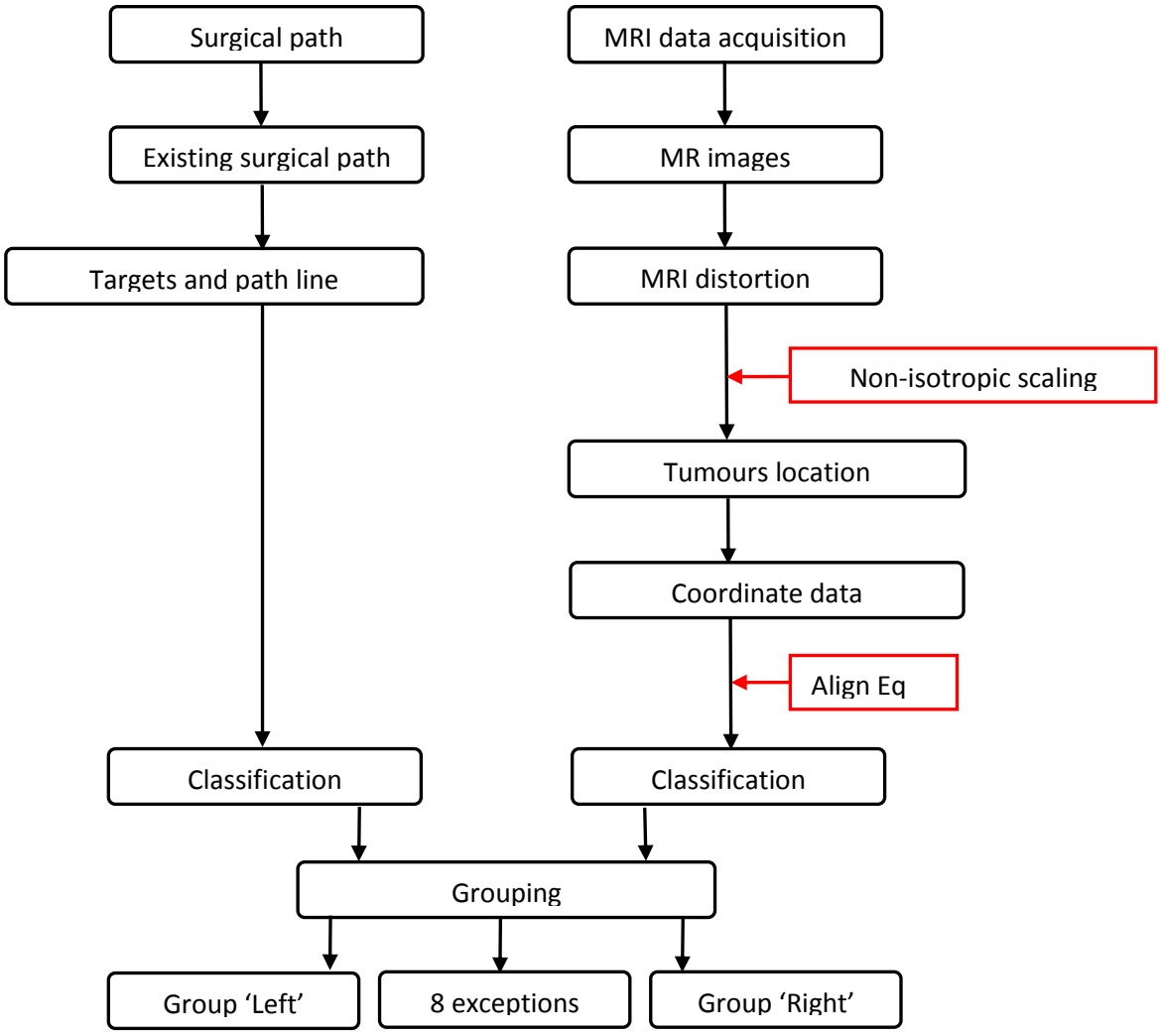

Figure 3.1 A flowchart of clinical data processing in this study

MRA data used to build the cerebral vascular template are processed as follows. The steps in establishing a template of a mean brain COW structure is schematically presented in a flowchart given in Figure 3.2, composing data collection, normalisation, vessel extraction, skeletonisation and re-construction, which are detailed in the following sections.

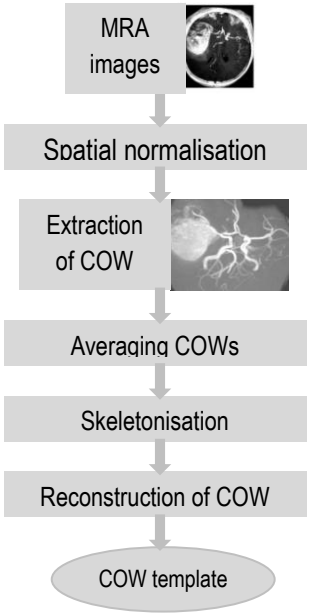

Figure 3.2 The flow chart of the establishment of a mean architecture of COW

3.2 Clinical data acquisition

3.2.1 MR data collection

All scans were acquired at the Medical Image Centre in the Navy General Hospital with a 1.5-T whole-body scanner (GE Signa horizon 1.5 T, GE Medical System) (Figure 3.3) [103]. MR images of one hundred consecutive patients of craniopharyngioma who

received a frame or frameless stereotactic operations in the Navy General Hospital from 2010 to 2013 were analyzed. All patients were prepared by contrast agent injections (Gadopentetic Acid Dimeglumine Salt Injection, Bayer Schering Pharma AG) before enhanced MR scans. An axial series of T1- weighted enhanced MR images (4-mm-thick slice, twenty-four to thirty-two slices for each patient) was collected from each patient's MR database. The image series can clearly show tumour range, the solid or cystic part, enhanced scanning range and the relationship to adjacent structures. All T1- weighted MR scans were acquired within the range of following imaging parameters: TR: 440~500 ms; TE11~14 ms; resolution: 240^2, 260^2 or 280^2.

All MRA data were acquired at the Medical Image Centre in the Navy General Hospital with a 3.0-T whole-body scanner (Philip3.0T, Philip Medical System) whithout contrast agent enhanced.

Figure 3.3 A photo of Signa horizon 1.5T, GE Medical System

3.2.2 Surgical path collection

The CAS-R-2 robot system used in this study was collaboratively developed by Beijing University of Aeronautics and Astronautics and the Navy General Hospital for

the project Application of Frameless Stereotactic Operations [104, 14]. The CAS-R-2 system mainly consists of two components: operation planning subsystem and a surgical localization and operation subsystem. The operation planning system provides surgeons with a simple, true-to-life and high-performance software tool, which generally fulfils the following functions: establishing and maintaining case history, entering and demonstrating data in the DICOM format, performing three-dimensional reconstruction for visualization, and planning the path of puncture. The surgical localization and operation subsystem is made up of a mechanical arm with five-degrees of freedom, fixed on the top of a stainless steel chassis which is 40 kg in weight and approximately 600 × 800 × 1,100 mm in volume (Figure 3.4 left). The mechanical arm is used as a probe holder through which the surgeon registers the fiducial marks and finally performs the stereotactic procedure. The system serves the purposes of tumour modelling, surgical path planning, simulating, and frameless stereotactic operation (Figure 3.4 right).

After four fiducial marks on a patient's forehead are registered by the probe, the position of patient's head in real space can be detected by the system. Meanwhile, an MRI series is reconstructed by the system into a virtual 3D space and four fiducial marks shown in the MR images are pointed out manually by the surgeon. Hence, the system links the MRI series with a real patient's head according to the fiducial marks. Therefore, a virtual surgical path shown on the operative interface will guide the puncture needle to the same position relative to the patient's head in reality. Depending on this interface, the surgeon has the ability to design a virtual surgical path which guides the robot arm. The snapshot pictures of the interface for each patient were collected for further study (Figure 3.5).

Figure 3.4 Left: Appearance of CAS-R-2 robot system; Right: Performing a frameless stereotactic operation with the CAS-R-2 robot system

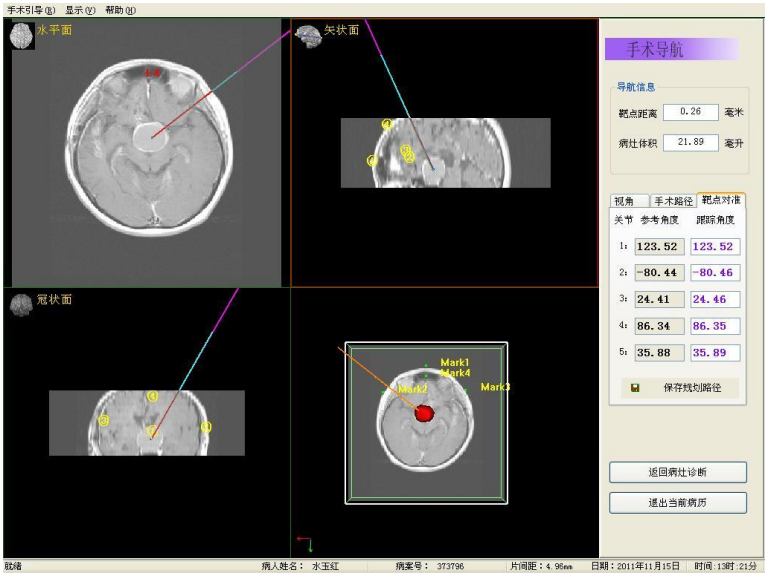

Figure 3.5 Snapshot picture of the operative interface for frameless stereotactic operation

MR images on 3 plane, reconstructed MR images, tumour model and virtual surgical path are shown on the left part; Features of the tumour, real and target position of robot arm are shown on the right part.

3.3 Detection of MR images distortion

Several cases of MRI data and one case of CT images data have been obtained, all of which display the same head frame. Images data is compared with various methods. Because CT images show clearer head structures and approximate to the real head frame without distortion [105], MR images are registered with reference to CT images in the steps as follows [106]:

1. The centre position of each mark was measured using the average location where the intensity level was above (or below in case of CT images) the threshold that was set empirically;

2. Calculation of the transformation factor including transformative error, translation factors and transformation matrix from a Matlab programme developed by ourselves;

3. The rotation, scaling and translation factors were computed using an existing SVD algorithm.

3.4 Tumours location analysis

MRI data were processed on a Lenovo T61 workstation using 3D slicer 4.0.1 software developed at the Brigham and Women's hospital, Harvard University [107, 108]. The 3D slicer provides multi modules that analyse the medical images at different levels. Modules *Editor*, *Model Maker* and *Models* were used for tumours modelling and locations measurement sequentially. Details of models such as volume, surface area and pixels are recorded to imply features of the tumour, and the coordinate data of each tumour's centre is measured with the 3D slicer manually [109]. The methods details are shown in the latter part. (Figure 5.1)

3.5 Targets and angles of existing surgical path lines analysis

To demonstrate the virtual surgical path in an operation planning platform, at least 2 groups of parameters should be investigated: target and orientation of surgical path. For this purpose, coordinate data of the path line target and 3 angles of the surgical path line were measured by the following methods:

1. In the snapshot picture of operative interface, the surgical target is clearly shown in an axial MRI slice. The 3D slicer is then employed to show exactly the same MRI slice and display the coordinates of the surgical target corresponding to the target's location in the snapshot picture. To improve the measurement accuracy, the target coordinates of each patient was measured 10 times and the average taken.

2. The orientation of surgical path is difficult to measure in reality. In addition, the CAS-R-2 robot system is unable to show the position of the probe in virtual 3D space. Therefore, the orientation of a surgical path only can be shown as a set of 3 angles with reference to 3 imaginary lines of a brain. They are as follow: 1) angle between the cerebral midline and projection line of the path on the axial plane; 2) angle made with the imaginary line passing through midpoint of two frontal poles to confluence sinus and projection line of the path on the sagittal plane; 3) angle between the cerebral midline and projection line of the path on the coronal plane. The former lines of these relative angles are defined as the datum line. The latter lines revolving clockwise around intersection points are recorded as positive degree angles, and vice versa. All of the angles of every patient were measured 10 times whereby the average was taken as the final measurement.

3.6 Coordinate data alignment

In practical clinical work, a patient is lying in a supine position on the patient bed in the scanner to receive an MR scan. The patient's head lies along the midline of the scanner cavity during the process of the scan, but the head position is not fixed. Because of the different head positions, brain image locates irregularly in an MRI slice. Obviously, the situation is unsuitable for scientific research. In this study, to investigate the location

of a tumour in a unified space, all coordinate data have been aligned with the following steps:

1. As a relatively fixed landmark in the brain, the vertex of the fourth ventricle was used as an original point to establish coordinate system [110, 111]. Although the adjacent structure shifts because of tumour compression, the vertex of the fourth ventricle is unlikely affected [112]. With 3D slicer software, the coordinates of the vertex of the fourth ventricle were measured 10 times for each MRI series and the average taken.

2. A new 3D coordinate system consists of these 4 geometric elements: original point (vertex of the fourth ventricle), Y axis (the parallel of the imaginary line between the midpoint of the frontal poles and confluence sinus, passing through the original point), X axis (the horizontal line passing through the original point) and Z axis (the perpendicular line of XY plane passing through the original point). The original 3D coordinate system of an MRI series is established in 3D slicer automatically with a default setting (Figure 3.6). Each angle between these two corresponding axes was measured respectively10 times and the average taken.

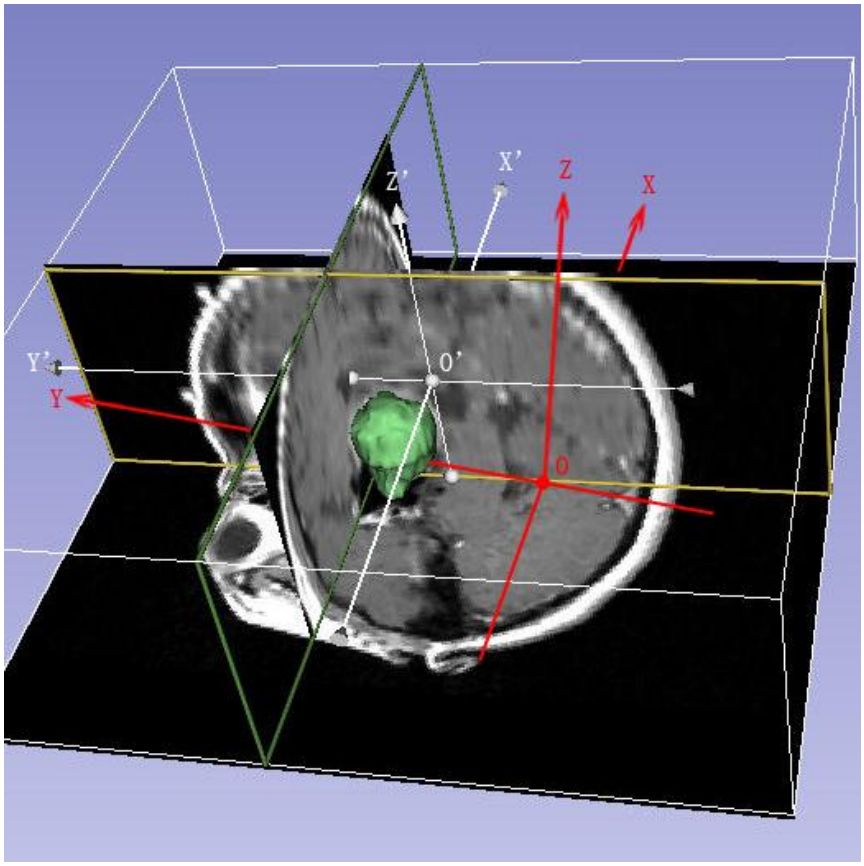

Figure 3.6 The sketch of the new 3D coordinate system
shown as red axes and the letter O indicates vertex of the fourth ventricle and the system generated by the 3D coordinate system in 3D Slicer (shown as white axes and letters).

3. All the measurement data was computed by Eq. (3.1).

$$
\begin{aligned}
X &= c \times \cos\left\{\left[a\cos\left(\frac{x}{c}\right)\right] + \alpha \times \left(\frac{\pi}{180}\right)\right\}; \\
Y &= c \times \sin\left\{\left[a\cos\left(\frac{x}{c}\right)\right] + \alpha \times \left(\frac{\pi}{180}\right)\right\}; \\
Z &= d \times \sin\left\{\left[a\cos\left(\frac{y}{d}\right)\right] + \beta \times \left(\frac{\pi}{180}\right)\right\}.
\end{aligned}
\tag{3.1}
$$

Where (x, y, z) refer to the coordinates of a random point in the 3D Slicer coordinate system. (X, Y, Z) indicate the corresponding point in the new 3D coordinate system. α denotes the angle of non-uniplanar X and X' axes; β denotes the angle of non-uniplanar Z and Z' axes; and $c = \sqrt{x^2 + y^2}$ and $d = \sqrt{y^2 + z^2}$.

3.7 Building a cerebrovascular template

3.7.1 Data collection

Twenty two sets of MRA data were collected from the Navy General Hospital in China, covering subjects of both healthy and diseased, which act as control data utilised to extract mean COW. A further six sets are also available at the disposal as working test sets. The volume of each dataset offers 16-bit resolution of 200×200 mm $\times 176$ frames as exemplified in Figure 3.7 (b). All these data comply with patients consent forms stipulated by the hospital.

3.7.2 Spatial normalisation

Although each image dataset shares the same dimension, the size of the brain varies due to differences both in size between individuals' brain and in variation in head positions while subjects undergoing MRA scanning. To minimise these changes, spatial normalisations are needed. The software of Statistical Parametric Mapping (SPM) [113] is applied in this regard with the selection of the T1 template, i.e., the longitudinal relaxation time, the same as the amassed datasets. In order to align with the original image resolution and take into account the limitation of existing computer processing power (to be addressed in Section 6), the normalization takes place at a voxel size of 0.8

$\times 0.8 \times 0.8$ mm^3, leading to the resulting normalised resolution of an image being $236 \times 196 \times 169$ mm^3.

3.7.3 Extraction of Circle of Willis (COW) artery

As introduced above, MRA images are designed for viewing brain arteries through the administration of a contrast agent into a subject before scanning. Usually, vessels can be viewed together with many non-vessel components of the brain as depicted in Figure 3.7(b & c). A certain level of enhancement has to be employed, for instance, threshold or maximum intensity projection (MIP), which requires substantial subjective intervention, leading to erroneous results. In order to simplify the level of segmenting controlling to a limited extent in a more objective and automatic way, the multi-scale vessel filter [114, 115] that is based on a Hessian matrix, is employed in this study. The strength of the approach lies in its application in highlighting tubular shape-like objects while overlooking the rest by assigning near zero values to them.

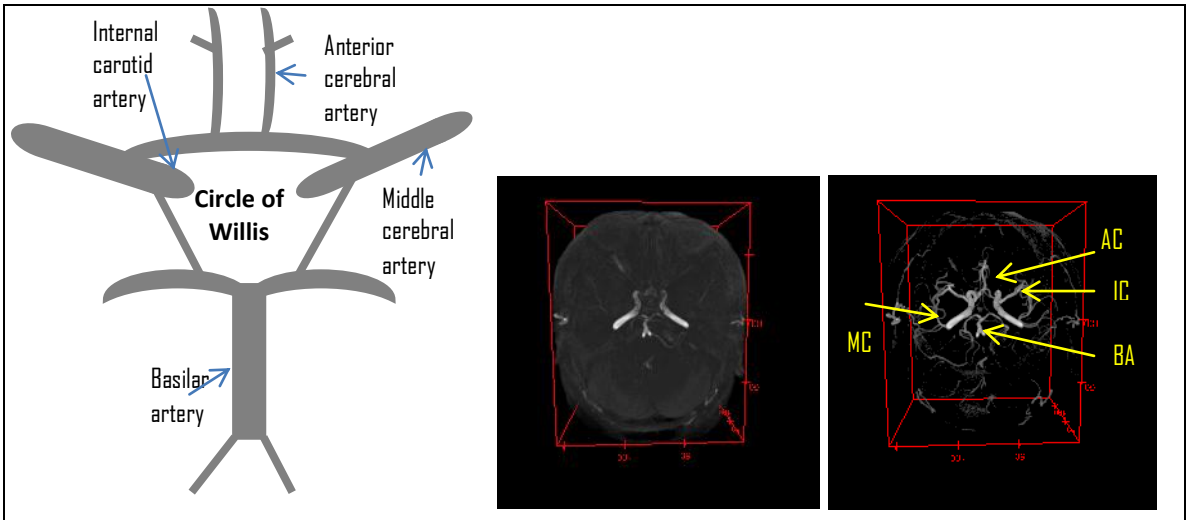

(a) COW artery. Bottom: beck; Top: eye.	(b) 3D MRA image. eye position. Bottom: neck.	(c) COW after a certain degree of thresholding of (b).

Figure 3.7 The Circle of Willis artery

The Circle of Willis artery illustrated in both drawing (a) and MRA images (b), and can be visible more clearly after a certain degree of thresholding (c).

Conceived by Ludwig Hesse, a Hessian matrix is a square matrix of second-order partial derivatives of a function, as expressed in Eq. (3.1) [116]. It describes the local curvature of a function of many variables.

$$H(f) = \begin{bmatrix} \frac{\partial^2 f}{\partial x_1^2} & \cdots & \frac{\partial^2 f}{\partial x_1 \, \partial x_n} \\ \vdots & \ddots & \vdots \\ \frac{\partial^2 f}{\partial x_n \, \partial x_1} & \cdots & \frac{\partial^2 f}{\partial x_n^2} \end{bmatrix} = H(x) \tag{3.1}$$

where $f(x_1, x_2, \ldots, x_n)$ is a real-valued function.

When it comes to the application to an image, I, a Hessian matrix can be applied after Taylor expansion. For instance, with a vessel diameter close to 4σ, I can be expressed at a local location δx in Eq. (3.2).

$$I(\boldsymbol{x}_o + \delta\boldsymbol{x}_o, \sigma) \approx I(\boldsymbol{x}_o, \sigma) + \delta\boldsymbol{x}_o{}^{\boldsymbol{T}}\nabla_{o,\sigma} + \delta\boldsymbol{x}_o{}^{T}H_{o,\sigma}\delta\boldsymbol{x}_o \quad (3.2)$$

where $\nabla_{o,\sigma}$ and $H_{o,\sigma}$ refer to gradient vectors and Hessian matrix respectively which are computed at $\boldsymbol{x}_o$ with a scale of σ.

As illustrated in Figure 3.8, the intensity profile of a vessel presents a Gaussian distribution form. This serves to confirm the consideration to enhance the edges of vessels by way of calculating differentiations using a convolution with the derivative of Gaussians as formulated in Eq. (3.3).

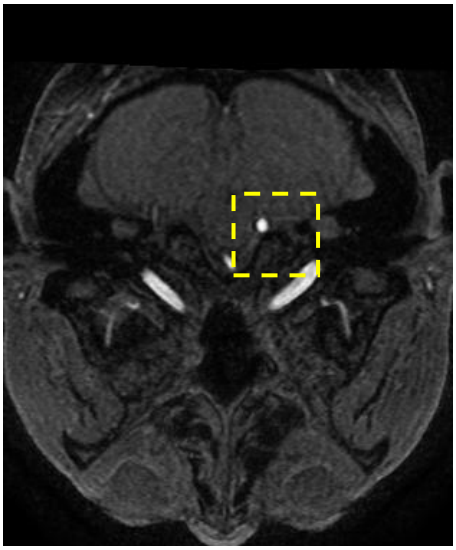

(a) A slice of an image set with a segment squared with dashed line containing two arteries with bright spots.

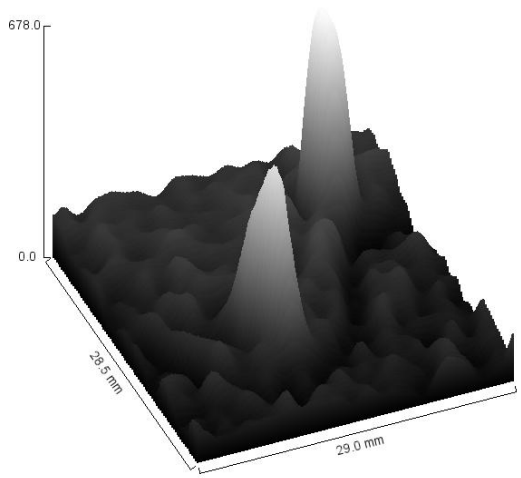

(b) Intensity profile of the segment in (a) showing two peak Gaussian-like shape corresponding to the two bright vessels in the segment.

Figure 3.8 An example displaying the Gaussian distribution of the intensity profile of arteries

$$\frac{\partial}{\partial \boldsymbol{x}} I(\boldsymbol{x}, \sigma) = \sigma I(\boldsymbol{x}) * \frac{\partial}{\partial \boldsymbol{x}} G(\boldsymbol{x}, \sigma) \tag{3.3}$$

where the 3-dimensional Gaussian is defined in Eq.(3.4):

$$G(\boldsymbol{x}, \sigma) = \frac{1}{\sqrt{2\pi\sigma^2}^3} e^{-\frac{||\boldsymbol{x}||^2}{2\sigma^2}} \tag{3.4}$$

On the other hand, the second-order derivative (Hessian) of a Gaussian kernel at a scale of σ generates a probe kernel that measures the contrast between the regions inside and outside the range of $(-\sigma, \sigma)$ in the direction of derivative as given in Eq. (3.5),

$$\delta \boldsymbol{x}_o{}^T H_{o,\sigma} \delta \boldsymbol{x}_o = \frac{\boldsymbol{\partial^2}}{\boldsymbol{\partial x_0^2}} I(x_0, \sigma) \tag{3.5}$$

Let λ_i(i=1, 2, 3) denote the eigenvalue corresponding to the i^{th} normalised eigenvector $\overline{\boldsymbol{u}}_{\sigma,i}$ of the Hessian matrix, $H_{o,\sigma}$, at the scale of σ, then

$$H_{o,\sigma} \overline{\boldsymbol{u}}_{\sigma,i} = \lambda_i \overline{\boldsymbol{u}}_{\sigma,i} \tag{3.6}$$

which leads to

$$\overline{\boldsymbol{u}}_{\sigma,i}^T H_{o,\sigma} \overline{\boldsymbol{u}}_{\sigma,i} = \lambda_i \tag{3.7}$$

Therefore, for an ideal tubular pattern in a 3D image, the following formulas exist:

$$|\lambda_1| \approx 0;\ |\lambda_1| \ll |\lambda_2|;\ \lambda_2 \approx \lambda_3 \tag{3.8}$$

The sign of λ_2 and λ_3 indicate their polarity, whereas the order of $|\lambda_1| \leq |\lambda_2| \leq |\lambda_3|$is arranged. Graphically, λ_1, λ_2, and λ_3 relate to the length of a cylindrical shape and the two diameters of the ellipse of its cross-section respectively. As a result, a vessel-like structure can be formulated in Eq. (3.9).

$$V(\sigma) = \begin{cases} \left(1 - \exp\left(-\frac{R_a}{2\alpha^2}\right)\right) \exp\left(-\frac{R_b}{2\beta^2}\right) (1 - \exp\left(-\frac{R_c}{2c^2}\right) \\ 0 \end{cases} \tag{3.9}$$

$if \lambda_2 > 0\ or \lambda_3 > 0$. In Eq. (3.9),

$$R_a = \frac{|\lambda_1|}{\sqrt{|\lambda_2 \lambda_3|}};\ R_b = \frac{|\lambda_2|}{|\lambda_3|};\ \text{and}\ R_c = \sqrt{\sum_1^3 \lambda_i^2}. \tag{3.10}$$

Moreover, the constants of α, β, and c serve to perform thresholding that controls the sensitivity of a line filter to the measures of R_a, R_b, and R_c that are referring to the volume, area, and length of a cylindrical shape respectively. Table 3.1 summaries the constants that are utilised in this investigation as inappropriate constants might result in images as well as vessels being out of visible range.

Table 3.1. Constants applied in the process of COW enhancement

α	β	c	σ	Image intensity Before Filtering	Image intensity level After Filtering
0.5	0.5	500	0.5 : 0.3 : 3.0	0 -- 1093	0 -- 0.1207

3.7.4 Calculation of mean COW using spherical Fisher-Rao metric

By definition, the Fisher–Rao metric tends to be a choice of Riemannian metric calculating the informational difference between measurements [117], which is defined on a space (P) of probability distribution of $p(x,\theta)$ and takes the form of Eq. (3.11).

$$ds = \sum\sum i_{rs} d\theta_r \, d\theta_s \tag{3.11}$$

where

$$i_{rs} = E\left[\left(\frac{\partial \log p(x,\theta)}{\partial \theta_r}\right)\left(\frac{\partial \log p(x,\theta)}{\partial \theta_s}\right)\right] \tag{3.12}$$

In Eq. (3.12), x refers to a specific value drawn from a collection of random variables, X, whereas $\int_X p(x,\theta)dx = 1$, and $\theta = (\theta_1, \ldots \theta_r, \ldots \theta_s, \ldots, \theta_n) \in R^n$, the Riemannian manifold. In Eq. (3.11), ds measures the change in $p(x,\theta)$when θ is replaced by $\theta + \delta\theta$.

If the probability distribution p is defined as a square-root density function as shown in Eq. (3.13):

$$\sqrt{p} = \psi \tag{3.13}$$

the Fisher-Rao metric can be calculated in Eq. (3.14) for any given two tangent vectors $v_1, v_2 \in T_\psi(\Psi)$ (i.e., distance space), which can be perceived as the unit sphere in a Hilbert space.

$$(v_1, v_2) = \int_0^1 v_1(\boldsymbol{s}) v_2(\boldsymbol{s}) d\boldsymbol{s} \tag{3.14}$$

where

$$\psi(\boldsymbol{s}) = \alpha e^{-D(\boldsymbol{s})} \tag{3.15}$$

and $\psi \in \Psi$ (the density space) and $\Psi = \left\{\psi: [0,1] \to R | \psi \geq 0, \int_0^1 \psi^2(\boldsymbol{s}) d\boldsymbol{s} = 1\right\}$. Furthermore, $D(\boldsymbol{s})$ refers to a distance transform and α the normalisation constant, with both of them to be addressed in more detail below.

The advantage of selecting Ψ for analysis is that it constitutes a convex subset of a unit sphere in L^2norm with many of the geometric expressions being already well defined [90, 94]. In this investigation, the calculation of the mean COW is therefore assimilated in the following steps by way of explanation, which has been clearly described in [94].

- Converting the enhanced image obtained in Section 3.7.3 into a binary image, BW.

- Calculating the Geodesic distance using Eq. (3.16) to create a tangent space$T_{\psi}(\Psi)$. Define $\psi_1, \psi_2 \in \Psi$ for any two vectors,

$$d(\psi_1, \psi_2) = \cos^{-1}\langle \psi_1, \psi_2 \rangle \tag{3.16}$$

and α in Eq. (3.14) for each distance image $D(\boldsymbol{s})$ (=$d(\psi_1, \psi_2)$) is derived in Eq. (3.17).

$$\alpha^2 = \frac{1}{\int e^{-2D(s)} d\boldsymbol{s}} \tag{3.17}$$

The constant, α, serves as a threshold to allow the recovery of the distance transform function from the square-root density representation by computing the inverse map when using Eq. (3.14).

- Parameterizing the distance in terms of a direction v in $T_{\psi}(\Psi)$ using an exponential map to square-root density Ψ:

$$exp_{\psi_1}(v) = \cos(|v|)\psi_1 + \sin(|v|)\frac{v}{|v|} \tag{3.18}$$

- Calculating Karcher mean in the space of density Ψ:

$$\bar{\psi} = arg\min_{\psi \in \Psi} \sum_{i=1}^{n} d^2(\psi, \psi_i) \tag{3.19}$$

- Computing the inverse exponential map converting back to distance space:

  for any $\psi_1, \psi_2 \in \Psi$, $v \in T_{\psi}(\Psi)$ to be the inverse exponential of ψ_2 if $exp_{\psi_1}(v) = \psi_2$, v can be obtained as below:

$$u = \psi_2 - \langle \psi_2, \psi_1 \rangle \psi_1 \tag{3.20}$$

$$v = u \cos^{-1} \psi_1, \psi_2 / \sqrt{(u, u)} \tag{3.21}$$

A search of Karcher means $\bar{\psi}$ then takes the approach of gradient where an estimate is iteratively updated according to Eq. (3.22).

$$\mu \rightarrow exp_{\epsilon}(\epsilon v),\ v = \frac{1}{n}\sum_{i=1}^{n} exp_{\mu}^{-1}(\psi_i) \tag{3.22}$$

where exp and $\exp^{-1}$ are expressed in Eqs.(3.18) and (3.21) respectively. The scalar of $0 < \epsilon < 0.5$ is a step size for iteration.

- Converting back to image space

$$BW = -\log \bar{D}$$

Figure 3.9 graphically demonstrates the above procedures by obtaining a mean shape from two images in 2D form. As it shows clearly on the last graph in row 3 and column 3 with red solid line, when shape data are converted into exponential map, they display Gaussian-like patterns from which it is easier to calculate the Karcher mean by working out the corresponding points along each coordinate in the x-axis. Then this exponential mean is converted back into distance space representation that is in turn transformed into binary image, the average of all the images. Each step can be either visualized in the form of an image or a plot, which is demonstrated in both ways. In the figure, it is displayed in image form for Image 1 and in data plot form for Image 2.

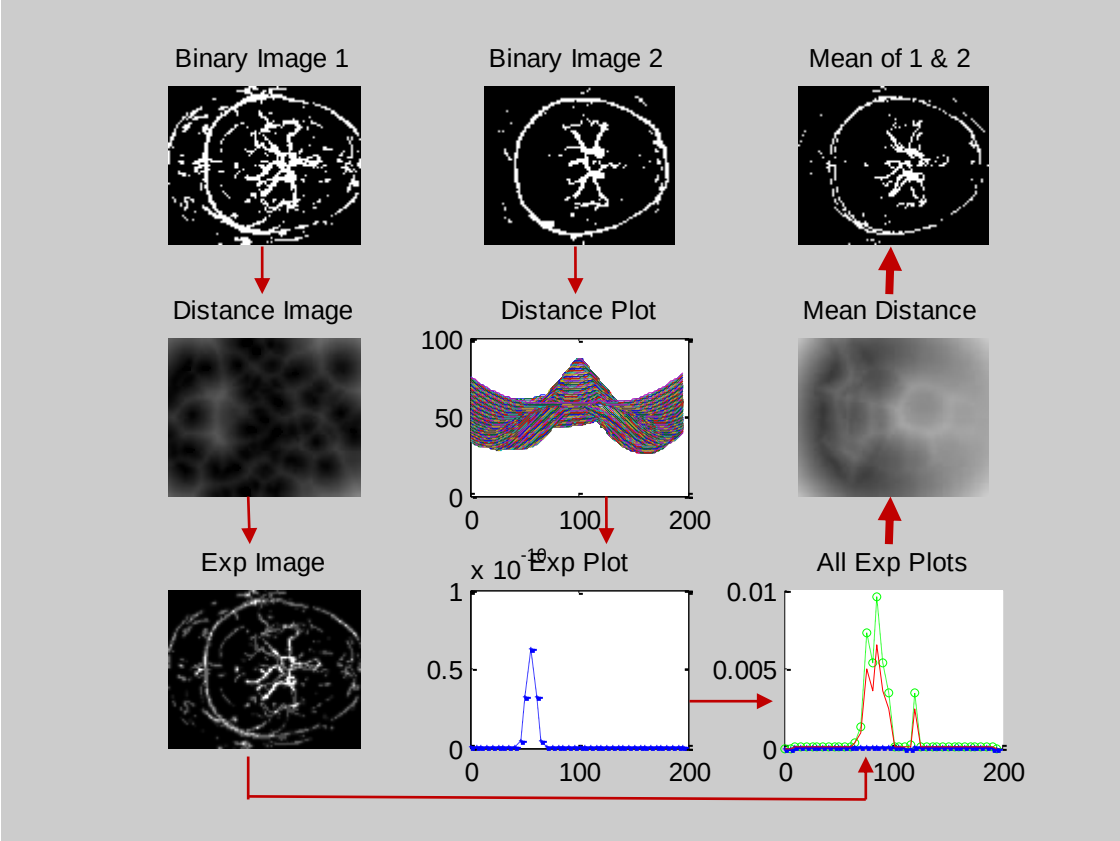

Figure 3.9 The procedure of calculating the mean of images 1 and 2

Row 1: binary images; Row 2: distance space displayed in the form of either image (image 1) or plot (image 2); Row 3: Square root density space presented in the form of either image (bottom left) or plot (bottom middle and bottom right).

3.7.5 Skeletonization of the mean COW

As illustrated in Figure 3.9, the resultant mean shape remains in black and white binary form which only reserves the mean location of every vessel of the COW. The

exact diameters of each vessel cannot be factored in this way, which leads to the next step of skeletonization of the mean COW to obtain the middle line of each vessel. In this study, after being cropped from the outliers of the BW brain image, i.e., skull, the skeletonisation of COW follows, by the application of the 3D Skeleton plugin tool [118] for the free software ImageJ [119].

3.7.6 Re-construction of mean COW

After skeletonisation, the mean COW has to be recovered into its rightful diameters. According to the mean value of each vessel, restoration of its mean width is conducted by building on the skeleton that acts as the middle line of each vessel. As demonstrated in Figure 3.10, a cross-section of each vessel is reconstructed using a surface function calculated in Eq. (3.23).

$$dx \cdot x + dy \cdot y + dz \cdot z = c \tag{3.23}$$

where $[dx, dy, dz] = gradient(I)$ and I represents the skeleton image. The function $gradient$ gives the numerical gradient of the matrix I.

On each cross section perpendicular to the vessel middle line, the area of the cross section can be filled in when the angle rotates from zero to 360^o with radius extending from zero to $d/2$, i.e., half of the average diameter of each type of vessels, which is formulated in Eq. (24) and illustrated in Figure 3.10.

$$\begin{cases} x = r\cos \propto + x_0 \\ y = y\sin \propto + y_0 \\ z = (c - dx \cdot x - dy \cdot y)/dz \end{cases} \tag{3.24}$$

Where $r \in \left[0, \frac{d}{2}\right], \propto \in [0, 360^0], and dz \neq 0.$

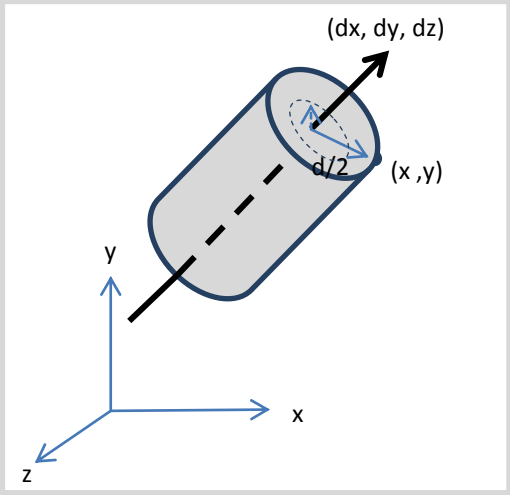

Figure 3.10 Schematic illustration of reconstruction of a vessel cross-section with diameter of d

3.7.7 Designing a surgical path by finding the minimal distance

At present, the surgical path takes a straight line, which therefore can be realised using the approach of minimum distance that is calculated from the target centre to the

skull by taking into consideration avoiding arteries of the COW. A number of known key functional regions, e.g., primary visual cortex at Brodman area 17, can also be kept away when incorporating with a brain anatomy template that has been well established already.

4 Detection of MR images distortion

It has been described in the literature that image guidance of surgical interventions is one of the most complex applications of computer technology to practical neurosurgery. Lots of novel methods or technologies have been reported in recent years. In addition, as the technology of medical imaging has advanced, medical images are being employed in various clinical aspects such as diagnosis, therapy and evaluation. Nevertheless, the accuracy and precision of these images are basic prerequisites that should be ensured in those clinical aspects, which include image guidance. Therefore, correcting the distortion of medical images depending on available image data is as important as developing a novel path planning module.

4.1 Methods

The method outline of detection of MR images distortion is described in the methodology part. Because CT images show clearer head structures and approximate to the real head frame without distortion, we used it as standard tool to detect the MR distortion. 10 sets of MRI with Gamma knife head frame were collected from Navy General Hospital, and 5 of 10 sets of MRI were picked out randomly for control group, whereas the rest 5 sets of MRI were processed as test group. Figure 4.1 illustrates the Gamma head frame worn by subjects when undergoing both MR and CT image scanning, whilst Figure 4.2 depicts the CT and MR images with fiducial markers showing the same subject.

4.1.1 Linear transformation with non-isotropic scale factors

Preliminary results showed the MR images in the test group varying less in rotation than in scale with less than 1-degree variations along each of three axial directions. Meanwhile, scaling factors in 3 directions showed different patterns. The scaling transformation in y direction was 0.5960, whereas the value in x and y direction approximated to 1. Regarding this non-isotropic pattern, the scaling factors were

reanalyzed as follows.

Let two sets of 3D coordinate data be represented by Yi=[y_{1i} y_{2i} y_{3i}]T and Xi=[x_{1i} x_{2i} x_{3i}]T, (i=1, 2, …, n) that are obtained from fiducial marks in both CT and MR images respectively along three axial directions, then the relationship between data Yi and Xi can be expressed using 3×3 matrixes M and translation matrix T using Eq. (4.1).

$$\mathbf{Y_i} = \mathrm{M}\,\mathbf{X_i} + \mathrm{T} + \mathbf{e_i} \tag{4.1}$$

Where $\mathbf{e_i} = [e_{1i}\ e_{2i}\ e_{3i}]^T$ is the error vector induced in the formula and *i* is the number of fiducial marker pairs in both modalities , and

$$\mathrm{M}=\begin{bmatrix} m_{11} & m_{12} & m_{13} \\ m_{21} & m_{22} & m_{23} \\ m_{31} & m_{32} & m_{33} \end{bmatrix} \qquad \mathrm{T}=\begin{bmatrix} t_1 \\ t_2 \\ t_3 \end{bmatrix}$$

Therefore m_{ij} can be solved linearly by Eq. (4.2) (assuming the determinant of the 3 x 3 matrix in Eq. (4.2) is not equal to zero).

$$\begin{bmatrix} m_{i1} \\ m_{i2} \\ m_{i3} \end{bmatrix} = \begin{bmatrix} \sum x_1'^2 & \sum x_1' x_2' & \sum x_1' x_3' \\ \sum x_1' x_2' & \sum x_2'^2 & \sum x_2' x_3' \\ \sum x_1' x_3' & \sum x_2' x_3' & \sum x_3'^2 \end{bmatrix}^{-1} \begin{bmatrix} \sum x_1' y_i' \\ \sum x_2' y_i' \\ \sum x_3' y_i' \end{bmatrix} \tag{4.2}$$

Where i = 1, 2, 3. and

$$Y_i' = Y_i - \overline{Y_i} = \begin{bmatrix} y_{1i} - \frac{\sum y_{1i}}{n} \\ y_{2i} - \frac{\sum y_{2i}}{n} \\ y_{3i} - \frac{\sum y_{3i}}{n} \end{bmatrix} \qquad X_i' = X_i - \overline{X_i} = \begin{bmatrix} x_{1i} - \frac{\sum x_{1i}}{n} \\ x_{2i} - \frac{\sum x_{2i}}{n} \\ x_{3i} - \frac{\sum x_{3i}}{n} \end{bmatrix}$$

After M has been figured out using MRI data in the test group, M is employed to calculate the average distance between corresponding marks in each MR image and CT

image respectively (average error), and the biggest distance of these corresponding marks (biggest distance) in the control group. In Ep. (4.1), X_i are replaced by original coordinate data of MRI in the control group, thus Y_i indicates the corrected coordinate data of corresponding fiducial marks in MRI. Therefore, Average error and biggest distance, indicating average distance and biggest distance between corresponding marks in corrected MR image and CT image respectively, are easy to be computed. All the results are shown in the Table 4.1.

4.1.2 Linear transformation with a constant scale factor

Singular value decomposition (SVD) has been applied in this application in order to compare with the non-isotropic scale factor method. Eq. (4.1) becomes Eq. (4.3).

$$Y_i = s\,R\,X_i + T + \mathbf{e_i} \tag{4.3}$$

Therefore R, the rotation matrix can be decomposed as

$$R = VDU^T \tag{4.4}$$

where $D = \begin{cases} I & if\, det(U)\det(V) = 1 \\ diag(1,1,-1) & if\, det(U)\det(V) = -1 \end{cases}$

Similar to above, S and R have been figured out to calculate the average distance between corresponding marks in each MR image and CT image respectively (average error), and the biggest distance of these corresponding marks (biggest distance) in the control group. All the results are shown in the Table 4.1.

4.2 Results

Some initial results have been obtained which are described below. The final results from these two methods will be compared using statistics software, and a method which is able to decrease distortion to the maximum extent will be employed to analyse all the MR and CT images data [120].

The initial results for correction of distortion have been carried out on five sets of MR and CT images data. Each set of data are acquired with a head frame as shown in Figure 4.1. Slices of CT and MR images in the same position are shown in Figure 4.2 [121].

After registration of the markers from MR and CT images of each subject using the method described above, the transformative errors were calculated. The transformative errors are shown in Table 4.1. The initial results indicate that this algorithm can be better than the existing SVD algorithms, because the average distance and the biggest distance are more approaching to the reality. However, general conclusions cannot be drawn until it is confirmed by further tests.

Figure 4.1 A head frame with contrast agent filled in the N shape tubes

The N shape tubes can be displayed both in MR and CT images.

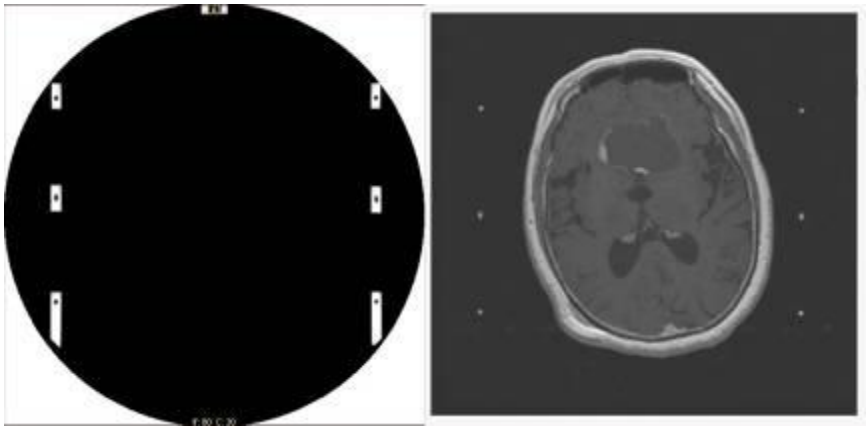

Figure 4.2 CT and MR slices at the same head position (same z direction)

Table 4.1 The largest transformative errors worked out from two algorithms

	Non-isotropic scaling algorithm			**SVD**		
Subject	**Average error (mm)**	**Standard Deviation**	**Biggest distance (mm)**	**Average error (mm)**	**Standard Deviation**	**Biggest distance (mm)**
1	0.0537	0.3622	1.2507	0.3004	3.3037	3.8256
2	0.1242	9.5389	9.6803	0.2782	13.5187	11.6049
3	0.1130	1.3413	2.3578	0.1420	1.7342	2.8391
4	0.0641	0.5388	1.6649	0.2448	3.1562	3.7903
5	0.0533	0.3131	1.3277	0.1648	1.4449	2.2514
Mean	**0.08166**	**2.41886**	**3.25628**	**0.22604**	**4.63154**	**4.86226**

4.3 Summary

The linear transformation approach is suitable in finding non-isotropic scaling factors, constituting one of the approaches in registration of fiducial markers. Comparison with other approaches, such as chi-square, will form part of future work and is currently being investigated.

According to these two methods, the overall errors are less than 0.1mm, suggesting that for clinical applications, these MR images are reliable and can be used directly [122, 123].

5 Images data analysis and classification

5.1 Tumours location analysis

As described in the methodology part, MRI data were processed on a Lenovo T61 workstation using 3D slicer 4.0.1 software developed at the Brigham and Women's hospital, Harvard University [107, 108]. Modules *Editor*, *Model Maker* and *Models* were employed for tumours modelling sequentially [124]. In the module Editor, Level tracing is a useful tool to segment the tumour from each slice automatically according to their intensity difference between tumour content and brain tissues. The module *Model Maker* generates a 3D tumour model for each MR series permitting display in axial, sagittal and coronal plane. As a multi-functional module, *Models* provides functions including information presentation, changeable tumour model's properties as well as scalars [125]. After a 3D tumour model is built, details of the model such as volume, surface area and pixels are recorded as a tumour's characters. In addition, the coordinate data of each tumour's centre is measured with 3D Slicer manually [109] (Figure 5.1).

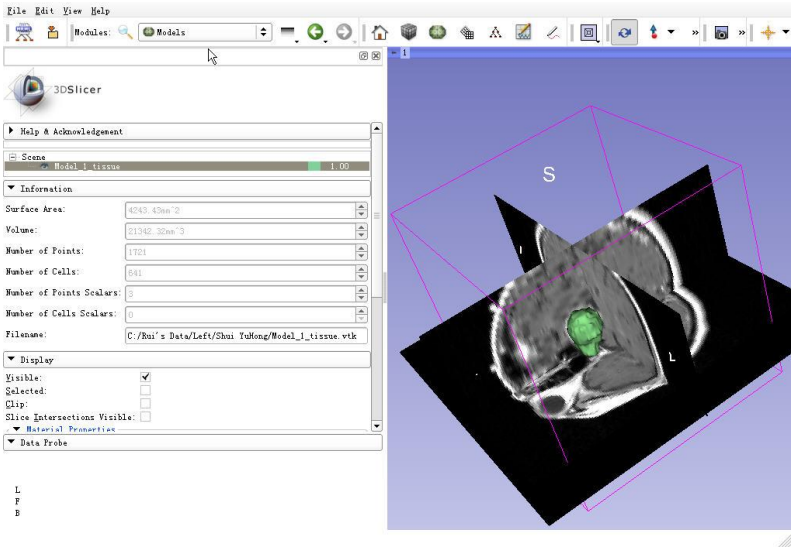

Figure 5.1 The interface of 3D Slicer (Module Models)

Features of the tumour are shown on the left part. MR images on 3 planes and tumour model are shown on the right part.

5.2 Targets and angles of existing surgical path lines analysis

As mentioned above, coordinate data of the path line target and 3 angles of surgical path line were measured manually:

1. Corresponding to the snapshot picture of operative interface, the same MRI slice is shown on the 3D slicer platform. The coordinates of the surgical target are precisely generated by 3D slicer, depending on the relative location of the surgical target in the snapshot picture. The target coordinates of each patient was measured 10 times and the average taken.

2. Three angles with reference to 3 imaginary lines of a brain: 1) angle between the cerebral midline and projection line of the path on the axial plane; 2) angle made with the imaginary line passing through midpoint of two frontal poles to confluence sinus and projection line of the path on the sagittal plane; 3) angle between the cerebral midline and projection line of the path on the coronal plane are employed to depicted the orientation of the surgical path. The former lines of these relative angles are defined as the datum line. The latter lines revolving clockwise around intersection points are positive degree angles, and vice versa. All of the angles of every patient were measured 10 times and the average was taken as the final measurement.

5.3 Coordinate data alignment

To align all the coordinates data and angles data into the same standards, the data is processed in the following steps:

1. The vertex of the fourth ventricle was considered as an original point to establish a coordinate system. With 3D slicer software, the coordinates of the vertex of the fourth ventricle were measured 10 times for each MRI series and the average taken.

2. The original point (vertex of the fourth ventricle), Y axis (the parallel of the imaginary line between midpoint of frontal poles and confluence sinus, passing through the original point), X axis (the horizontal line passing through the original point) and Z axis (the perpendicular line of XY plane passing through the original point) establish a new 3D coordinate system, which was regarded as the standard coordinate system. The original 3D coordinate system of the MRI series is established in 3D slicer automatically with a default setting (Figure 3.6). Each angle between these two corresponding axes was measured respectively by the same method as described above.

3. All the measurement data was computed by Eq. (5.1).

$$\begin{aligned} X &= c \times \cos\left\{\left[a\cos\left(\frac{x}{c}\right)\right] + \alpha \times \left(\frac{\pi}{180}\right)\right\}; \\ Y &= c \times \sin\left\{\left[a\cos\left(\frac{x}{c}\right)\right] + \alpha \times \left(\frac{\pi}{180}\right)\right\}; \\ Z &= d \times \sin\left\{\left[a\cos\left(\frac{y}{d}\right)\right] + \beta \times \left(\frac{\pi}{180}\right)\right\}. \end{aligned} \tag{5.1}$$

Where (x, y, z) refer to the coordinates of a random point in the 3D Slicer coordinate system. (X, Y, Z) indicate the corresponding point in the new 3D coordinate system. α denotes the angle of non-uniplanar X and X' axes; β denotes the angle of non-uniplanar Z and Z' axes; and $c = \sqrt{x^2 + y^2}$ and $d = \sqrt{y^2 + z^2}$.

The aligned coordinate data will be employed to classified, which in turn to establish expert system. In practical neurosurgical operation, six of the parameters must be achieved before the operation, which are target coordinate data, namely x, y, z data in the orthogonal coordinate system, two angels of the surgical path in spherical polar system and depth of the insertion. All of these parameters were obtained from the aligned coordinate data, including target and insert angles, except the depth of the insertion. The data of 100 cases are shown in Appendix 1.

5.4 Data Classification

As described above, neurosurgeons plan optimal surgical path for individual patients depending on their experience. The factors considered by neurosurgeons to design a path are listed successively as follows (in an order based on importance): location, size, shape and the structure of the tumour. Based on the existing data, the tumours (craniopharyngiomas) located in a specific region of the brain, sellar region, where the tumours grow with regard to tumorigenicity. In terms of location, it seems likely that the centre of a tumour can be reasonably representative where the is tumour located. To find out the relationship between the tumours' location and the surgical path, the coordinates of tumours' centres and inserting angles of surgical path are therefore measured respectively.

Preliminarily, the classification of the path pattern is carried out within two categories, which are on the left and on the right hand side of the brain with reference to the median sagittal plane (Figure 5.2). The line angles of one hundred surgical paths at XY plane are demonstrated in Figure 5.4. The axial line where x=0 represents the sagittal midline projected onto the XY plane. Similarly, all the MR data are divided into 2 groups based on the coordinate data of tumour centres. The centre positions of these one hundred cases in the XY plane are shown in Figure 5.3. According to Figure 5.4, the surgical path lines have a concentrated distribution to a certain extent. Meanwhile, the centre positions of tumours located in the left side, shown in Figure 5.3, roughly coincide with the left category of the clustered data shown in Figure 5.4. Likewise, surgical lines in the right category almost match all the centre positions of tumours on the same side. With only 8 exceptions, the locations of the centre points on the left of the midline in Figure 5.4 correspond to the right group positioned in Figure 5.3.

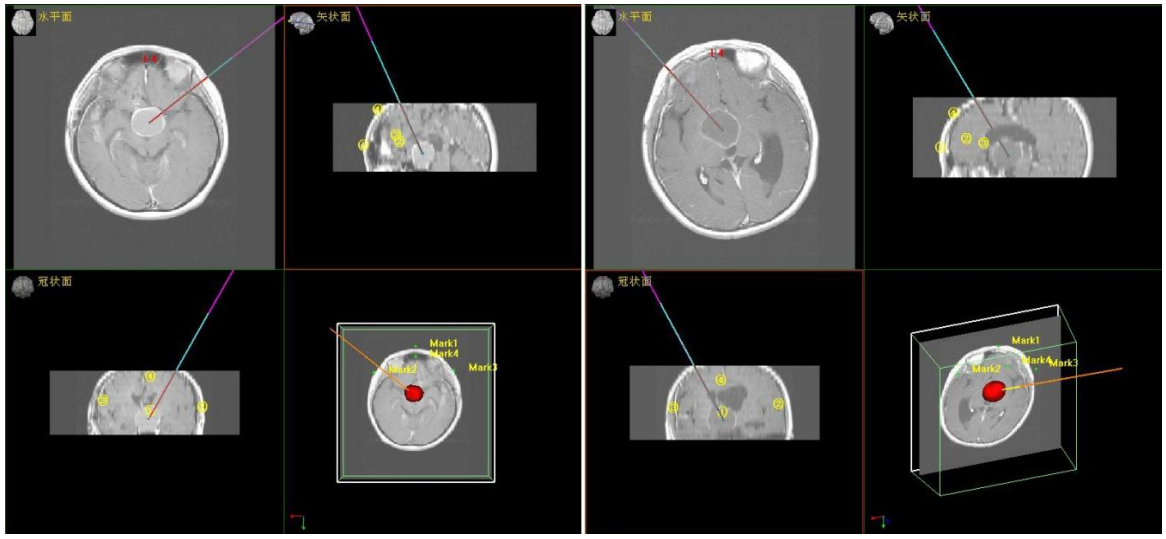

Surgical path on the lift side	Surgical path on the right side

Figure 5.2 Two examples of surgical paths that are indicated by red lines in the frameless stereotactic operative interface

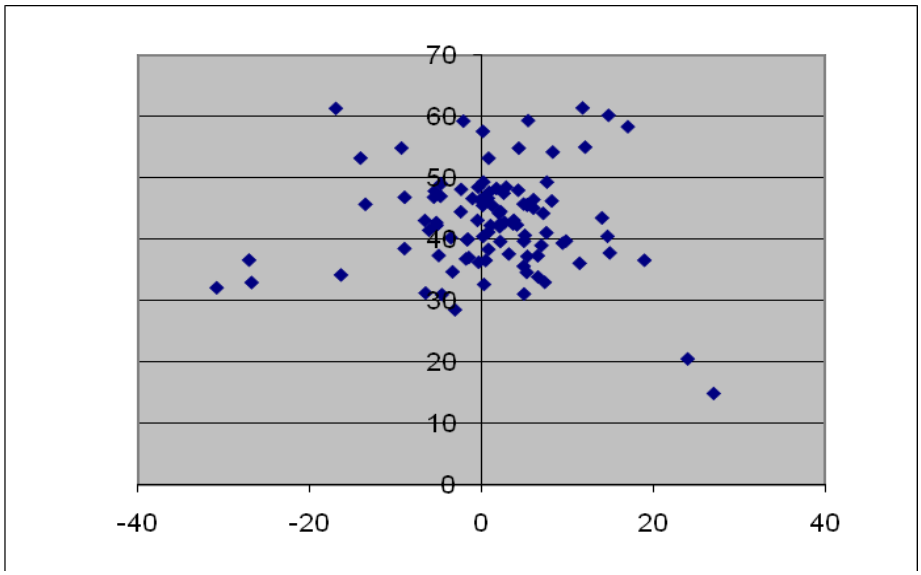

Figure 5.3 The locations of tumour centres of 100 in the XY plane

in which the line x=0 represents the median sagittal plane.

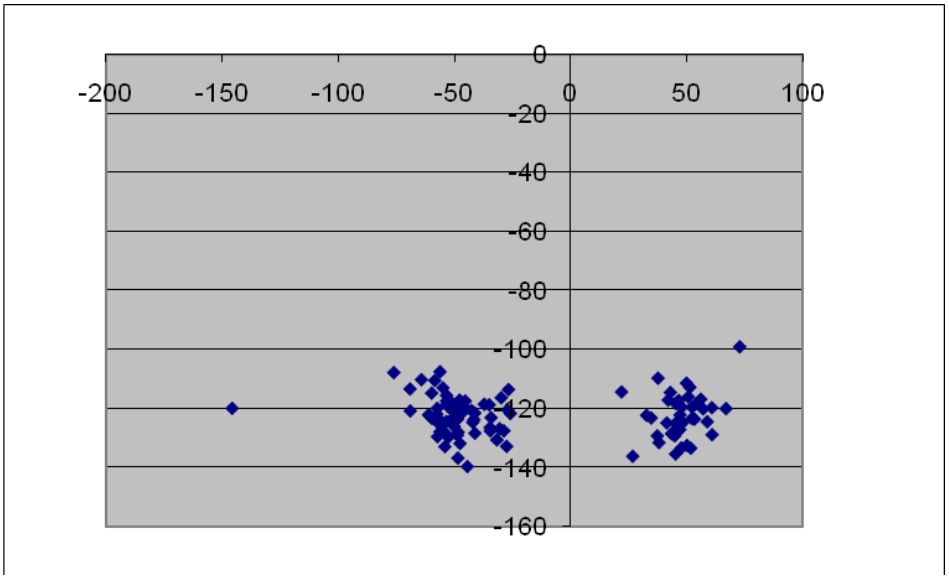

Figure 5.4 The angles of the 100 path lines projected onto XY and YZ planes

The line x=0 indicates the median sagittal plane.

5.5 Summary

According to the result shown in the Figure 5.3 and Figure 5.4, the centres of the tumours scattered around the middle line while the surgical path lines have a concentrated distribution in two regions, indicating a corresponding relationship between these two distributing patterns. It can be concluded that the tumours with proximal positions will result in a similar surgical path.

6 Results of building cerebral vascular template

6.1 Experimental results

Implementation took place on a Dell Precision T5500 workstation with 12-Gbyte memory, together with Intel® Xeon® CPU with duel 2.4 and 2.39 GHz processors. Under the Windows 64-bit operating system, Matlab R2013a software is employed for image processing.

Since the final mean shape is represented using a binary matrix whereby 1 refers to a vessel position and 0 non-vessels, the image of 8-bit is stored. Table 6.1 follows the changes in image volume sizes during each stage of the averaging process.

Table 6.1 Image sizes during each processing stage

Original image	**Spatial normalised using SPM (V=0.8×0.8×0.8mm)**	**Hessian Filter**	**MAT file**	**Mean Shape**	**Skeleton**	**Reconstructed COW**
200 × 200 mm× 174 frames	196×236×169	196×236×169	196×236×169 ×23 dataset	196×236×169	196×236×169	196×236×169
16-bit, 90 MB	16-bit, 16 MB	16-bit, 16 MB	8-bit, 8 MB	16-bit, 16 MB	8-bit, 8MB	8-bit, 8MB

Figure 6.1 depicts the length of diameters for each of the COW measured from the twenty-two datasets investigated, including the Internal Carotid Artery (ICA), the Middle Cerebral Artery (MCA), the Basilar Artery (BA), and the Anterior Cerebral Artery (ACA), as figuratively labelled at Figure 2(c). For each diameter (in millimetres) of

vessels on each COW, the measurement takes the average reading of three attempts on the same vessel to ensure the consistency of measurement. In the figure, 'Left' refers to the vessels on the left hand side of the body. Likewise, 'Right' indicates on the right. There are two (bilateral) of ICA, MCA and ACA arteries for each COW, and one BA artery. Understandably, on an MRA image, patient's left side is shown on the right part of the image to be made to face the users, and vice versa. All original measurement data is shown as Appendix 2.

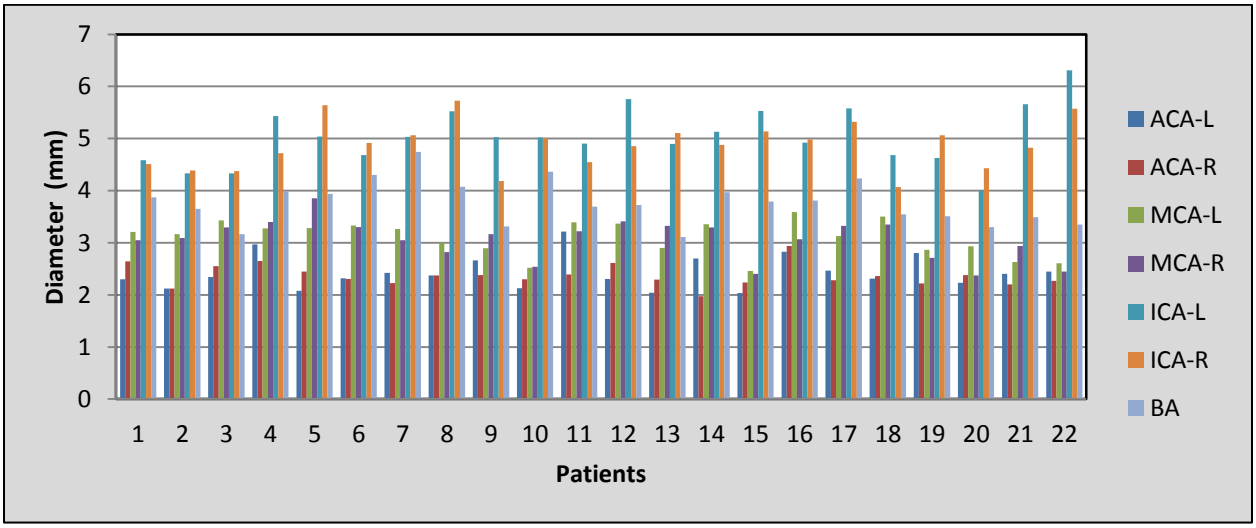

Figure 6.1 The measurement of arteries in COW for the twenty-two datasets (x-axis) investigated in this study

'L' refers to the left vessel and 'R' the right one. The measurement in the y-axis is in the unit of mm.

The mean diameter values measured from the twenty-two datasets are presented in Table 6.2.

Table 6.2 The mean diameters measured from the twenty-two datasets.

	ACA-L	**ACA-R**	**MCA-L**	**MCA-R**	**ICA L**	**ICA R**	**BA**	**Mean**
Mean diameter for each type of arteries	2.40	2.37	3.10	3.06	5.04	4.87	3.34	
Mean of both left and right vessels	**2.39**		**3.08**		**4.96**		**3.34**	
Standard deviation (SD)	0.31	0.21	0.33	0.38	0.45	0.50	0.54	**0.39**

In Table 6.2, it appears that for the same bilateral arteries, the left ones display slightly larger than the right counterparts, e.g., the averaged diameter of left ICA is 5.04 mm in comparison with 4.87mm on the right. However, this tendency does not show in a significant way with variations ranging from 1.3% to 3.4% across all the vessels in the COW.

Figuratively, Figure 6.2 illustrates the results of the extraction of COWs from twenty-two datasets by using a Hessian matrix. The graph on row 4 column 5 shows the extraction of COW from the mean of sum images of all the twenty-two images, i.e, $meansumimage = \frac{\sum I}{22}$, whereas the last image at bottom-right is the average shape calculated using the procedures addressed in Section 3.7.4.

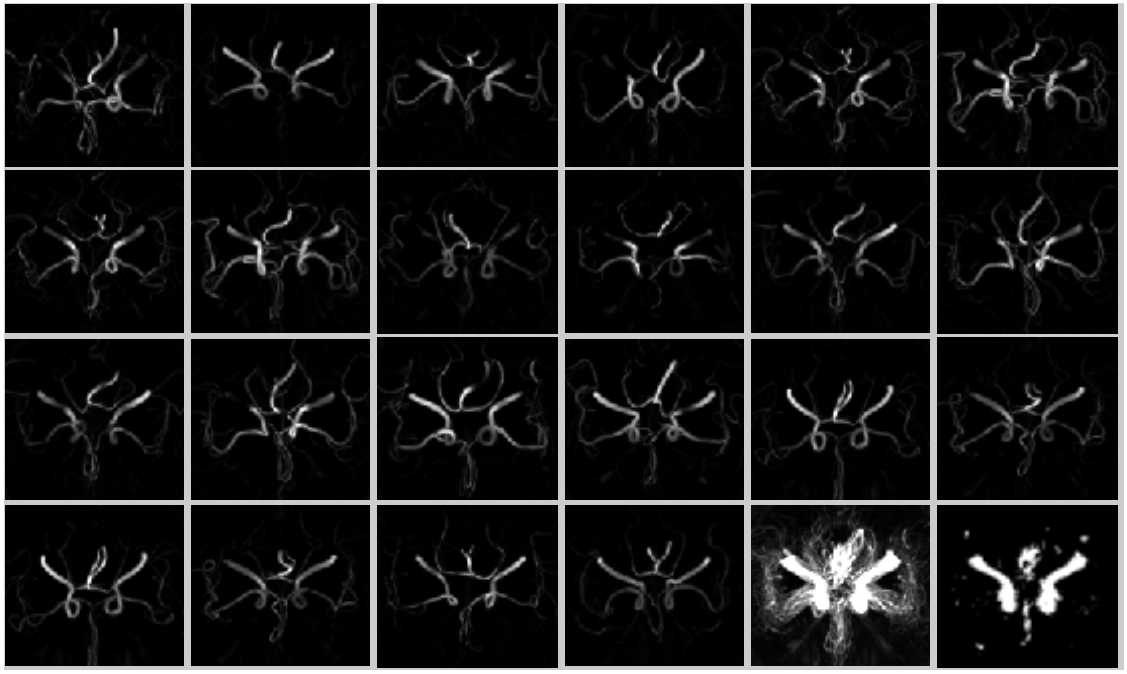

Figure 6.2. The extraction of COW from 22 datasets using a Hessian matrix

Row 4 column 5 shows the mean sum image and the bottom right the mean COW generated using the approach given in Section 3.7.4.

In addition, the comparative view in 3D form of the COWs obtained from both mean sum images and Karcher mean is demonstrated in Figure 6.3. Logically, the mean sum image tends to embrace all the COWs together and appears to contain most of the vessels. By contrast, the mean shape can be representative.

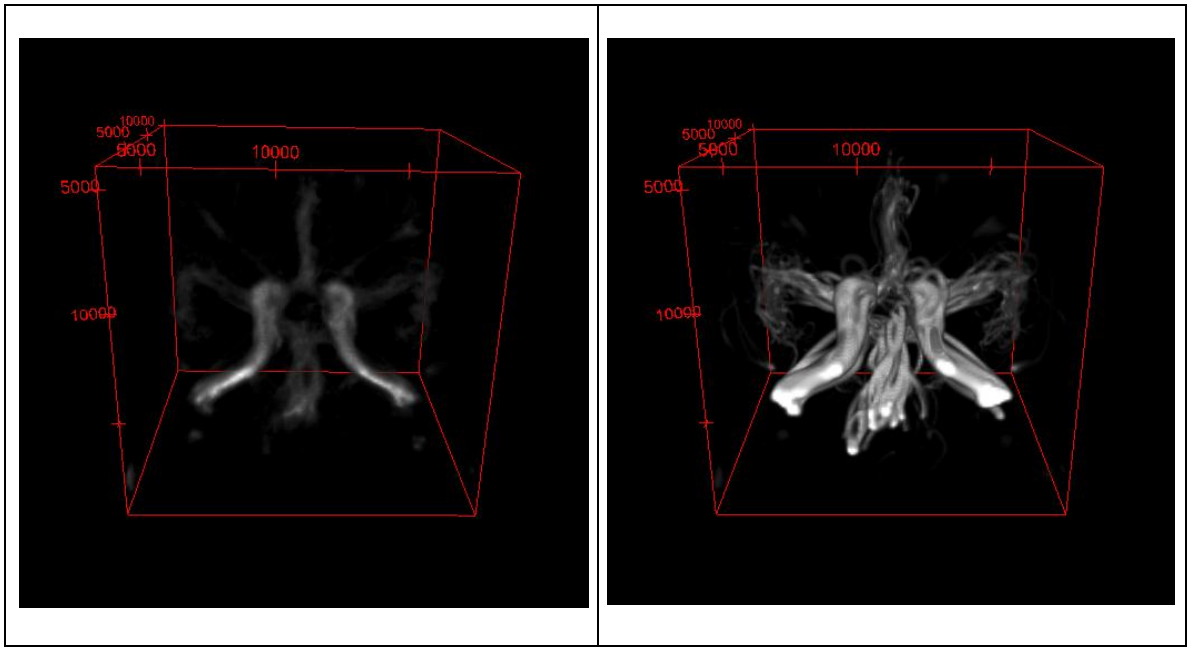

(a) Karcher Mean of COWs. (b) Extraction of COW from the sum images.

Figure 6.3 3D view of mean COWs

(a): Karcher mean of COWs; (b) COW extracted using Hessian matrix from the mean sum images, the average of all the twenty-two images

Extrapolating from Figure 6.3, the diameter of each vessel from the mean is far from accurate in comparison with each individual's COW displayed in Figure 6.2. Therefore reconstruction of COW to its rightful width is underway, which requires skelectionisation first. In this regard, due to the variations in diameters along the same vessel, the procedure of the skeletonisation can produce a number of untoward bifurcations. The reconstruction therefore only takes place for those key vessels, i.e., BA, ICA, ACA, and MCA, while retaining those smaller daughter vessels at the size of 1 pixel, equivalent to 0.8mm. Figure 6.4 portrays the skeletonisation (a), dilation with specified diameters (b), smooth of dilation (c), and a different viewpoint of the final reconstructed COW (d).

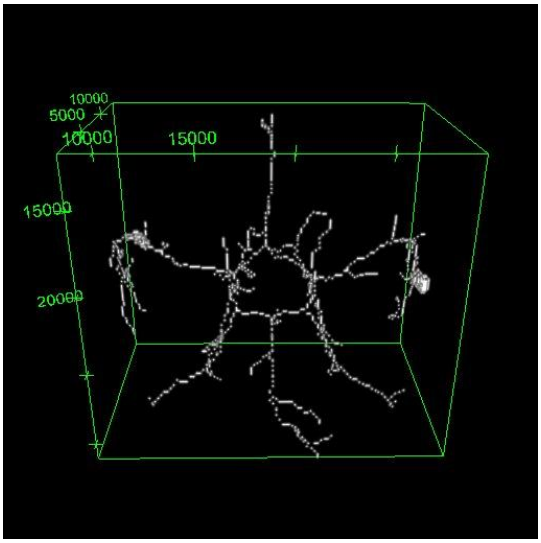

(a) Skeleton of COW.

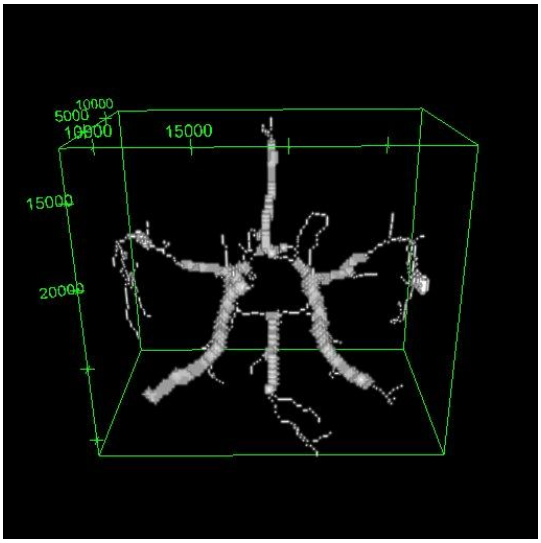

(b) Dilation of (a).

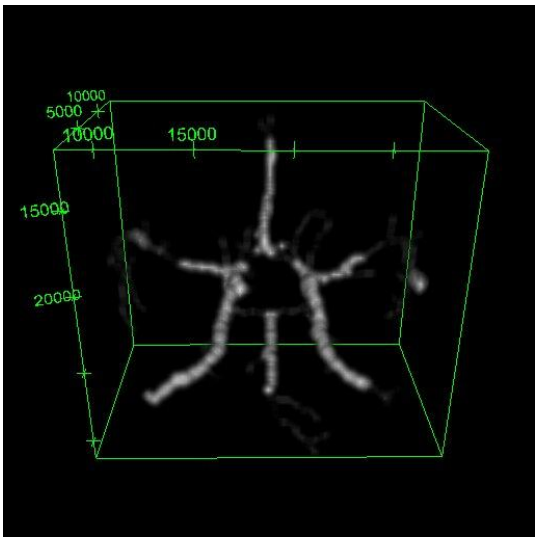

(c)Smooth of (b)

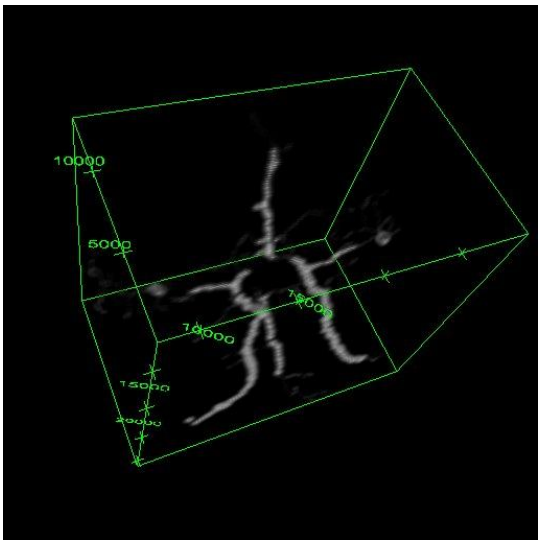

(d) Top view of (c)

Figure 6.4 Reconstruction of the Circle of Willis (COW)

Significantly, Figure 6.4 presents a demonstrable missing of one ACA in comparison with that in Figure 3.7 (a) showing two anterior cerebral arteries. This can be ascribed to the very closeness and interlacing nature of the two ACAs in terms of their spatial positions. As a result, it is difficult to discern one from another precisely from the mean COW as presented in Figure 6.3 (a). To assuage this cause, alternatively, Figure 6.5 tailors the COW with two ACAs as a complementary template, in which the two ACAs are constructed to be in near parallel positions. The subsequent preliminary clinical study serves to show the two templates work the same way on course to assist surgical path planning.

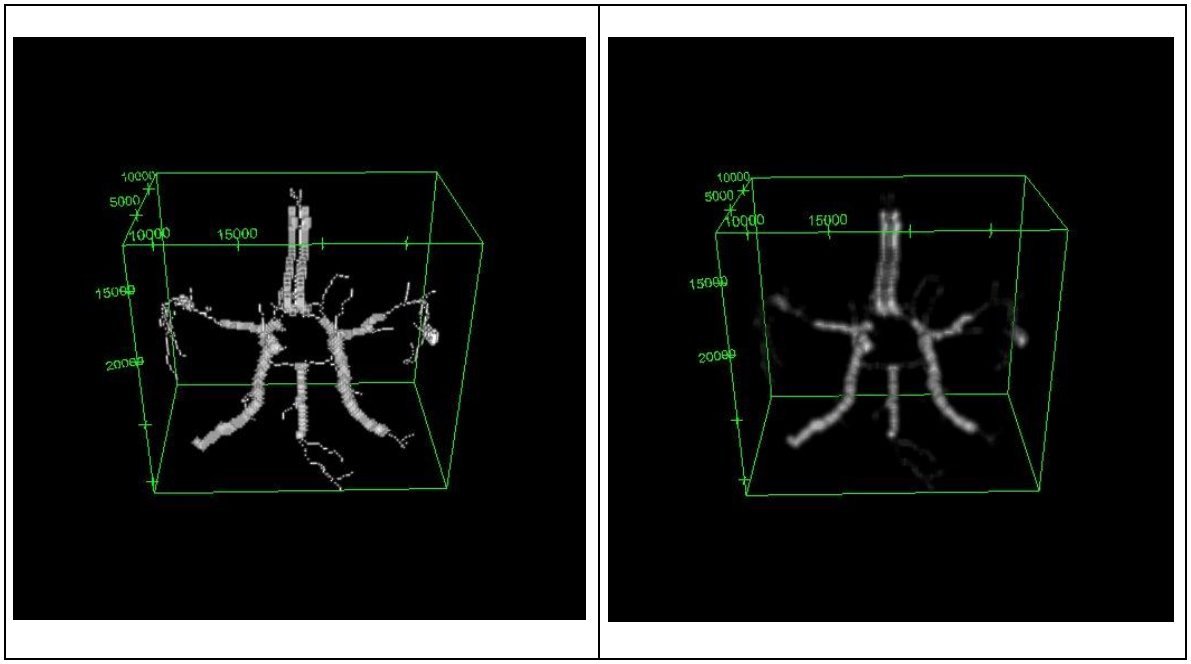

Figure 6.5 The reconstructed COW template with two ACAs

Left: the reconstructed COW. Right: the smooth version of left.

6.2 The analysis of variation of the mean COW

To evaluate the veracity of the mean COW, statistically, with reference to the analysis of shape variations, a volume based approach has been widely employed [24, 25, 16] which is fathomed with the following formulae, including volume index, similarity index and difference index.

$$VI = \frac{Vi}{Vm} \tag{6.1}$$

$$SI = 2\frac{Vi \cap Vm}{Vs + Vm} \tag{6.2}$$

$$DI = 2\frac{|Vi - Vm|}{Vi + Vm} \tag{6.3}$$

Where, *VI*, *SI*, *DI* refer Volume Index, Similarity Index, and Difference Index respectively, *Vi*, *Vm*, *Vs* indicate Volume (Individual), Volume (Mean), and Volume (Subject) respectively.

In these measures, the volume index (VI) denotes the entire volume change between each individual data with reference to the mean, whereas the similarity index (SI) indicates the overlapping region between each individual and the mean data. The difference between mean volume and each individual is measured using difference index (DI). Figure 6.6 displays the plots of these three measures of VI, SI, and DI for both 22 sets of control data that have been employed to derive the mean and six sets of additional test data to be used to evaluate the obtained mean.

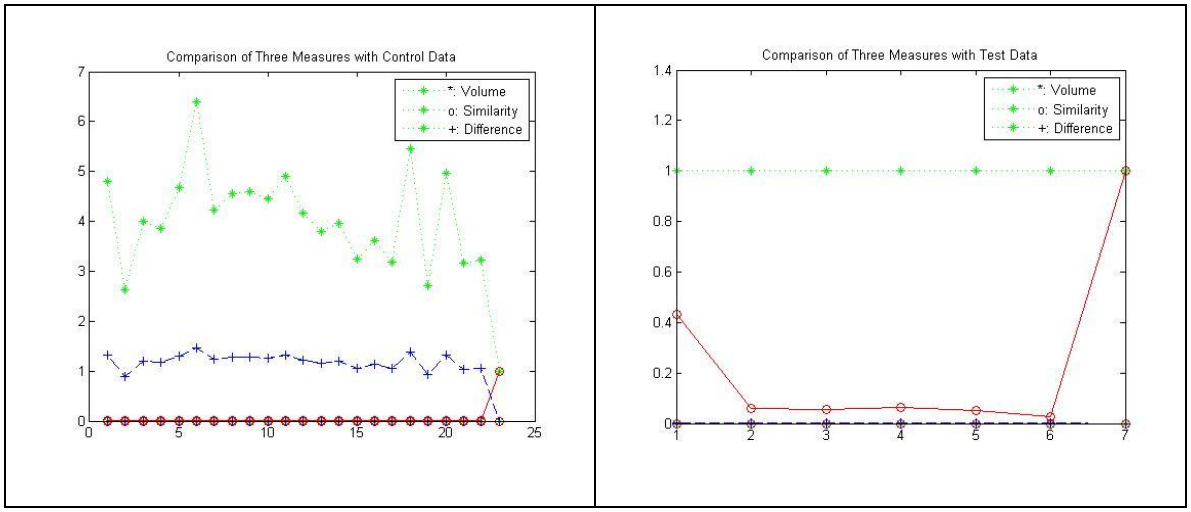

Figure 6.6 The plots of VI, SI and DI between control data (left) and test data (right) and the mean

VI (top curve), SI (bottom on left graph and middle on right graph) and DI (middle on left and bottom on right). The mean data are numbered as the last, i.e., no 23 in the left and no 7 in the right graph.

The standard deviations of the three measures (i.e., VI, SI, DI) for the test data are 0.0367, 0.3510, 0.0383 respectively, whereas the volume of the Karcher mean entails pixels of around 11,100. From the volume point of view, the mean COW does represent a typical Circle of Willis with sub-pixel variations in all three measures, especially for the additional test data, which implies the accuracy of the mean COW and points to the appropriateness of the synergy of the above approaches for the calculation of the mean COW. However, since the number of test datasets remains a small sample, more data will

be collected in the future to further verify this assumption. In terms of the template of COW, the visual comparison with the test data is demonstrated in Figure 6.7 where the COW template is shown in red colour. To show a clearer picture, each graph only depicts two of the six sets of data (in blue and green respectively) in comparison with the COW template (in red). In particular, each vessel volume in the test data is evidently comparable with its counterpart in the COW template.

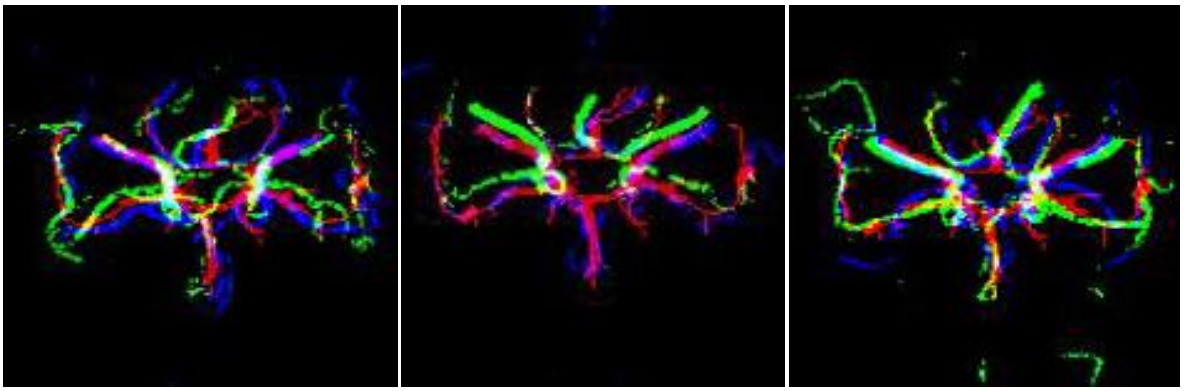

Figure 6.7 Visual comparison between six test datasets and the COW template with two shown in each graph

The COW template is in red colour whereas the test data are in blue and green.

6.3 A clinical application

A clinical study has been put forth to verify the applicability of the obtained COW template, abbreviated as T-COW, and is attested in Figure 6.8. The top row of the figure shows MR images whereas the bottom the superimposed images of MR on the MRA of the same patient. The arrows on Figure 6.8 (a) and 6.8(b) indicate the tumour location at two different view angles, i.e., axial and coronal views, while Figure 6.8(c) refers to the

real surgical path initially drafted based on the T-COW. On the bottom row, the planned path is superimposed with the patient's own COW network (f). Graphs (d) and (e) clearly indicate that the surgical path has well avoided the COW vessels while maintaining the optimal distance.

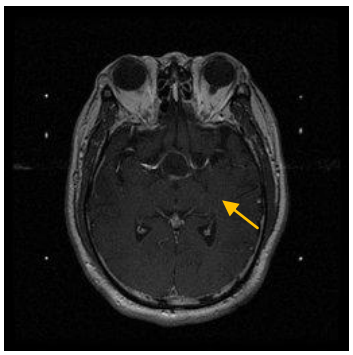

(a) Axial view of the tumour pointed by an arrow.

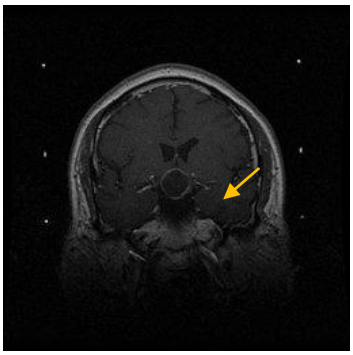

(b) Coronal view of MR image.

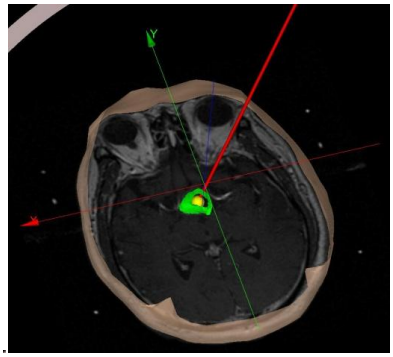

(c) Operative path indicated by the vertical red line.

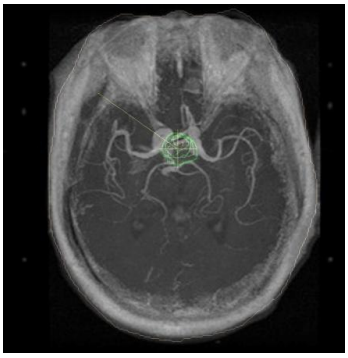

(d) Axial view of path superimposed with patient's COW.

(e) Coronal view of path superimposed with patient's COW.

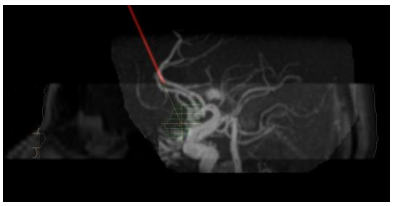

(f) Sagittal view of path superimposed with patient's COW.

Figure 6.8 An example of surgical planning for tumour removal

6.4 Summary

This thesis initiates the synergy of the current state of the art image processing techniques into rendering of the COW template, with an intention to enhance the cutting edge technology of image guided neurosurgery. As an immediate application, the COW template will benefit the planning process for designing operative paths. In the long term, it can also foster the service of diagnosis of cerebral vascular diseases as well as any other neuro-intervention of relevance. Both preliminary clinical studies and veracity analysis have confirmed the applicability of the COW template.

The availability of a digital mean brain artery architecture has not been reported before. To cement this gap and benefit a wider community working on the field of neuro-intervention, this work aims at providing a template of the Circle of Willis for the initial application of path planning in the procedure of image guided neurosurgery. The average diameters of COW vessels are also fathomed not only to be employed to reconstruct a COW template but also to act as a reference for the future similar work. As demonstrated in Figure 6.8, the planning of the optimal path has to take into consideration the distribution of COW comprehensively in order to achieve maximum resection of tumours while maintaining minimum mortality and complication morbidity rate, a task that can only be conducted by experienced surgeons at present. With the arrival of the COW template, it is anticipated that junior clinicians can learn from doing whilst senior doctors are able to make faster and more improved decisions.

Due to the lack of correspondences between points among individual COW shapes extracted from each image dataset, the calculation of the mean dataset poses a

challenging task. With the application of differential geometry, including Riemannian metrics, geodesics, and exponential maps, statistics on these shapes can be defined and compounded. Since the Fisher-Rao metric remains the only one that is invariant of re-parameterisation, it makes the appropriate choice of metric in this study.

It is conspicuous that the width of a vessel varies along its length, whilst the creation of the template COW has the same width along each key artery between any two bifurcations. With mean standard deviation being 0.39 mm, tantamount to half of a pixel (i.e., 0.8mm), those variances appear to pale into insignificance when it comes to visualisation. Nevertheless, more data will be made available in the future to further fathom this assumption.

On the other hand, in the process of calculating a mean shape, the limitation of computer power remains to be confronted, i.e., more datasets require more memory and computing power, especially when images are in high resolutions. In this investigation, the mean COW at the pixel sizes of $0.8 \times 0.8 \times 0.8$mm, $0.9 \times 0.9 \times 0.9$mm and $1 \times 1 \times 1$mm are calculated, whereas any higher resolutions have to call for the availability of extra resources, such as parallel computing. In the light of a pixel size of $0.8 \times 0.8 \times 0.8$mm, it might only take several minutes to complete the calculation of a mean shape. However, visualisation of all COWs in a 3D fashion of Figure 6.2 is quite a task if not impossible with the current existing computer hardware. Parallel implementation of such an algorithm will definitely help. In addition, in this study, the vessel length of each artery between bifurcations takes the averaged length dwelled on the mean COW and hence has

not been measured individually, future study will further this direction to verify if there is any significant untoward result.

7. Conclusion and Future works

7.1 Conclusion

As a minimally invasive operation, image guided stereotactic operation has been presented as one of the most important treatments in modern neurosurgery. Path planning for stereotactic operations normally depends on a neurosurgeon's clinical experience. A few medical software systems provide modules for path planning and training, but it is not good enough for practical use. Therefore, the research seeks to develop a novel module for surgical path planning of stereotactic neurosurgery by taking into consideration functional regions, the distributive pattern of blood vessels and an expert system. In this research, the distortion of MR images has been reduced to minimal level, ensuring MRI data used for path planning are reliable. Works on clinical data acquisition and analysis have been done, and the initial results show that the tumours with proximal positions result in similar surgical path. The relationship between tumours and the surgical paths is the fundamental discipline, which guides us to build the expert system. As an important part, a cerebral vascular template has been built, providing a reference to minimize the vessels' damage during the process of automatic surgical path planning. A novel approach can be developed finally, and it will be an evolution not only in computing technology but practical clinic works. The module will be able to create a stereotactic surgical path basing on the distributive pattern of functional regions and blood vessels automatically, which can be used by surgeons and medical students for training purposes.

7.2 Future works

The whole process of this study can be concluded as shown Figure 7.1.

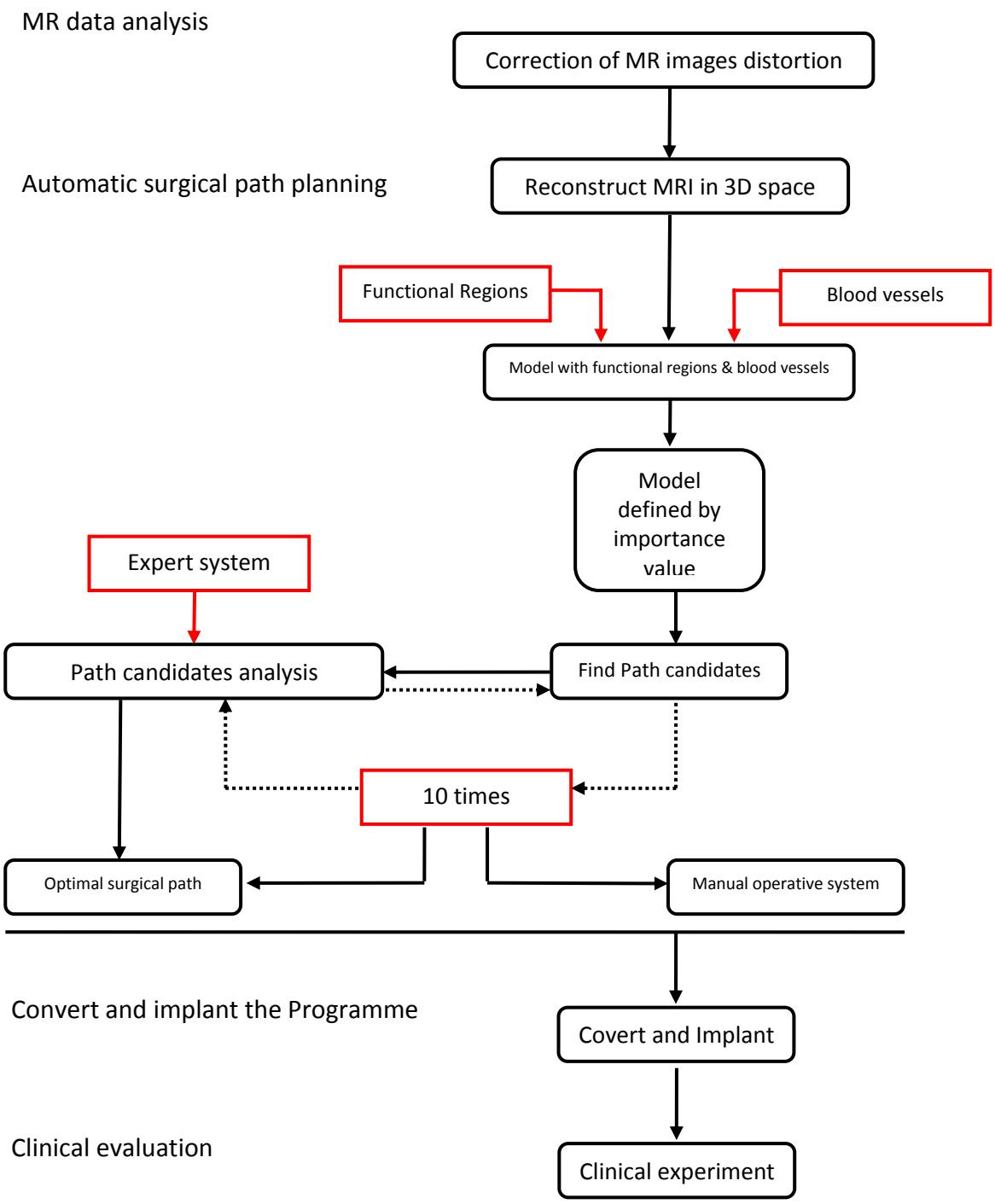

Figure 7.1 A flowchart of automatic surgical path planning process in this study

7.2.1 Initial programming

This phase involves the development of the algorithm for path planning associated with functional region classification and the distribution pattern of blood vessels. Namely, a safe surgical path must avoid blood vessels, functional cortex and nuclei, i.e., those crucial functional regions, and should incur the minimal distance toward the target. In reality, a surgeon considers the minimal distance as the first criterion to plan a surgical path to minimise the sacrifice of healthy tissues

To calculate the minimal distance, the Matlab platform is employed in this study. A Canny edge detector is used to find out the brain edge from the sample image which is a 2D MRI slice. The Euclidean distance between every point on the brain edge and the given point, namely centre point of a tumour, is calculated by classic distance formula. Initially, the minimal distance between a given point and the edge of the brain in a 2D slice can be easily calculated by the programme developed on the Matlab platform (Figure 7.2) for this research. However, the surgical path which has minimal Euclidean distance does not necessarily represent the perfect path for the image-guide neurosurgical operation. Blood vessels and functional structures have to be taken into account in the surgical path planning. Therefore, a cost function should be introduced in this study in the future works.

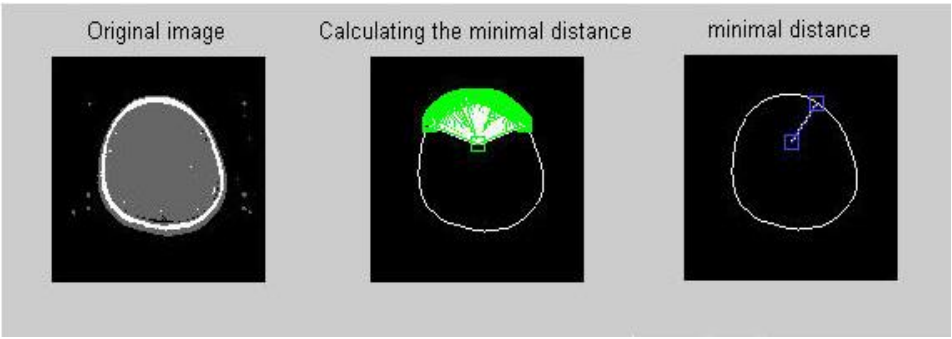

Figure 7.2 Three snapshot pictures captured at three time points during the process of minimal distance calculation on Matlab platform

Left figure: the original MRI slice after segmentation; Middle figure: the snapshot picture shows the process of minimal distance calculation; Right figure: the minimal distance has been calculated.

7.2.2 Programming based on cost functions

The cost function has been used to find the optimal surgical path in some studies [101,126, 127]. However, they are not completely suitable for practical clinical works as described above. In this study, a proper cost function will be used and realised on the Matlab platform following these steps:

1. Implant standard distribution pattern of blood vessels and functional regions to experimental MRI series and reconstruct them into a 3D version which is named as ModelBrain;

2. Depending on the fatalness of different intracranial structures, brain tissues in the ModelBrain are defined with an importance value respectively and divided into 8 degrees (Table 7.1). As an exception, vessels including arteries and veins are absolutely untouchable, therefore they have ∞ importance value.

Table 7.1 Importance values of different introcranial structures

Intracranial structures	White matters	Cortex	Neuronal tracts	Nuclei	Grey Matters	Functional Regions	Veins venous sinus	Arteries
important value	1	2	3	4	5	6	∞	∞

3. Costs of different intracranial structures will be added up, and a minimal linear cost accumulation line which has more than 10mm distance to the vessels' trunks will be qualified as path candidates. Some parameters are variable and generate inferior quality path candidates fitting the expert system which is described as follows.

7.2.3 Establishment of an expert system

The expert system for a safe insertion surgical path is the most distinguishing part of this research. The experience of neurosurgeons has been used to evaluate the automatic surgical path in some studies, however, it is not so efficient [128]. A one-hundred-case database has been analysed with reference to the positions of tumours and path angles. So far, it shows a certain degree of relativity between them, which is the tumours with proximity positions will result in similar surgical paths. A primary expert system will be built up based on this finding. Other features of tumours, such as size, shape and content are considered as important factors which will also be considered by the expert system to be developed. After that, the system will create a virtual surgical path under these criteria. The expert system then has the ability to choose the one path candidate which has less than 5mm distance to the virtual path as an optimal surgical path. If there is no surgical path conformity from the expert system, more path candidates will be calculated with inferior quality and analyzed by the expert system. After it repeats 10 times, an existing manual operative system for surgical path planning will be launched in case the expert system is unable to find the proper path. Although the database of MR images in this study has a limited coverage of brain tumours (only craniopharyngioma is included), this system can be promoted theoretically to choose optimal surgical paths in other clinical cases.

7.2.4 Convert and implant the programme

A new module originating from the Matlab codes for path planning for stereotactic operation will be converted to C++ and added as a member of modules in the 3D slicer as a plug-in. The interface of the module will be friendly and easily to operate, and will be compatible and associable with other modules in the 3D slicer.

7.2.5 Evaluation

1. Testing the module in progress.

2. Test the final software in practical neurosurgical operation at the Navy General Hospital in China.

Reference

1 Gao W X. The anatomy of Tele-neurosurgery in China. *International Journal of Telemedicine and Applications* 2011, doi:10.1155/2011/353405 (2011).

2 Ballantyne G H. Robotic surgery, telerobotic surgery, telepresence, and telementoring. Review of early clinical results. *Surg Endosc* Oct 16(10), 1389-1402 (2002).

3 Wu C Y, Wang Y H, Meng F G,Liu Y G. Development of stereotactic neurosurgery in China. *Neurosurgery* Apr 56(4), 851-860 (2005).

4 Benabid A. Deep brain stimulation for Parkinson' s disease. *Curr. Opin. Neurobiol.* 13, 696-706 (2003).

5 Czyż M, Tabakow P, Jarmundowicz W,Lechowicz-Głogowska B. Intraoperative magnetic resonance-guided frameless stereotactic biopsies - initial clinical experience. *Neurol Neurochir Pol.* Mar-Apr 46(2), 157-160 (2012).

6 Rajshekhar V. Rate of recurrence following stereotactic aspiration of colloid cysts of the third ventricle. *Stereotact Funct Neurosurg* 90(1), 37-44 (2012).

7 Karavitaki N, Cudlip S, Adams C B T,Wass J A H. Craniopharyngiomas. *Endocrine Reviews* 27(4), 371-397 (2006).

8 Hasegawa T, Kondziolka D, Hadjipanayis C G,Lunsford L D. Management of cystic craniopharyngiomas with phosphorus-32 intracavitary irradiation. *Neurosurgery* 54, 813-822 (2004).

9 Yu X, Liu R, Wang Y M, Wang H W, Zhao H L,Wu Z H. Infrasellar craniopharyngioma. *Clinical Neurology and Neurosurgery* 114, 112-119 (2012).

10 Shahzadi S, Sharifi G, Andalibi R, Zali A,Ali-Asgari A. Management of Cystic Craniopharyngiomas with Intracavitary Irradiation with 32P. *Arch Iranian Med* 11(1), 30-34 (2008).

11 Gao X W, Muller H,Deserno T. Integration of Medical Images in the Digital Hospital. *The Open Medical Informatics Journal* 5 (Suppl 1), 17-18 (2011).

12 Maciunas R J. Computer-assisted Neurosurgery. *Clinical Neurosurgery* 53, 267-271 (2006).

13 Itakura T. Neurosurgery in the 21st century--development of stereotactic and functional neurosurgery. *No Shinkei Geka* Apr 30(4), 351-356 (2002).

14 Tian Z M, Lu W S, Wang T M, Liu D, Chen Y, Zhang G L, Zhao Q J, Bai M M,Yin F. Clinical application of robotic tele-manipulation system in stereotactic surgery. *Chin J Neurosurgery* Dec 15 45(24), 1679-1681 (2007).

15 Horsley V. The linacra lecture on the function of the so called 'motor' area of the brain. *Br Med J* 21, 125-132 (1909).

16 Spiegel E A, Wycis H T,Marks M. Stereotactic apparatus for operations on the human brain. *Science* 106, 349-350 (1947).

17 Leksell D G. Stereotactic radiosurgery. *Neurol Res* 9, 60-68 (1987).

18 Brown R A. A computerized tomography-computer graphics approach to stereotaxic localization. *Journal of Neurosurgery* 50(6), 715-720 (1979).

19 Brown R A. A stereotactic head frame for use with CT body scanners. *Invest Radiol* 14(4), 300-304 (1979).

20 Golfinos J G, Fitzpatrick B C, Smith L R,Spetzler R F. Clinical use of a frameless stereotactic arm: results of 325 cases. *Journal of Neurosurgery* 83(2), 197-205 (1995).

21 Yu X, Liu Z H, Tian Z M, Li S Y, Huang H Y, Xiu B,Zhao Q J. Stereotactic biopsy for intracranial space-occupying lesions: clinical analysis of 550 cases. *Stereotact Funct Neurosurg* 75, 103-108 (2000).

22 Mendez I, Hill R, Clarke D,Kolyvas G. Robotic long-distance telementoring in neurosurgery. *Neurosurgery* 56, 434-440 (2005).

23 Tian Z M, Lu W S, Wang T M, Ma B L, Zhao Q J,Zhang G L. Application of a Robotic Telemanipulation System in Stereotactic Surgery. *Stereotact Funct Neurosurg* 86, 54-61 (2008).

24 Raimondi A J,Rougerie J. A critical review of personal experiences with craniopharyngioma: clinical history, surgical technique and operative results. *Pediatr Neurosurg* 21, 134-150 (1994).

25 Saxer F. Ependymepithel, gliome und epithelische geschwuelste des zentralenervensystems. *Ziegler's Beitraege* 32, 276 (1902).

26 Banna M. Craniopharyngioma: based on 160 cases. *Br J Radiol* 49, 206–223 (1976).

27 Susman W. Embryonic epithelial rests in the pituitary. *Br J Surg* 19, 571-576 (1932).

28 Cushing H. The craniopharyngioma in *Intracranial tumours. London: Bailliere, Tindall and Cox* 93–98 (1932).

29 Lewis D D. A contribution to the subject of tumours of the hypophysis. *JAMA* 55, 1002-1008 (1910).

30 Petito C K, Girolami U D,Earle K. Craniopharyngiomas. A clinical and pathological review. *Cancer* 37, 1944–1952 (1976).

31 Paja M, Lucas T, Garcia-Uria F, Salame F, Barcelo B,Estrada J. Hypothalamic-pituitary dysfunction in patients with craniopharyngioma. *Clin Endocrinol (Oxf)* 42, 467–473 (1995).

32 Karavitaki N, Brufani C, Warner J T, Adams C B T, Richards P, Ansorge O, B B S, Turner H E,Wass J A H. Craniopharyngiomas in children and adults: systematic analysis of 121 cases with long-term follow-up. *Clin Endocrinol (Oxf)* 62, 397–409 (2005).

33 Gonzales-Portillo G,Tomita T. The syndrome of inappropriate secretion of antidiuretic hormone: an unusual presentation for childhood craniopharyngioma: report of three cases. *Neurosurgery* 42, 917–921 (1998).

34 Waga S,Handa H. Radiation-induced meningioma: with review of literature. *Surg Neurol* 5, 215–219 (1976).

35 Van-den-Bergh P,Dom R. Wallenberg's syndrome caused by a craniopharyngioma 'en plaque'. *J Neurol* 229, 61-64 (1983).

36 Van-Effenterre R,Boch A L. Craniopharyngioma in adults and children. *J Neurosurg* 97, 3-11 (2002).

37 Banna M, Hoare R D, Stanley P,Till K. Craniopharyngioma in children. *J Pediatr* 83, 781–785 (1973).

38 Russell R W,Pennybacker J B. Craniopharyngioma in the elderly. *J Neurol Neurosurg Psychiatry* 21, 1-13 (1961).

39 Matson D D,CriglerJr J F. Management of craniopharyngioma in childhood. *J Neurosurg* 30, 377–390 (1969).

40 DeVile C J. Craniopharyngioma in *Oxford textbook of endocrinology and diabetes* (eds Wass J A H,Shalet S M) 218–225 (Oxford University Press, 2002).

41 Pusey E, Kortman K, Flannigan B, Tsuruda J,Bradley W G. MR of craniopharyngiomas: tumor delineation and characterization. *AJR Am J Roentgenol* 149, 383–388 (1987).

42 Hald J K, Eldevik O P, Brunberg J A,Chandler W F. Craniopharyngiomas—the utility of contrast medium enhancement for MR imaging at 1.5 T. *Acta Radiol* 35 (1994).

43 Sartoretti-Schefer S, Wichmann W, Aguzzi A,Valavanis A. MR differentiation of adamantinous and squamous-papillary craniopharyngiomas. *Am J Neuroradiol* 18, 77-87 (1997).

44 Caruso R D, Rosenbaum A E, Sherry R G, Wasenko J J, Joy S E, Hochhauser L,Chang J K. Pituitary gland. Variable signal intensities on MRI. A pictorial essay. *Clin Imaging* 22, 327-332 (1998).

45 Harwood-Nash D C. Neuroimaging of childhood craniopharyngioma. *Pediatr Neurosurg* 21, 2-10 (1994).

46 Nagahata M, Hosoya T, Kayama T,Yamaguchi K. Edema along the optic tract: a useful MR finding for the diagnosis of craniopharyngiomas. *Am J Neuroradiol* 19, 1753-1757 (1998).

47 Karavitaki N, Brufani C, Warner J T, Adams C B T, Richards P, Ansorge O, Shine B, Turner H E,Wass J A H. Craniopharyngiomas in children and adults: systematic analysis of 121 cases with long-term follow-up. *Clin Endocrinol (Oxf)* 62 (2005).

48 De-Vile C J, Grant D B, Kendall B E, Neville B G R, Stanhope R, Watkins K E,Hayward R D. Management of childhood craniopharyngioma: can the morbidity of radical surgery be predicted? *J Neurosurg* 85, 73-81 (1996).

49 Davies M J, King T T, Metcalfe K A,Monson J P. Intraventricular craniopharyngioma: a long-term follow-up of six cases. *Br J Neurosurg* 11, 533-541 (1997).

50 Weiner H L, Wisoff J H, Rosenberg M E, Kupersmith M J, Cohen H, Zagzag D, Shiminski-Maher T, Flamm E S, Epsten F J,Miller D. Craniopharyngiomas: a clinicopathological analysis of factors predictive of recurrence and functional outcome. *Neurosurgery* 35, 1001-1011 (1994).

51 Baskin D S,Wilson C B. Surgical management of craniopharyngiomas. *J Neurosurg* 62, 22-27 (1986).

52 Fahlbusch R, Honegger J, Paulus W, Huk W,Buchfelder M. Surgical treatment of craniopharyngiomas: experience with 168 patients. *J Neurosurg* 90 (1999).

53 Yasargil G M, Curcic M, Kis M, Siegenthaler G, Teddy P,Roth P. Total removal of craniopharyngiomas. Approaches and longterm results in 144 patients. *J Neurosurg* 73, 3-11 (1990).

54 Honegger J, Buchfelder M, Fafhlbusch R, Daubler B,Dorr H G. Transsphenoidal microsurgery for craniopharyngiomas. *Surg Neurol* 37, 189-196 (1992).

55 Duff J M, Meyer F B, Ilstrup D M, Laws-Jr E R, Scleck C D,Scheithauer B W. Long-term outcomes for surgically resected craniopharyngiomas. *Neurosurgery* 46, 291–305 (2000).

56 Maira G, Anile C, Rossi G F,Colosimo C. Surgical treatment of craniopharyngiomas: an evaluation of the transsphenoidal and pterional approaches. *Neurosurgery* 36, 715–724 (1995).

57 Carpenter R C, Chamberlin G W,Frazier C H. The treatment of hypophyseal stalk tumours by evacuation and irradiation. *Am J Roent* 38, 162-167 (1973).

58 DI D I S, Chang C H, Harisiadis L,Carmel P W. Treatment results of craniopharyngiomas. *Cancer* 47, 847-852 (1981).

59 Regine W F,Kramer S. Pediatric craniopharyngiomas: longterm results of combined treatment with surgery and radiation. *Int J Radiat Oncol Biol Phys* 24, 611-617 (1992).

60 Jose C C, Rajan B, Ashley S, Marsh H,Brada M. Radiotherapy for the treatment of recurrent craniopharyngioma. *Clin Oncol (R Coll Radiol)* 4, 287-289 (1992).

61 Leksell L,Liden K. A therapeutic trial with radioactive isotopes in cystic brain tumour. Radioisotope techniques. *J Med Physiol Appl*, 1-4 (1952).

62 Szeifert G T, Julow J, Slowik F, Balint K, Lanyi F,Pasztor E. Pathological changes in cystic craniopharyngiomas following intracavital ^{90}yttrium treatment. *Acta Chir Scand* 102, 14-18 (1990).

63 Backlund E O. Studies on craniopharyngiomas III. Stereotactic treatment with intracystic yttrium-90. *Acta Chir Scand* 139, 237-247 (1973).

64 Pollock B E, Lunsford L D, Kondziolka D, Levine G,Flickinger J C. Phosphorus-32 intracavitary irradiation of cystic craniopharyngiomas: current technique and long-term results. *Int J Radiat Oncol Biol Phys* 33, 437-446 (1995).

65 Voges J, Sturm V, Lehrke R, Treuer H, Gauss C,Berthold F. Cystic craniopharyngioma: long-term results after intracavitary irradiation with stereotactically applied colloidal β-emitting radioactive sources. *Neurosurgery* 40, 263-270 (1997).

66 Bond W H, Richards D,Turner E. Experiences with radioactive gold in the treatment of craniopharyngioma. *J Neurol Neurosurg Psychiatry* 28, 30-38 (1965).

67 Yu X, Liu Z H,Li S Y. Combined treatment with stereotactic intracavitary irradiation and gamma knife surgery for craniopharyngiomas. *Stereotact Funct Neurosurg* 75, 117-122 (2000).

68 Sun J Z, Tian Z M, Yu X, Zhou D X, Qi S B,Wang Y M. Management of cran iopharyng iomas in sen ior patients with stereotactic 32 P intracav itary irradiation. *Chin J Neurosurg Dis Res* 8(1), 60-63 (2009).

69 Lunsford L D. Comment on cystic craniopharyngioma: longterm results after intracavitary irradiation with stereotactically applied colloidal β-emitting radioactive sources. *Neurosurgery* 40, 269-272 (1997).

70 Leber K A, Bergloeff J,Pendl G. Dose response tolerance of the visual pathways and cranial nerves of the cavernous sinus to stereotactic radiosurgery. *J Neurosurg* 88, 43-50 (1998).
71 Kawanaka A,Takagi M. Estimation of static magnetic field and gradient fields from NMR image. *J.Phys. E.: Sci. Instrum.* 19, 871-875 (1986).
72 Bakker C J G, Moerland M A, Bhagwandien R,Beersma R. Analysis of machine-dependent and object-induced geometric distortions in 2DFT MR imaging. *Magn. Reson. Imaging* 10, 597-608 (1992).
73 Moerland M A, Beersma R, Bhagwandien R, Wijrdeman H K,Bakker C J G. Analysis and correction of geometric distortions in 1.5 Tmagnetic resonance images for use in radiotherapy treatment planning. *Phys. Med. Biol.* 40 (1995).
74 Maciunas R J, Fitzpatrick J M, Gadamsetty S,Maurer C R. A Universal Method for Geometric Correction of Magnetic Resonance Images for Stereotactic Neurosurgery. *Stereotact Funct Neurosurg* 66, 137-140 (1996).
75 Balac S,Caloz G. Magnetic susceptibility artifacts in magnetic resonance imaging: calculation of the magnetic field disturbances *Magnetics. IEEE Transactions* 32, 1645-1648 (1996).
76 Gao X W, Anishenko S, Shaposhnikov D, Podladchikova L, Batty S,Clark J. High-precision Detection of Facial Landmarks to Estimate Head Motions Based on Vision Models. *Journal of Computer Science* 3(7), 528-532 (2007).
77 Arun K S, Huang T S,Blodstein S D. Least squares fitting of two 3-d point sets. *IEEE Trans. Pattern Anal. Machine Intell.* 9, 698-700 (1987).
78 Klema V. The singular value decomposition: Its computation and some applications. *Automatic Control, IEEE Transactions* 25, 164-176 (1980).
79 Challis J H. A procedure for determining rigid body transformation parameters. *Journal of Biomechanics* 28(6), 733-737 (1995).
80 Ramos J A,Verriest E I. Total Least Squares Fitting of Two Point Sets in m-D. *Decision and Control, 1997, Proceedings of the 36th IEEE Conference* 5 (1997).
81 Alexander E, Kooy H M, Herk M V, Schwartz M, Barnes P D, Tarbell N, Mulkern R V, Holupka E J,Loeffler J S. Magnetic resonance image—directed stereotactic neurosurgery: use of image fusion with computerized tomography to enhance spatial accuracy. *J of Neurosurg* 83, 271-276 (1995).
82 Cohen D S, Lustgarten J H, Miller E, Khandji A G,Goodman R R. Effects of coregistration of MR to CT images on MR stereotactic accuracy. *J Neurosurg* 82, 772-779 (1995).
83 Eggers G, Rieker M, Fiebach J, Kress B, Dickhaus H,Hassfeld S. Geometric accuracy of magnetic resonance imaging of the mandibular nerve *Dentomaxillofacial Radiology* 34, 286-291 (2005).
84 Wang D, Doddrell D M,Cowin G. A novel phantom and method for comprehensive 3-dimensional measurement and correction of geometric distortion in magnetic resonance imaging. *Magnetic Resonance Imaging* 22(4), 529-542 (2004).
85 Viard R, Mordon S, Betrouni N, Vermandel M, Vanhoutte M,Rousseau J. Correction of images in an open-configuration MR imaging system for radiation

therapy planning and Interventional MRI. *Computer-Assisted Radiology and Surgery* 3(3-4), 283-289 (2008).

86 Biller J. in *Localization in Clinical Neurology* (eds Brazis P W, Msadeu J C,Biller J) (Little, Brown, and Co., Boston, 1990).

87 Caplan L R,Bogousslavsky J. *Stroke syndromes and uncommon causes of stroke*. (Cambridge University, 2001).

88 Greene K A, Marciano F F, Dickman C A, Coons S W, Johnson P C, Bailes J E,Spetzler R F. Anterior communicating artery aneurysm paraparesis syndrome: Clinical manifestations and pathologic correlates. *Neurology* 45, 45-50 (1995).

89 Bornstein R,Brown G. *Cerebrovascular Disease*. (Oxford University Press, 1991).

90 Srivastava A, Jermyn I,Joshi S H. Riemannian Analysis of Probability Density Functions with Applications in Vision. *CVPR 2007* (2007).

91 Chui H, Rangarajan A, Zhang J,Leonard C M. Unsupervised learning of an atlas from unlabeled point-sets, Pattern Analysis and Machine Intelligence. *IEEE Transactions* 26(2), 160-172 (2004).

92 Chen T, Vemuri B C, Rangarajan A,Eisenschenk S J. Group-wise Point-set registration using a novel CDF-based Havrda-Charvát Divergence. *International journal of computer vision* 86(1), 111-124 (2010).

93 Rao C R. Information and accuracy attainable in the estimation of statistical parameters. *Bull. Cal. Math. Soc.* 37, 81-91 (1945).

94 Chen T, Rangarajan A, Eisenschenk S J,Vemuri B C. Construction of a neuroanatomical shape complex atlas from 3D MRI brain structures. *NeuroImage* 60(3), 1778-1787 (2012).

95 She F H, Chen R H, Gao W M, Hodgson P D, Kong L X,Hong H Y. Improved 3D Thinning Algorithms for Skeleton Extraction. *Digital Image Computing: Techniques and Applications* (2009).

96 Vals-Miro J,White A S. Quasi-optimal trajectory planning and control of a CRS A251 industrial robot. *J Systems and Control, Proc. Inst Mech Eng* 216, 343-356 (2002).

97 Elnagar A,Lulu L. A global path planning Java-based system for autonomous mobile robots. *Science of Computer Programming* 53, 107-122 (2004).

98 Gering D T, Nabavi A, R R K, Grimson W E L, Hata N, Everett P, Jolesz F A,Wells-III W M. An Integrated Visualization System for Surgical Planning and Guidance using Image Fusion and Interventional Imaging. *Int Conf Med Image Comput Comput Assist Interv* 2, 809-819 (1999).

99 Joshi A, Scheinost D, Vives K P, Spencer D D, Staib L H,Papademetris X. Novel interaction techniques for neurosurgical planning and stereotactic navigation. *IEEE Transactions on Visualization and Computer Graphics* 14(6), 1587-1594 (2008).

100 Vaillant M, Davatzikos C, Taylor R H,Bryan R N. A path-planning algorithm for image-guided neurosurgery. *CVRMed-MRCAS'97* 1205, 467-476 (1997).

101 Fuji T, Emoto H, Sugou N, Mito T,Shibata I. Neuropath planner-automatic path searching for neurosurgery. *International Congress Series* 1256, 587-596 (2003).

102 Bosmans H, Marchal G, Van-Hecke P,Vanhoenacker P. MRA review. *Clin Imaging* 16(3), 152-167 (1992).

103 Gao X W, Qian Y,Hui R. The state of the art of medical imaging technology: from creation to archive and back. *The Open Medical Informatics Journal* 5(Suppl 1), 73-85 (2011).

104 Tian Z M, Zhao Q J, Du J X, Wang T M, Liu D,Lv H B. Use of robot in frameless stereotactic neurosurgery. *Chinese Journal of Minimally Invasive Neurosurgery* 5(3), 56-58 (2000).

105 Zylka W,Wischmann H A. On geometric distortions in CT images, Engineering in Medicine and Biology Society, 1996. Bridging Disciplines for Biomedicine. *Proceedings of the 18th Annual International Conference of the IEEE* (1996).

106 Mauter C M,Fitzpatrick J M. A Review of Medical Image Registration in *Interactive image-guided Neurosurgery* (ed Maciunas R J) (American Association of Neurological Surgeons, 1993).

107 Pieper S, Halle M,Kikinis R. 3D Slicer. *the 1st IEEE International Symposium on* Biomedical Imaging: From Nano to Macro 1, 632-635 (2004).

108 Simmross-Wattenberg F, Carranza-Herrezuelo N, Palacios-Camarero C, Casaseca-de-la-Higuera P, Martín-Fernández M A, Aja-Fernández S, Ruiz-Alzola J, Westin C F,Alberola-López C. Group-Slicer: a collaborative extension of 3D-Slicer. *J Biomed Inform* Dec;38(6), 431-442 (2005).

109 Henson J W, Ulmer S,Harris G J. Brain tumor imaging in clinical trials. *American Journal of Neuroradiology* 29, 419-424 (2008).

110 Afshar F, Watkins E S,Yap J C F. in *Stereotaxic Atlas of the Human Brainstem and Cerebellar Nuclei. A Variability Study* (ed Afshar F) (Thieme Medical Publishers, 1978).

111 Wieslaw L N. Computerized Brain Atlases for Surgery of Movement Disorders. *Seminars in Neurosurgery* 12(2), 183-194 (2001).

112 Pierson R, Corson P W, Sears L L, Alicata D, Magnotta V, O'Leary D,Andreasen N C. Manual and Semiautomated Measurement of Cerebellar Subregions on MR images. *NeuroImage* 17(1), 61-76 (2002).

113 Statistical Parametric Mapping. *www.fil.ion.ucl.ac.uk/spm*. *Retrieved in May* (2013).

114 Frangi A F, Niessen W J, Vincken K L,Viergever M A. Multiscale vessel enhancement filtering. *In Medical Image Computing and Computer-Assisted Intervention - MICCAI '98*, 130-137 (1998).

115 Frangi A F, Niessen W J, Hoogeveen R M, Walsum T v,Viergever M A. Model-based quantitation of 3D magnetic resonance angiographic images. *IEEE Transactions on Medical Imaging* 18(10), 946-956 (1999).

116 Binmore K,Davies J. Calculus Concepts and Methods. *Cambridge University Press*, 190 (2007).

117 Rao C. Fisher-Rao Metric. *Scholarpedia,http://www.scholarpedia.org/article/Fisher-Rao_metric* 4(2), 2009 (2009).

118 *http://fiji.sc/AnalyzeSkeleton* retrieved in August (2013).

119 *http://rsbweb.nih.gov/ij/* Retrieved in August (2013).

120 Umeyama S. Least-squares Estimation of transformation parameters between two point ppatters. *IEEE Trans. Pattern Anal. Machine Intell* 13(4), 376-380 (1991).
121 Gao X W, Hui R, White A,Tian Z M. A new approach to estimation of non-isotropic scale factors in correction of MR distortion. *Int J CARS* 4, 349-350 (2009).
122 Tian Z M, Liu Z H, Du J X, Zhao Q J, Wang T M, Liu D, Tang Z S,Wang Z G. Clinic use of new robot in neurosurgery. *Chin J Neurosurgery* 16, 2-5 (2000).
123 Nimsky C, Fujita A, Ganslandt O, Keller B V, Kohmura E,Fahlbusch R. Frameless stereotactic surgery using intraoperative high-field magnetic resonance imaging. *Neurol Med Chir* 44, 522-534 (2004).
124 Pieper S, Lorensen B, Schroeder W,Kikinis R. The NA-MIC Kit: ITK, VTK, Pipelines, Grids and 3D Slicer as an Open Platform for the Medical Image Computing Community. *the 3rd IEEE International Symposium on* Biomedical Imaging: From Nano to Macro 1, 698-701 (2006).
125 Kikinis R,Pieper S. 3D Slicer as a tool for interactive brain tumor segmentation. *Conf Proc IEEE Eng Med Biol Soc* 2011, 6982-6984 (2011).
126 Dijkstra E. A note on two problems in connexion with graphs. *Numerische Mathematik 1*, 269–271 (1959).
127 Ellen J L. Automatic trajectory planning for deep brain stimulation: A feasibility study. *MICCAI 2007* Part I, LNCS 4791, 584–592 (2007).
128 Guo T, Parrent A G,Peters T M. Automatic Target and Trajectory Identification for Deep Brain Stimulation (DBS) Procedures. *MICCAI 2007* Part I, LNCS 4791, 483–490 (2007).

Appendix

Appendix 1: The aligned coordinate data for the path line target and 3 angles of the path line, which indicates the necessary parameters for neurosurgical path, described in part 5.3, will be employed to establish expert system.

patients(False name)	real-X	real-Y	real-Z		path-angle	
Chou ShuKang	-30.7949	32.1572	14.2991	46.7	-117.2	15
Tao Rui	6.0907	46.4984	7.3147	-54.8	-112.9	-22.6
Zhang HuiLin	-4.5809	31.0496	19.5849	38.2	-131.6	18.1
Zhang Jia Feng	14.0704	43.5245	-0.473	-34.9	-118.7	-13.4
GuJianFang	5.3026	34.655	17.4248	-27	-120.4	-27.3
Li Chang Sheng	-16.9186	61.3345	28.9274	37.8	-109.6	28
Liu Jun	-4.6813	49.0782	14.9803	43.1	-114.5	36.9
Liu Xie Mei	-5.2202	42.7611	21.7598	32.9	-122.3	35.1
Wang Qi	-9.2823	54.8898	14.6432	48	-119.5	23.9
Yu LunJi	-0.3477	48.5251	13.9744	-29.7	-116.3	-30.6
Zhao Feng Zhi	-3.5383	40.3048	10.9203	34.9	-123.2	29.7
Zhou YingChun	1.0905	42.2883	13.7624	-25.8	-121.7	-29.1
Chen AiMei	14.7097	40.5196	17.6488	-34.5	-126.5	-26.4
JiXingYu	24.0461	20.5768	-1.9296	-145.6	-119.9	-13.6
Wang PeiYu	2.9081	48.5311	10.7402	-26.6	-113.5	-26.5
GuHeng	-1.0091	46.6731	-2.0422	22.1	-114.3	25.4
Sun YiMin	2.1525	42.0824	24.8	-37	-118.5	-34.7
Wang Zhen	-2.0671	59.2653	17.2258	45	-129.3	34.9
Ye ShaoHong	0.1915	45.5501	2.9833	41.6	-124.9	28.4
Du YeHeng	9.8779	39.7602	22.6396	-30.4	-126.9	-29.8
Hou ShuLin	-3.0525	28.5766	24.6271	45.4	-118.2	22.2
Sun JingXiang	-3.3323	34.7522	26.1706	53.5	-123.6	27.4
Yan ChengHe	-4.7299	47.0445	9.3411	37.5	-129.3	24.1
Zhang Po	-2.3338	48.1634	22.0622	42.2	-117.1	21
Du HuiWei	0.8281	41.2015	14.4677	-28.6	-127.6	-18.3
Gao JinNa	8.2186	46.2687	10.2703	-34.1	-123.1	-25.5
Liu Chao	12.1068	55.036	-5.5952	-56.1	-107.4	-12.6
ShuiYuHong	-5.4134	47.8823	20.1235	54.5	-118.1	33.8
Yang TianYu	-0.1045	46.4306	5.7619	50.1	-111.3	24.9
Zhang YanAn	4.1556	42.3762	10.1483	-45.2	-117.4	-24.4
Dong ChengGang	0.4562	46.9982	12.6855	-34.4	-127.6	-21
Gao RenCai	2.2467	44.5811	-4.177	-53.3	-128.9	-36.7
GuoYongHua	-1.4368	37.0788	10.4156	47.3	-122.2	24.1
JinJiaJia	0.7847	46.7208	11.6629	-57.3	-123.6	-41
Su XinYue	-8.9246	38.5224	5.2644	61.1	-128.9	42.4

Tao XinYuan	-14.0487	53.2497	10.9959	43.7	-128.6	26.7
Wang HaiHe	0.9153	47.6938	13.2327	-54.6	-127.8	-32.8
Wang RuiRui	0.2559	49.3627	9.6983	-44.3	-139.8	-20.6
Zhang LianYing	-0.4307	43.1174	12.335	59	-124.5	32.5
Zhao JinZhong	1.3213	45.4994	3.0024	-56.1	-127.9	-29.9
Cao Ou	5.4672	59.3576	-4.2222	-59.7	-114.7	-27.6
Chao Yuan	0.3283	32.6985	17.6217	-53.3	-118.7	-30.4
Cui Yan	-1.5495	40.0732	7.4907	48.4	-124.8	40.1
GuoJianMin	27.0682	14.9577	22.5068	-27.4	-132.9	-15.2
Li ShuJu	9.4849	39.4194	4.4518	-50	-120.8	-22.2
Fang ShuYing	2.6249	47.5285	-11.5561	67.1	-120	37.3
Fang LiangBo	7.398	33.0483	22.2422	-57.2	-129.6	-39.7
Han ChengFei	14.9729	37.8184	4.9579	-41.5	-123.8	-21.5
Hu CuiLian	7.653	49.3413	12.3085	-50.1	-122.9	-36.1
Huang BingLin	8.3377	54.2373	20.1992	-48.5	-123.6	-27.6
JiBoFei	0.8661	53.2384	5.2794	-52.5	-129.8	-39.5
Li FuSheng	-5.5	46.9	2.6449	51.5	-112.7	23.8
Li GuiChen	5.3523	45.5723	11.5989	-56.9	-124.9	-31
Li Hui	3.7173	42.5365	12.8727	-42.6	-120.6	-20.3
Li XuNa	6.6149	33.9217	4.917	-31.6	-130.7	-23.2
Lu XingFu	-26.7311	33.0142	11.8141	26.9	-136.3	19.4
MengXiYang	-4.9417	37.4009	2.5696	50.3	-132.6	36
Qin HongChun	0.2016	57.5997	11.744	-57.5	-121.9	-35.5
Song FangWen	0.2241	40.4999	16.5475	-53.3	-124.4	-30.5
Tian MiYuan	4.308	48.0221	3.9266	-57.3	-119.9	-30.7
Yu ShengFeng	-0.2949	36.2994	11.4264	51.9	-133.5	31.2
Yu XiaoTian	5.3586	45.6983	0.3894	-51.3	-117.8	-30.6
Yue ZhiFeng	11.4604	36.1423	11.4619	-41.1	-128.4	-26.8
Zhang JingYu	4.9865	31.1412	26.1939	-59.6	-123.3	-33.1
Zhao DaShuang	-6.5525	43.1077	10.4506	43.9	-128.4	17.7
Zou XiaoHong	2.7253	42.8048	8.199	-60.6	-122.4	-35.9
Cao JianChao	4.9859	39.7421	15.8329	-47.5	-131.9	-37.9
Ding LeJiao	-6.4748	31.3	19.4917	-61	-122.1	-32.2
Dou YiEn	7.2269	44.2649	12.6293	-50	-126.1	-32.3
GuoLiNa	-5.1958	42.3618	11.4532	45.4	-135.5	37.5
Hu XiaoBin	19.0007	36.6309	8.0954	-41.1	-121.5	-27.1
Hu YongChun	2.0729	44.2706	9.6703	-48.3	-128.1	-41.3
Huang GuoXian	4.9489	35.6596	16.6372	47.9	-133.4	33.3
Huang ZhenFu	7.0096	39.0367	9.3486	-48.4	-136.9	-31.3
Lai FeiSai	-1.7742	36.8433	20.4353	56.2	-116.8	30.2
Li Gang	-5.2849	42.1986	10.5201	52.4	-123.4	27.9
Li JiaLian	3.2233	37.6451	19.7529	-58.3	-110.4	-35.6
Li Jie	1.7703	48.3065	12.6814	-69	-113.3	-45.1
Li QingEn	5.0956	40.6876	17.2336	-47.1	-121.8	-27

Lin Cui	-16.3196	34.2432	13.1616	50.8	-116	22.7
Lin Tian	4.3789	54.8639	15.3703	-48.6	-118.9	-31.6
Lu Jin	-2.3703	44.5168	17.1929	52.5	-119.5	28.8
Min YongQun	0.5304	36.5974	10.3447	-53.3	-117.4	-32.8
Ren JinWei	6.0865	45.1184	17.544	-53.3	-115.5	-30.7
Rong Liang	17.0767	58.3571	30.5853	-68.9	-120.8	-44.2
Sun ZhiAi	3.794	43.1391	18.1127	57.2	-120.1	37.9
Tang MengKe	-1.626	39.9681	-1.1346	-50.6	-120.9	-34.7
Wang Cheng	2.2268	39.6709	15.2194	-55	-124.8	-31.8
Wang Fang	0.8404	38.3941	17.0953	46.9	-118.7	24
Wang HaoFan	6.5889	37.3721	10.9184	-45.3	-119.9	-27.9
Wu Lei	11.8116	61.4119	23.7815	-64.1	-110.1	-21.4
Xia ZhenJuan	7.5988	41.1061	7.9657	-42	-124.7	-34.1
Xiao JingYun	4.9397	45.7748	13.3766	-48.6	-129.1	-35.9
Zhang GuoYi	-13.4741	45.7329	14.1779	45.4	-125	34.1
Zhang JinYe	2.1536	42.525	15.1657	-54	-133	-35.2
Zhu HaiYan	5.3775	37.272	17.983	-47.7	-117.1	-29.1
Chen GuiHua	14.829	60.2088	21.7505	-76	-107.7	-33
Li Jia	-27.021	36.6656	19.7948	73	-98.9	35.1
Pang LiLi	-8.9121	46.8694	-1.4114	47.2	-127.2	31.4
Hu XiaoBin2	-6.0727	41.5129	14.8408	61	-119.7	40.1

Appendix 2: Measurement results of primary and processed data for diameter ACA, MCA, ICA and BA, respectively.

Name	ACA							
	L			Mean	R			Mean
bai-YS	2.55	2.2	2.15	2.3	2.97	2.69	2.27	2.643333
Huang De Cheng	2.17	2.2	2	2.123333	2.2	2.04	2.13	2.123333
Liu Yun Cong	2.4	2.26	2.37	2.343333	2.67	2.45	2.53	2.55
Ma Gui Ling	2.75	2.93	3.22	2.966667	2.75	2.4	2.8	2.65
Peng Gong Bing	2.07	2.08	2.08	2.076667	2.28	2.28	2.78	2.446667
Qi Xia Wa	2.4	2.45	2.11	2.32	2.53	2.27	2.11	2.303333
Ren Shu Ying	2.15	2.72	2.4	2.423333	2.15	2.4	2.13	2.226667
Sun Shu Zheng	2.46	2.17	2.49	2.373333	2.21	2.39	2.52	2.373333
Tong Tui Yuan	2.75	2.47	2.77	2.663333	2.3	2.64	2.2	2.38
Wang Jun Feng	2.14	2.06	2.18	2.126667	2.3	2.4	2.2	2.3
XueErQuan	3.07	3.04	3.54	3.216667	2.15	2.52	2.51	2.393333
Yan Bi Rong	2.39	2.42	2.11	2.306667	2.79	2.75	2.3	2.613333
Zhu Jin Hua	2.07	2.07	1.98	2.04	2.56	2.17	2.15	2.293333
Chen Shao Xian	2.85	2.95	2.3	2.7	2	2	1.93	1.976667
Li Chun You	2	1.89	2.22	2.036667	2.31	2.22	2.19	2.24
Yang Kun	2.26	2.36	2.47	2.363333	2.13	2.33	2.4	2.286667
Zhou Shu Lan	2.69	2.79	3	2.826667	3.02	2.94	2.86	2.94
Jing Yu	2.52	2.39	2.48	2.463333	2.44	2.2	2.2	2.28
Zhou Fu Ming	2.36	2.45	2.13	2.313333	2.45	2.36	2.27	2.36
Dong Peng Nian	2.64	3.02	2.75	2.803333	2.45	2.11	2.09	2.216667
Zhang Wen Xiu	2.37	2.02	2.3	2.23	2.48	2.29	2.36	2.376667
Dong Shun Ying	2.46	2.56	2.19	2.403333	2.36	2.13	2.11	2.2
Li Yong Qing	2.4	2.8	2.14	2.446667	2.27	2.27	2.27	2.27
			Mean	STDEV			Mean	STDEV
			2.42899	0.306278			2.367101	0.204693
	ACA							
	Mean			STDEV				
	2.398043478			0.259468189				

Name	MCA							
	L			Mean	R			Mean
bai-YS	3.13	3.33	3.16	3.206667	2.83	3.26	3.06	3.05
Huang De Cheng	3.29	3.1	3.11	3.166667	3	3.12	3.15	3.09
Liu Yun Cong	3.33	3.48	3.47	3.426667	3.21	3.2	3.47	3.293333
Ma Gui Ling	3.33	3.28	3.22	3.276667	3.49	3.21	3.49	3.396667
Peng Gong Bing	3.33	3.21	3.3	3.28	3.64	3.82	4.1	3.853333
Qi Xia Wa	3.2	3.33	3.47	3.333333	3.64	3.1	3.17	3.303333
Ren Shu Ying	3.36	3.36	3.07	3.263333	2.83	3.26	3.06	3.05
Sun Shu Zheng	3.04	2.92	3.06	3.006667	2.8	2.81	2.86	2.823333
Tong Tui Yuan	2.97	2.69	3.02	2.893333	2.97	3.32	3.2	3.163333
Wang Jun Feng	2.58	2.48	2.5	2.52	2.56	2.66	2.4	2.54
XueErQuan	3.49	3.67	3.02	3.393333	3.04	3.05	3.58	3.223333
Yan Bi Rong	3.46	3.14	3.5	3.366667	3.43	3.6	3.2	3.41
Zhu Jin Hua	2.64	2.97	3.1	2.903333	3.2	3.37	3.4	3.323333
Chen Shao Xian	3.37	3.31	3.38	3.353333	3.52	3.34	3.02	3.293333
Li Chun You	2.55	2.36	2.46	2.456667	2.5	2.36	2.36	2.406667
Yang Kun	2.96	2.47	2.54	2.656667	2.5	2.54	2.33	2.456667
Zhou Shu Lan	3.67	3.5	3.6	3.59	3.14	3.19	2.87	3.066667
Jing Yu	3.14	3.11	3.14	3.13	3.28	3.22	3.48	3.326667
Zhou Fu Ming	3.79	3.31	3.4	3.5	3.16	3.18	3.7	3.346667
Dong Peng Nian	2.65	2.92	3.02	2.863333	2.74	2.83	2.56	2.71
Zhang Wen Xiu	2.94	2.88	2.98	2.933333	2.48	2.27	2.36	2.37
Dong Shun Ying	2.53	2.56	2.81	2.633333	3.07	3	2.74	2.936667
Li Yong Qing	2.53	2.85	2.44	2.606667	2.4	2.4	2.54	2.446667
			Mean	STDEV			Mean	STDEV
			3.076522	0.33431			3.038261	0.392593
	MCA							
	Mean			STDEV				
	3.057391304			0.361062159				

Name	ICA							
	L		Mean		R			Mean
bai-YS	4.49	4.95	4.32	4.586667	4.33	4.53	4.67	4.51
Huang De Cheng	4.03	4.44	4.53	4.333333	4.3	4.37	4.5	4.39
Liu Yun Cong	4.29	4.42	4.28	4.33	4.47	4.26	4.39	4.373333
Ma Gui Ling	5.57	5.7	5.02	5.43	4.54	4.84	4.78	4.72
Peng Gong Bing	4.89	5.15	5.07	5.036667	5.62	5.57	5.73	5.64
Qi Xia Wa	4.73	4.61	4.7	4.68	5.13	4.95	4.66	4.913333
Ren Shu Ying	4.99	4.96	5.15	5.033333	5.04	5.12	5.02	5.06
Sun Shu Zheng	5.57	5.33	5.67	5.523333	5.9	5.73	5.55	5.726667
Tong Tui Yuan	4.96	4.99	5.12	5.023333	4.33	4.12	4.11	4.186667
Wang Jun Feng	4.96	5.12	4.97	5.016667	5.15	4.85	5.02	5.006667
XueErQuan	4.85	4.88	4.97	4.9	4.52	4.56	4.56	4.546667
Yan Bi Rong	5.71	5.94	5.62	5.756667	4.85	4.77	4.95	4.856667
Zhu Jin Hua	4.88	4.83	4.98	4.896667	5.12	5.16	5.04	5.106667
Chen Shao Xian	5.31	5.02	5.07	5.133333	4.83	5.1	4.7	4.876667
Li Chun You	5.49	5.62	5.48	5.53	5.11	5.1	5.2	5.136667
Yang Kun	5.03	5.49	5.63	5.383333	5.01	5.19	5.08	5.093333
Zhou Shu Lan	5	4.85	4.91	4.92	5	4.96	4.99	4.983333
Jing Yu	5.92	5.47	5.34	5.576667	5.71	5.12	5.14	5.323333
Zhou Fu Ming	4.7	4.72	4.62	4.68	4.3	4.26	3.65	4.07
Dong Peng Nian	4.67	4.75	4.46	4.626667	5.19	5	5	5.063333
Zhang Wen Xiu	3.84	4.18	3.98	4	4.64	4.56	4.09	4.43
Dong Shun Ying	5.54	5.66	5.77	5.656667	4.66	4.96	4.85	4.823333
Li Yong Qing	6.15	6.22	6.56	6.31	5.74	5.25	5.73	5.573333
			Mean	STDEV			Mean	STDEV
			5.05928	0.535754			4.88739	0.444182
	ICA							
	Mean				STDEV			
	4.973333333				0.494301353			

Name	BA			
				Mean
bai-YS	3.83	4.1	3.69	3.873333
Huang De Cheng	4.15	3.21	3.6	3.653333
Liu Yun Cong	3.07	3.4	3.02	3.163333
Ma Gui Ling	3.6	4.5	3.87	3.99
Peng Gong Bing	4.34	3.69	3.78	3.936667
Qi Xia Wa	4.33	4.15	4.42	4.3
Ren Shu Ying	4.7	4.73	4.8	4.743333
Sun Shu Zheng	4.24	3.98	4.01	4.076667
Tong Tui Yuan	3.4	3.34	3.2	3.313333
Wang Jun Feng	4.42	4.46	4.2	4.36
XueErQuan	3.58	4.1	3.4	3.693333
Yan Bi Rong	3.78	3.75	3.65	3.726667
Zhu Jin Hua	2.97	3.26	3.1	3.11
Chen Shao Xian	3.87	3.83	4.2	3.966667
Li Chun You	3.77	3.88	3.73	3.793333
Yang Kun	3.31	3.48	3.2	3.33
Zhou Shu Lan	3.75	3.71	3.97	3.81
Jing Yu	4.22	4.39	4.1	4.236667
Zhou Fu Ming	3.34	3.36	3.94	3.546667
Dong Peng Nian	3.49	3.07	3.96	3.506667
Zhang Wen Xiu	3.31	3.59	3.01	3.303333
Dong Shun Ying	3.6	3.07	3.8	3.49
Li Yong Qing	3.5	3.21	3.33	3.346667
			Mean	STDEV
			3.75087	0.4172
	BA			
	Mean		STDEV	
	3.339333333		0.539671332	

Appendix 3: My related publications

Gao, X.W., Hui R.,Tian Z.M. White A. 2009A new approach to estimation of non-isotropic scale factors for correction of MR distortions,*International Journal of Computer Assisted Radiology and Surgery,* 4 (s1): s349-350.

Gao, X.W., Hui R. Building a template of cerebrovascular architecture to assist path planning for image-guided neurosurgery. (In submitting)

Qian Y, Hui R., Gao X. W., 2013 3D CBIR with sparse coding for image-guided neurosurgery *Signal Processing,* 93:1673–1683.

Gao X. W., Qian Y., Hui R. 2011 The state of the art of medical imaging technology: from creation to archive and back,*The Open Medical Informatics Journal*, 5 (Suppl 1) 73-85.

Gao X. W., Qian Y., Hui R.,Loomes M., Comley R., Barn B., Chapman A., and Rix J., 2010 Texture-based 3D Image Retrieval for Medical Applications, *IADIS Multi Conference on Computer Science and Information System(MCCSIS)*, July, 2010.

Qian Y., Gao X. W., Loomes M., Comley R., Barn B., Hui R., Tian Z.M. 2011 Content based image retrieval of 3D images, *The Third International Conference on eHealth, Telemedicine, and Social Medicine, eTELEMED 2011*, Guadeloupe, France.

Gao X., Qian Y., Loomes M., Comley R., Barn B., Chapman A., Rix J., Hui R., Tian Z.M. 2012 Retrieval of 3D Medical Images via Their Texture Features, International , *International Journal On Advances in Software*, 2011 no 3&4, 2012.